

STRUCTURE AND DEFORMATION IN A PROPAGATING SURGE FRONT

by

Willam Tad Pfeffer

A dissertation submitted in partial fulfillment
of the requirements for the degree of

Doctor of Philosophy

University of Washington

1988

Approved by _____
(signature of chairperson of committee)

Program Authorized
to Offer Degree _____

Date _____

Doctoral Dissertation

In presenting this dissertation in partial fulfillment of the requirements for the Doctoral degree at the University of Washington, I agree that the Library shall make its copies freely available for inspection. I further agree that extensive copying of this dissertation is allowable only for scholarly purposes, consistent with "fair use" as prescribed in the U.S. Copyright Law. Requests for copying or reproduction of this dissertation may be referred to University Microfilms, 300 North Zeeb Road, Ann Arbor, Michigan 48106, to whom the author has granted "the right to reproduce and sell (a) copies of the manuscript in microform and/or (b) printed copies of the manuscript made from microform."

Signature _____

Date _____

University of Washington

Abstract

STRUCTURE AND DEFORMATION IN A PROPAGATING SURGE FRONT

by William Tad Pfeffer

Chairperson of the Supervisory Committee: Prof. C. F. Raymond

Geophysics Program

Detailed daily measurements of geometry and velocity made at the terminus of Variegated Glacier, Alaska, during the latter part of the 1982/83 surge showed that thick (≈ 100 m), rapidly sliding (≈ 30 m d^{-1}) ice entered thin (≈ 50 m) stationary ice, producing high longitudinal compressive strain rates (≈ -0.1 d^{-1}). The associated total strain reached a maximum of -0.75 (logarithmic). Finite element calculations showed that horizontal velocities were essentially constant with depth. Discrepancies between measured and calculated vertical velocities indicate that volume was not conserved in the surge front, and that void formation caused an increase in glacier volume of about 12%. Calculated basal stresses show anomalously high basal shear at the leading edge of the front, and anomalously low basal shear in the central part of the front. Basal normal stresses are essentially overburden. Simplified analytical modelling based on depth independent velocity and continuity provides simple estimates of finite strain versus depth and indicates that a front may propagate through ice at a steady speed and with unchanged shape, provided variables such as initial thickness and upstream velocity do not vary. The observed variations in shape and speed of the front are consistent with changes in these variables.

A structural study made after the surge showed that macroscopic structures in the terminus include recognizable primary layering, and two sets of foliation developed during

the surge: a transverse bubble foliation, which was well developed in all ice experiencing compressive strains of more than about -0.1, and a pervasive set of longitudinal cracks and associated bubble traces caused by transverse extension. C-axis fabrics in the ice affected by the surge and containing the transverse foliation resemble fabrics seen in ice subjected to plane strain compression near 0°C in other glaciers and experiments, and have symmetry consistent with the transverse bubble foliation. Neither foliation is explained by passive reorientation of preexisting inhomogeneities by large compressive strains, which is commonly supposed to be the cause of foliation in glacier ice. These foliations were developed rapidly by high strain rate.

TABLE OF CONTENTS

	Page
LIST OF TABLES	v
LIST OF FIGURES	vi
1. Introduction	1
1.1 Glacier Surges and Interesting Questions	1
1.2 Variegated Glacier, Alaska	2
1.3 Plan of the Dissertation	5
2. Passage of the Surge Front Through Variegated Glacier, Alaska	7
2.1 Introduction	7
2.2 Setting and Measurements	7
2.3 Evolution of Topography and Motion	8
2.3.1 Spatial pattern	8
2.3.2 Temporal Variation	10
2.4 Evolution of Surface Morphology	11
2.4.1 Tectonic Zones	11
2.4.2 Structural Pattern at the Termination of the Surge	13
2.5 Finite Strain in the Terminus Region	14
2.5.1 Strain Rate Based on Interpolated Survey Data	14
2.5.2 Strain Rate Based on Automatic Short Baseline Measurements	18
2.5.3 Estimate of Finite Strain in the Terminus Region	21
3. Englacial Structures Following the Surge	37
3.1 Introduction	37
3.2 Presurge Conditions	38

3.3 General Postsurge Conditions	39
3.4 Planar Structures in the Terminus Region	41
3.4.1 Classification of Structural Types	42
3.4.2 Interpretation	44
3.5 Crystallographic Fabrics in the Terminus Region	56
3.5.1 Method	56
3.5.2 Crystallographic Fabrics	57
4. Modelling of Flow In the Propagating Surge Front	77
4.1 Introduction	77
4.2 Model Design	77
4.2.1 Modelling Strategy	77
4.2.2 Finite Element Program	78
4.2.3 Rheology	78
4.2.4 Grid Geometry	79
4.2.5 Boundary Conditions	79
4.2.6 Scheme For Matching Boundary Conditions	80
4.2.7 Sensitivity Tests	81
4.3 Calculations Based on Front Data	84
4.3.1 Representative Days	84
4.3.2 Pattern of Velocity	84
4.3.3 Pattern of Stress	86
4.4 Fractures	88
5. A Simplified Surge Front Model	107
5.1 Introduction	107
5.2 An Analytic Model of the Front	107
5.3 A Finite Element Model of the Steady State Front	114
5.4 Summary	116
6. Synthesis	127
6.1 Introduction	127
6.2 Descriptive summary	127

6.3 New Developments	129
----------------------------	-----

REFERENCES	133
------------------	-----

Pocket material: Figure 3.9

LIST OF TABLES

Number	Page
3.1 Coordinates of reference markers in terminus region	44

LIST OF FIGURES

Number	Page
2.1 Terminus region of Variegated Glacier, showing reference markers	24
2.1 (continued) Terminus region, 18 June and 28 August, 1983	25
2.2 Longitudinal elevation profiles	26
2.3 Longitudinal elevation profiles and velocities	27
2.4 Emergence angles, strain rate, and thickness times strain rate	28
2.5 Propagation of various indicators of front passage	29
2.6 Velocity versus time at fixed locations	30
2.7 Finite strain at fixed locations	31
2.8 Large baseline strain rate above BX	32
2.8 (continued) Large baseline strain rate below BX	33
2.9 Automatic short baseline strain rate at BX	34
2.9 (continued) Automatic short baseline strain rate at DX	35
2.10 Profile of finite strain from various sources	36
3.1 Terminus region on 1 September 1974	61
3.2 Elevation profiles before and after surge	62
3.3 Schematic of structural types	63
3.4 Primary layering (S_0)	64
3.5 Transverse foliation (S_1) and longitudinal foliation (S_2)	65
3.6 Crevasses in S_2 orientation	66
3.7 Subhorizontal foliation (S_b)	67
3.8 Transverse P_1 structures	68
3.10 Relation of P_1 , P_2 , and S_2	69
3.11 Displacement of fold in P_1	70

3.12 Thick section of coarse bubbly ice	71
3.13 Sketch of thin section at site C	72
3.14 C-axis orientations at sites in terminus region	73
3.14 (continued)	74
3.14 (continued)	75
3.15 Schematic of fabrics and structures in terminus region	76
4.1 Finite element velocity and stress solution for 21 June, 1983	91
4.1 (continued)	92
4.2 Finite element velocity and stress solution for 25 June, 1983	93
4.2 (continued)	94
4.3 Finite element velocity and stress solution for 29 June, 1983	95
4.3 (continued)	96
4.4 Finite element velocity and stress solution for 4 July, 1983	97
4.4 (continued)	98
4.5 Finite element velocity and stress solution for 6 July, 1983	99
4.5 (continued)	100
4.6 Deformation of grid on 25 June	101
4.7 Calculated velocity, strain rate, and basal stress for 22 June, 1983	102
4.8 Tensile stresses on 21 June, 1983	103
4.9 Tensile stresses on 25 June, 1983	104
4.10 Tensile stresses on 29 June, 1983	105
4.11 Hydrofractures an 21 June, 1983	106
5.1 Schematic of idealized surge front	118
5.2 Particle path and horizontal velocity in sinusoidal front	119
5.2 (continued) vertical velocity and strain rate	120
5.3 Construction of composite front	121
5.4 Particle path and horizontal velocity in composite front	122
5.4 (continued) vertical velocity and strain rate	123
5.5 Finite element grid for composite front	124
5.5 (continued) Velocity and stress solution	125
5.6 Calculated and steady state velocities in composite front	126

ACKNOWLEDGMENTS

Several universities and many people have participated in the Variegated Glacier project. My own involvement goes back to 1980, and in the seven years and twelve trips to the glacier since that time I have been associated with and received assistance from most of the parties involved. In this sense, the first person plural used in this dissertation is truly collective, and not simply an editorial convention.

I am indebted first to Charlie Raymond, for including me in the Variegated Glacier project, and for his support and expert guidance while I have been a student at the University of Washington. He has provided vital ideas and has served as the primary critic and judge of this work. The other members of my supervisory committee have each added their own expertise during the preparation of this dissertation: Ed Waddington advised in particular on matters of stress and strain, and provided editorial discipline. Bill Bruner also gave expert advice on stress and strain, as well as on matters concerning fracture, and acted as the consulting geologist to the committee. Mike Brown gave needed advice on parts of the finite element modelling. Chris Bretherton helped to sort out some preliminary confusion regarding the material of Chapter 5, and gave an opinion on the feasibility of certain other related objectives which resulted in the saving of some some valuable time.

The field work done at Variegated Glacier has been very dependent on the assistance of others; in particular, I would like to thank Neil Humphrey for his help, especially during the exhausting months of May and June, 1983, and for his electronic expertise, to which I owe the existence of the automatic strain rate records. Jon Harbor joined me in 1985 for a very frugal but productive summer, in which we worked out the problem of how to approach the structure in the terminus region. Bill Bruner joined us at the end of this trip, and supplied the first expert guidance. Mark Lockwood worked with me in 1986, when, with a push in the right direction from Charlie Raymond, we saw the light and finished the job.

Several other people have contributed specific indispensable items for which I am grateful. Charlie Raymond, Tomas Johannesson, Magnus Magnusson, and Martin Sharp did the surveying in the terminus region between 21 June and 18 July 1983, from which the

kinematic information was obtained; Tomas Johannesson did the extensive analysis of the survey data to produce the position, velocity, and strain rate data which appears in Chapter 2; Roy Walters (U.S.G.S) pointed me to the proper sources to resolve the pressure instability problems described in Chapter 4; Mark Brandon (Yale University) provided the computer program which was used to calculate the statistics of the c-axis distributions in Chapter 3; Tom Grenfell supplied the computer on which the c-axis analyses were done, as well as his own time in getting things running.

Finally, I want to thank my wife Anne, who has taken all this in stride, despite having her own academic fish to fry, even as I fry mine.

CHAPTER 1

INTRODUCTION

1.1 Glacier Surges and Interesting Questions

What question does one first think to ask about surges? Probably the question is "why?". Why does one region of the world contain surging glaciers and not another? Why, within a region of surging glaciers, do some glaciers not surge? Why does a surge, once started, not stop until it has so completely transformed the geometry of the glacier? Another likely question is "how?". How is the rapid motion accomplished? How is the surge initiated - in parts, or does the entire length of the glacier start surging at once? How does it terminate?

Other questions come to mind. In an unknown territory such as glacier surging, the questions of "why" and "how" are quickly displaced by the more fundamental question "what?". What happened? Interpretation and explanation follow the establishment of a foundation of facts: exploration and observation.

This dissertation is to a large degree concerned with "what". In particular, it addresses the questions of what happened, kinematically, at the terminus of a glacier as the ice there was activated by a surge, and what structures developed in the ice as a consequence of the deformation. Some answers to the question "how" are provided as well, since knowing what happened kinematically immediately gives some insight as to how some structures developed.

These questions and answers will find some application outside of the immediate topic of glacier surges. Deformation occurs and structure develops in all glaciers, and on a larger spatial and longer time scale in geologic settings as well. The observations here have relevance in a general sense, and in fact add information not readily obtainable on other glaciers, for what must be inferred to have occurred over many years on a non-surging glacier was observed here in the space of two weeks. The same consideration applies to geologic problems as well, and the advantage presented by the short time scale of the surge is even greater. Quite apart from any questions relating to surges, the events we describe here serve as a comparatively accessible experiment in plane-strain deformation at high stress, in which anyone with an interest in such things will probably discover something interesting.

1.2 Variegated Glacier, Alaska

Variegated Glacier is a small temperate glacier on the west slope of the St. Elias Mountains of south east Alaska. It is approximately 20 km long, and descends from 1950 m to near sea level at Russell Fjord. The main channel of the glacier is about 1 km wide and has a fairly uniform slope of about 5°. Two wider accumulation basins lie at its head, and a wider lobe of ice forms its terminus. This wide lobe, referred to as the "terminus region" throughout this dissertation, is about 3 km long and 2 km wide, and is for the most part covered with a thick mantle of debris.

The glacier has a documented history of surge behavior which indicates that surges occur in roughly 20 year intervals. Surges were observed or inferred during the periods 1905-1906, sometime between 1911 and 1933, sometime between 1942 and 1948, 1964-65, and most recently January 1982 - July 1983.

Based on the periodicity of surges up to 1965, a surge sometime in the early 1980's was anticipated. A long-term project was started in 1973 to study Variegated Glacier in its quiescent phase and gain an understanding of its behavior between surges, and to prepare the necessary foundation of information for a thorough observation of the coming surge. Participating in this project were personnel from the Universities of Washington and Alaska and the California Institute of Technology. Bindschadler et al (1977) provide a detailed picture of the geometry and motion of Variegated Glacier in its quiescent phase. The changes which occurred in the glacier as it built up to its surge are described in a pending paper (Evolution of Variegated Glacier Alaska, U.S.A., Prior to its Surge, Raymond, C. F., and Harrison, W.D., manuscript submitted).

The surge of Variegated Glacier in 1982 and 1983 occurred in two phases, occupying the winter and first part of the summer of each year. (Previous surges may well have occurred in similar phases, but observations were too infrequent to tell this.) During the period January 1982 to 26 June 1982, surge motion developed on the upper half of the glacier, with velocities reaching 10 m d^{-1} , but the lower half remained unaffected. On 26 June 1982, the velocities dropped dramatically, and by late July had returned to pre-surge levels ($\approx 1\text{-}2 \text{ m d}^{-1}$). Velocities rose again in October 1982 and continued rising until maximum rates of over 60 m d^{-1} were reached in June 1983. The surge ended with a second abrupt drop in velocities to non-surgeing rates on 5 July 1983. A general description of the

1982/83 surge is given in Kamb et al (1985).

During the second phase, following October 1982, the surge entered the lower half of the glacier, propagating downglacier as a kinematic wave at an average speed of about 20 m d⁻¹. As the wave, or "surge front", entered thinner ice, it created a dramatic topographic step which, by the time it entered the terminus region, moved at about 40 m d⁻¹ and stood above the old ice surface by a height nearly equal to the initial depth. A detailed description of the surge front is given by Raymond et al, (1987). Parts 2.1-2.4 of Chapter 2 are excerpted from that paper.

The propagation of the surge front into the terminus region and the tectonic developments which accompanied it were among the more dramatic and unexpected aspects of the surge. These developments are described in Chapter 2. It was realized that the substantial, well-documented deformation in the terminus region provided a rare opportunity to relate englacial structures developed during the surge to stress and strain histories which are much better known than is typically the case. Under ordinary circumstances, the strain associated with structures in glacier termini has accumulated over very long periods of time and direct observation of the deformation has not been possible. Strain histories have been inferred in these cases by various methods. Hudleston (1977) estimated strains on the basis of deformation of natural strain markers; Hooke and Hudleston (1980) and Hudleston and Hooke (1980) calculated strains from finite element modelling of flow in which they assumed a steady state flow and constant surface configuration; Hambrey et al (1980) assumed steady state flow and calculated strains along paths which lay on the surface over the length of a glacier.

These analyses of strain history have been made in efforts to discover, among other things, how foliation originates in glaciers. The origin of foliation is a central topic in structural glaciology; in recent years it has been shown (mostly by the above authors) that in many cases foliation develops through accumulation of shear strains which rotate pre-existing inhomogeneities of almost any initial orientation into the final foliation direction. We show here, however, two categories of foliation which were developed in the absence of shear strains. The foliations are, in fact, unrelated to finite strain altogether, being apparently developed very rapidly in an orientation related to the state of stress at that time.

As well as occurring in a period of time short enough to be conveniently measured, the deformation in the surge front developed at rates which may be more conveniently simulated experimentally than ordinary glacier flow. Typical glacier strain rates are $\leq 0.1 \text{ yr}^{-1}$, while strain rates in the surge front were on the order of 0.1 d^{-1} (in compression). The time involved in the passage of the surge front was also short, with most of the deformation in a given parcel occurring in 7-10 days. Experiments conducted at these strain rates and at such short time scales present problems peculiar to high stresses, but do not involve long periods of time waiting for significant strains to develop. Crystallographic fabrics were measured in ice from the terminus region with comparisons to future experimental work in mind, and for comparison with measured finite strains and the state of stress during the surge.

In no previous case has an episode of deformation such as the Variegated Glacier surge been observed in its entirety and the details of deformation and motion measured. Even in this case the relation between structures, fabrics, and strain is not entirely straightforward, owing principally to the lack of a structural and fabric survey before the surge, and to the fact that only a part of the terminus region was observed in fine detail starting at a time before the entry of the surge front (although ice unaffected by the 1982/83 surge was available in 1985 and 1986 for comparison). Nevertheless, finite strains have been calculated on a much firmer foundation of observation than has previously been the case, and structures developed during the surge have generally been clearly distinguished from those which existed before.

The progress of the surge on Variegated Glacier in 1982 and 1983 provided the first detailed picture of the propagation of surge motion. Surveyed changes in surface geometry showed the kinematic progress of the surge in the terminus region (Raymond et al, 1987), while borehole inclinometry confirmed that the rapid motion of the surge is accomplished almost entirely by basal sliding (Kamb et al, 1985). The distribution of interior and basal stress is unknown, however, as well as whether basal sliding dominates the motion in the surge front. Finite element modelling of the flow in the surge front has been done here to address these problems.

1.3 Plan of the Dissertation

Four distinct topics are addressed in this dissertation. These are:

- 1) Observations of geometry and motion made during the passage of the surge through the terminus region.
- 2) Englacial structures and crystallographic fabrics in the terminus region following the surge.
- 3) Finite element calculations of internal and basal velocity and stress along a longitudinal profile in the terminus region.
- 4) Simplified models of flow and surge front propagation.

The observations of geometry and motion at the surface, together with finite element calculations of velocity and stress within the ice and at the base, provide a detailed picture of the kinematic evolution of the front. The kinematics are of interest both as they relate to questions of surge propagation and as an agent in the development of structures in the ice during the surge. The englacial structures and crystallographic fabrics are examined with the objective of understanding their origin in terms of the observed and calculated kinematic history during the surge. The hypothetical models of flow in the surge front are developed to distinguish features of propagation which are essential on the basis of such simple rules as continuity, and which are compatible with the specific geometries at hand.

These four topics are presented in this sequence in Chapters 2 through 5. While each topic has its own terminology, methods, and data, there is an intimate relation between the four which is an essential part of their interpretation. This interconnection creates some difficulty when discussing the separate topics. There is clearly a need to introduce each topic one at a time, but pertinent facts frequently have to be brought in, often from topics not yet presented. This results in a certain amount of cross-reference, and anticipation of information not yet presented. This has been kept to a minimum, and the references to as yet undefined information are made in a way which will hopefully leave to reader clear as to what has been introduced and what has not.

Chapters 2 through 5 are each presented in a more or less autonomous fashion, although the reader should have a pretty clear picture of their relationship by Chapter 5. In Chapter 6, once all terms have been defined and results presented, we give a summary of the pertinent events during the passage of the surge through the terminus region as

interpreted in the conclusions of the preceding chapters.

CHAPTER 2

PASSAGE OF THE SURGE FRONT THROUGH THE TERMINUS REGION OF VARIEGATED GLACIER, ALASKA

2.1 Introduction

Variegated Glacier, Alaska, surged between early January 1982 and 5 July 1983. A broad description of the surge is given by Kamb et al. (1985). The surge motion started in 1982 in the upper part of the glacier and the zone affected by the surge spread down glacier. By mid-1983 the surge speed reached its maximum of up to 65 m d^{-1} , and the lower edge of the surging zone entered the nearly stagnant terminal lobe. This propagating edge developed into a dramatic frontal zone expressed by a steep topographic ramp and a sharp horizontal velocity jump. Within the frontal zone, upward vertical velocity, longitudinal compressive strain rate, and stress were extremely high in comparison to normal glacier flow conditions. Compressional tectonic processes developed unusual ice surface structures including thrust faults, buckle folds, and longitudinally oriented cracks.

2.2 Setting and Measurements

Figure 2.1 shows the terminal lobe of Variegated Glacier, the positions of surface markers referenced in this paper, and the pre-surge and post-surge distribution of morainal surface debris. The downglacier propagating surge began to affect the upglacier edge of the photograph region in mid-May 1983 and propagated through it until 5 July, 1983, when surge motion abruptly terminated over the full length of the glacier.

Before 20 June, 1983, markers were spaced about every $1/4$ to $1/2$ km. In order to resolve more spatial detail in the propagating frontal zone, additional markers were placed on June 20 and surveyed daily thereafter until July 18. The vertical section in Figure 2.2 shows the marker positions at various times in relation to the approximate bed determined by seismic soundings (Bindshadler et al., 1977) and radio echo soundings (K.A. Echelmeyer and H.F. Engelhardt, personal communication, 1983).

Most of the markers added on June 20, 1983, were small marked stones. These were subject to displacement relative to ice particles from ablation, but the rates of several

centimeters per day were negligible in comparison to the surge-induced ice speeds. Coordinates of the markers were determined by conventional survey techniques using theodolite and electromagnetic distance ranging from the station GWM shown in Figure 2.1. This station was on an ice-cored moraine 42 m above the ice surface at its upglacier edge. Although this station was on the glacier, repeated surveying showed it to be essentially stationary and unaffected by the surging ice farther upglacier.

Because of the position of the survey station, the height of the topographic bulge, and the isolation of marker positions by crevassing, many of the highest markers could not be located as time progressed either because they were out of view or could not be reached with reflectors.

To describe and analyze the results, the following symbols will be used: x is the position on the westward running axis in the local Variegated Glacier Cartesian coordinate system (Bindshadler et al., 1977), XP is the curve distance along the centerline measured from the head, y is the elevation, u is the x component of velocity, v is the vertical component of velocity, and u_h is the horizontal component of velocity. On the terminal lobe the centerline and flow directions run essentially to the west so in practice x and XP differ by a near constant.

2.3 Evolution of Topography and Motion

2.3.1 Spatial Pattern

Figures 2.3a-2.3c show the detailed distributions of surface elevation and velocity. The distribution of horizontal velocity u_h (Figure 2.3b) defines three zones of dynamic activity: a stagnant zone in which u_h is relatively small (less than 0.1 m d^{-1}), a front zone in which u_h increases strongly with distance upglacier representing intense longitudinal compression, and a surging zone in which u_h is high (20 m d^{-1} or more) and increases gradually with distance upglacier. The same zones are apparent in the distributions of vertical velocity v (Figure 2.3c). In the stagnant zone, v is slightly negative from ablation. In the front zone, v is large (up to 7 m d^{-1}) and upwardly consistent with the large longitudinal compression. In the surge zone, v is downward, relatively space independent, and consistent with ice motion approximately parallel to the glacier surface. The front zone is displayed in the surface elevation profile as a steep topographic ramp (slope up to 15°

averaged over 100 m) with an elevation change of 50 m or more (Figure 2.3a). The width of the front zone is about 0.4 km or roughly 10 times the pre-surge depth.

The angle of upward motion γ (Figure 2.4a) shows a peaked pattern similar to that for the vertical velocity v (Figure 2.3c). Comparison of Figures 2.3c and 2.4a shows that the peak in γ occurs approximately 100 m downglacier from the peak in v . Since $\gamma = \tan^{-1}(v/u_h)$ and u_h decreases strongly downglacier, this shift of the peak in γ from the peak in v is expected. The maximum value of γ is in the range 30° - 40° .

Peaked patterns also appear in distributions of longitudinal compressional strain rate $-\partial u/\partial x$ (Figure 2.4b) and $-h\partial u/\partial x$ (Figure 2.4c). The distribution of $-\partial u/\partial x$ was calculated using optimal interpolation. Comparison of $-\partial u/\partial x$ (Figure 2.4b) and $-h\partial u/\partial x$ (Figure 2.4c) shows that within the spatial resolution of the measurements, the peaks in $-\partial u/\partial x$ and $-h\partial u/\partial x$ coincide. Apparently, $-\partial u/\partial x$ is so strongly peaked that the variation in h is too small to produce a noticeable shift of $-h\partial u/\partial x$. The peaks in $-\partial u/\partial x$ and $-h\partial u/\partial x$ are shifted downglacier from the peak in v , but not so far as the peak for γ . The spatial distributions of $-\partial u/\partial x$ and $-h\partial u/\partial x$ show secondary peaks upglacier from the principal peak; this substructure is not evident in the distributions for v . Maximum longitudinal compression rates averaged over a day are about 0.075 d^{-1} to 0.15 d^{-1} . Comparable compression rates were measured on a time scale shorter than a day using continuous recording strain meters, as discussed in section 2.5.2.

If the upward motion v were accomplished by a depth-independent longitudinal compression and corresponding vertical extension assuming incompressible, planar flow on a flat bed, then the patterns of thickness times strain rate $-(h\partial u/\partial x)$ (Figure 2.4c) and v (Figure 2.3c) should be the same. In fact, there is considerable similarity, but the peak in v is displaced noticeably upglacier from the peak in $-h\partial u/\partial x$. This is an interesting anomaly which also appears in finite element calculations, and is discussed in Chapter 4.

The migration of the features of these various spatial patterns down the glacier defines the propagation of the front zone. Figure 2.5 shows the position versus time of the rise points in u (defined as that location where u rises above 0.5 m d^{-1}), v , and the lower edge of the topographic front, which all closely coincide and define a sharp lower edge of the front zone. Peaks in the patterns of γ , $-\partial u/\partial x$, and v within the front zone are also shown. These all propagate roughly in parallel with a speed of $40 \pm 3 \text{ m d}^{-1}$ averaged over

the interval June 20 to July 5, 1983. The upper edge of the front zone is transitional and is less precisely defined but can be represented as the location where v and γ first reach 0. The secondary peaks in $-\partial u/\partial x$ (Figure 2.4b) and $-h\partial u/\partial x$ (Figure 2.4c) migrate more slowly and are confined between XP 17.6 and 18.0 km. These features could possibly be tied partly to irregularities in the bed topography not detected by the depth soundings.

2.3.2 Temporal Variation

Although the downglacier propagation of the surge front may be roughly described as the migration of a fixed spatial pattern, this is not precise. Examination of Figures 2.3b, 2.3c and 2.4b show the curves for u , v , and $-\partial u/\partial x$ tend to break up into four phases defined by the time intervals 22-27 June, 28-30 June, 1-5 July, and after 6 July. From Figure 2.3b it is evident that this represents a time variation of velocity within the surging zone, which affects the velocity pattern within the front zone (Figures 2.3 and 2.4) and its rate of advance (Figure 2.5). This is also seen in Figure 2.6, which shows the variation of velocity with time at fixed locations.

Possible explanations of the four phases are best described with reference to Figure 2.3b. The initial phase (22-27 June) is characterized by moderately high upstream velocities ($\approx 30 \text{ m d}^{-1}$). At the transition from the initial phase to the second phase (27-28 June), there is a large downglacier displacement of the profile. A possible explanation lies in the presence of a locally steep step in the original surface topography at the leading edge of the surge at this time, but more probably the cause is related to a speed-up experienced at other parts of the glacier at the same time. Figure 2.6 shows a sustained interval of high velocity at several sites on 27/28 June. Figure 9 of Kamb et al, 1985 shows a well-defined water pressure maximum at the same time at XP = 9.5. The increased water pressure may be expressed at the front not only by elevated velocities, but also by a more rapid advance of the zone of sliding.

The second phase (28-30 June) persists through 30 June, with the velocity at the upglacier end of the region diminishing slightly over the period. The transition from the second to third phase involves a distinct drop in velocity levels without a significant change in the shape of the velocity profile. This is associated with a glacier-wide slow-down and a discharge maximum at the outlet stream (Kamb, *et al* (1985)). Finally, the termination of the surge marks the transition to the fourth, post-surge velocity phase.

Velocities in the fourth phases drop dramatically on 5/6 July at the termination of the surge, and continue to fall throughout the remainder of the survey period, approaching stagnation by 9 July.

The same pattern is visible at a fixed point. For example, at XP 18.1 km (Figure 2.6), u rapidly rose from an initial value close to zero to a surge value of about 20 m d^{-1} as the surge front reached and passed by this location. If the surge velocity had remained constant, u would then have gradually increased with time as this location occupied places farther into the surge zone. Instead, this idealized pattern is masked by the period of relatively high surge velocity from June 28 to 30 and relatively low surge velocity from July 1 to 5. At all positions the time variation of velocity represents a combination of activation of the stagnant ice by the migration of the front zone and time variations in the surge speed farther upglacier.

2.4 Evolution of Surface Morphology

2.4.1 Tectonic Zones

Distinct zones of tectonic activity on the ice surface are associated with the front zone, and these migrate with the advancing front (Figure 2.5). These zones are relevant to the production of structures in the ice as discussed in Chapter 3.

At the lower edge of the front and extending approximately 100 m below the boundary of noticeable topographic or motion disturbance was a zone of distinctly audible microcracking. In this zone one could hear a pervasive and continuous emission of high-frequency noises similar to the noises when cellophane is crinkled. These noises were clearly distinct from the hissing and popping of out-gassing pressurized air bubbles frequently audible in ablation areas of glaciers and also distinct from the characteristic "ping" sound of an opening crevasse. No obvious surface features such as extended cracks were evident in this zone. However, finite element calculations presented in Chapter 4 suggest that the development of surface-parallel tensile fractures were responsible for these sounds.

Above the microcracking zone was a zone of prominent surface buckling features. These were formed by exfoliation of ice slabs on surface-parallel fractures (possibly produced during the microcracking events) and upward buckling of the slab. Surface-parallel

widths ranged from $\sim 10^{-1}$ m to ~ 10 m. Thicknesses ranged from $\sim 10^{-2}$ m to ~ 3 m. There was a consistent relationship between the surface width and thickness. The buckling would first develop as a gentle arch. In many cases this would progress with continued compression to a vertical standing isoclinal fold with parallel limbs and fractured hinge forming a vertical fence sometimes more than 4 m high running transverse to the flow direction. Also evident in this zone of buckling was the opening of longitudinal cracks perpendicular to the transverse running fold axes of the buckles. In this zone one heard occasional fracture events lasting up to a minute during which a sequence of "tearing sounds" appeared to propagate in various directions under areas more than 100 m in dimension and "ice quaking" could be sensed.

Above the front zone, active surface buckling was absent. Longitudinal cracks continued to widen into crevasses, and differential horizontal and vertical motions occurred across many of these crevasses. Such motions were indicated by vertical offsets of the former ice surface, relative displacement of ice structures, or development of scroll-like rolls of snow or ice by shearing of bridges. The longitudinally oriented plates of ice between the crevasses experienced differential tilting, buckling about vertical fold axes and disruption by secondary crevasses running oblique to the first longitudinal crevasses. Selected crevasses broadened into longitudinal chasms sometimes exceeding 30 m in width. In this zone, various cracking, creaking, and impact noises were common. Occasional episodes of rumbling seemed to come from deep within the glacier with no visible surface effects to account for them. At least some of these noises came from massive collapses into the chasms described above. Such collapses contributed to the broadening of the chasms and the development of irregular floors by partial filling with ice blocks.

This description of tectonic activity applies to the front at the centerline as it propagated from about $XP = 17$ km to $XP = 18.5$ km. The front was not nearly as dramatic when it was upglacier from $XP = 17$ km: the slope of the topographic ramp was less, microcracking was not noticeable at its toe, and surface buckling features did not form. The differences may be related to the small pre-surge ice depth below $XP = 17$ km (Figure 2.2), as discussed in a later section. This is also indicated by the occurrence of microcracking and buckling in the thin ice along the south margin of the terminal lobe (Figure 2.1) as the surging ice spread sideways. Active thrusting also occurred along this margin where the pre-surge ice was apparently very thin (W.B. Kamb and M. Sharp, personal

communication, 1983). A possible mechanism for the thrusting and reasons why it did not develop in the surveyed region are discussed in Chapter 4.

2.4.2 Structural Pattern at Termination of the Surge

At the termination of the surge the ice surface at any location had been modified by the processes described above to an extent dependent on how far the surge front had progressed past it. Ablation also modified the surface morphology. Starting from the stagnant zone and proceeding upglacier, one would come to a sharp break in slope. Proceeding up the slope, one would find surface buckles of increasing sharpness and amplitude. Approximately half way up the slope ($XP \approx 18.1$ km) these buckles had thicknesses of several meters and were of sufficient amplitude that their steeply sloping, downglacier limbs impeded upglacier progress on foot. At about this location, longitudinal crevasses were also sufficiently wide and closely spaced to make sideways progress difficult. Near the top of the slope ($XP \approx 18.0$ km) and about 0.4 km above, the principal surface features were rubble fields of slab like pieces of ice from collapsed surface buckle folds formed earlier as the surge front passed. Through this zone, longitudinal crevasses widened upglacier. Above about 1.5 km from the surge edge ($XP \approx 17$ km), buckle folds never formed, and the surface was free of rubble. Longitudinal crevasses were more numerous and wider, and the longitudinal ice plates between them were often buckled. Above this location, longitudinal chasms and obliquely running crevasses made upward progress on foot impractical.

The distribution of the above described features was nonuniform. The surface profile of the surge front was not smooth but showed a "wrinkling" and "dimpling" correlated with preexisting surface irregularities usually associated with differing moraine cover thickness and composition. These irregularities presumably arose by differential ablation prior to the surge and were amplified by deformation during the surge. The apparent wave in the surface profile at $XP \approx 18.0$ km (Figures 2.2 and 2.3a) is an example. Other smaller-scale topography was not resolved by the spatial sampling of the surveys but was apparent in sequential aerial photography from July 28, 1982, June 18, 1983, and August 28, 1983. Such wrinkles often ran southwest to northeast oblique to the flow direction and axis of compression aligned nearly east to west. The longitudinal crevasses and buckle folds tended to form preferentially on the downglacier side or on the topographic highs with consistent orientation parallel and perpendicular, respectively, to the flow direction independent of the trend of the topographic ridge.

2.5 Finite Strain in the Terminus Region

Calculations of longitudinal strain have been made by two independent methods in the terminus region during the passage of the surge front. One method uses strain rates derived from the surveyed velocities presented in section 2.3, while the other method is based on direct measurements of tilt and strain by automatic recording tiltmeters and short (1 m) baseline strain meters. These latter data are part of a set of measurements which produced strain and tilt rate data for the entire lower glacier between February and June 1983. The results of this larger project will be presented elsewhere.

The strain rates presented here are regarded as principle compressional strain rates. In both methods the strain rates were calculated along baselines oriented very nearly in the direction of flow, but a small cross-component of flow was found to exist at all sites once the site had entered the fast-moving surge zone (where strain rates were comparatively low). At the time of maximum compressive strain rate, however, the cross-component of velocity was negligible, and the effect on finite strain is therefore not considered.

2.5.1 Strain Rate Based on Interpolated Survey Data

Method of calculation

The longitudinal distributions of velocity presented in section 2.3 (Figure 2.3b) were smoothed by interpolation of data measured at points separated by about 50 m on the glacier. Profiles of longitudinal strain rate were taken from the slope of the resulting curves to produce Figure 2.4b. The history of strain rate for a given point fixed in the ice can be calculated from Figures 2.3b and 2.4b by reading the strain rate from Figure 2.4b for a given day, and then moving to the next day's position by reading the appropriate velocity from Figure 2.3b. This can be done either forward or backward in time. In the strain histories presented here, the final position of the point is used to start, so that histories can be calculated for seven specific sites examined after the surge. These are labeled A through H and are located on Figure 2.1a. The relation between strain history and structures at these sites will be discussed in Chapter 3.

Finite strains can be calculated for each strain rate record simply by summing the daily strains, provided that the strain is always coaxial, i.e. that the direction of principle compressive strain does not change its orientation relative to the measurement baseline. The cross-components of velocity mentioned above would affect this assumption, but again

they are negligible during the arrival of the surge front when most of the straining occurs. The resulting finite strain is a logarithmic strain, being calculated on a baseline which changes with time according to the strain. This is an appropriate strain to use for large displacements. All of the strains calculated from the various sources presented here are logarithmic.

Data and discussion

The calculated strain rate and accumulating finite strain for the seven sites over the interval 21 June - 5 July is shown in Figure 2.7. Only two sites - F and G - near the final position of the front were surveyed during the entire interval between the arrival of the surge front and the termination of the surge on 5 July. The five sites above F and G were already involved in the surge on 21 June when surveying was started. No site on the profile was surveyed for long enough to capture both the characteristic arrival of the front, as seen in F and G, and the tail of lower but still significant strain rate as seen at the upper sites. A comparison of the sequence of sites gives a picture of the typical strain history at any one location, however.

Before the arrival of the front, a typical site shows no longitudinal straining, although some very low level strain rate may be present, as will be seen in the automatic strain recordings to be described later. The arrival of the front produces a dramatic rise in compressive strain rate to reach the maximum levels measured (typically -0.08 to -0.10 d^{-1}) within one day of the onset. This rise may involve an intermediate phase of compression at a lower level, as seen at G, but such a phase is not always present. A rapid onset of high compressive strain rate at a site corresponds in the profiles of velocity to a narrow concave-up leading zone. Similarly, an intermediate phase of compression corresponds to a slower rise in velocity resulting in a broader concave-up leading zone. The spacing of data points in the velocity profiles also influences the calculated shape, however. The onset of compression at F is shown as a smooth rise to high levels, but in the automatic records of strain we will see that the onset of compression can be very sudden indeed. When measured on a shorter baseline, compression may rise from near zero to high levels in the space of a few hours.

Compression at the highest level is maintained for about one day, and is terminated by a pronounced drop to levels about half of the maximum value. Thereafter, the

compressive strain rate drops in stages, with short episodes of higher compression, until, as seen at site A, the strain rate drops essentially to zero. The drop to zero strain rate occurs not because the ice is stagnant again, but because it is being carried in the central part of the surge zone. The velocity at site A at the time when strain rates dropped to zero was about 30 m d^{-1} .

The total strain accumulated at any site between the arrival of the front and the end of the surge is known from direct measurement only for sites F and G. These are -0.625 and -0.221, respectively. The sites further upglacier are missing the initial phase of maximum compression which occurred before surveying began. By assuming that the missing phases at the various sites are of approximately the same magnitude as those present at other sites, a rough composite estimate can be made using sites F, E, and B, which puts the total strain at -1.1 for this part of the glacier. The assumption that missing phases of the strain rate pattern may be combined is justifiable only over short distances, where the surge front passed without substantial changes in its geometry or velocity. The three sites used to make this estimate are within 600 meters of each other, in a region of uniform slope and thickness.

The magnitudes of strain rate and total strain at the surge front can be understood in a general way in terms of the thickness and velocity change across the front. A simple hypothetical model is developed along these lines in Chapter 5, but for the present purpose, we need only identify the velocity u_2 and the thickness h_2 below the surge front, the velocity u_1 , and thickness h_1 at the top of the surge front, and the longitudinal length L of the front. Assuming that the horizontal component of velocity is independent of depth (calculations in Chapter 4 show that this is justified), and that the glacier is a parallel-sided slab except in the front zone, the average strain rate across the front is

$$\bar{\epsilon} = \frac{u_2 - u_1}{L} \quad (2.1)$$

The total longitudinal strain across the front zone can be found through the vertical extension of a column of ice which starts at the base of the front at thickness h_2 and ends at thickness h_1 at the top. Continuity of the column requires that

$$h_2 \Delta x = h_1 \Delta x^*$$

where Δx and Δx^* are the longitudinal dimension of the column before and after its passage

through the front. From this one finds the ratio of the thicknesses, and the total strain E :

$$\frac{\Delta x^*}{\Delta x} = \frac{h_2}{h_1}$$

$$E = \frac{\Delta x - \Delta x^*}{\Delta x} = 1 - \frac{h_2}{h_1}$$

The logarithmic strain is more appropriate for the present purpose; it is

$$E_l = \ln \frac{h_2}{h_1} \quad (2.2)$$

The predictions of equations 2.1 and 2.2 can be tested against the measurements presented in Figure 2.7. At the time of passage of the front past F, $u_2 - u_1 \approx -22 \text{ md}^{-1}$, while $h_1 \approx 78 \text{ m}$, $h_2 \approx 40 \text{ m}$, and $L = 365 \text{ m}$. The measured average strain rate in the 9 day period (26 June to 5 June) recorded at F was -0.069 d^{-1} , while equation 2.1 predicts an average strain rate of -0.060 d^{-1} . The measured finite strain (logarithmic) in the same interval was -0.626 , while equation 2.2 predicts -0.668 . This agreement is moderately good, and shows that the observed strain rate and finite strain can be accounted for approximately in this region by a simple model of flow through the front.

Earlier, as the surge front propagated down from the higher reaches of the glacier, the surge front had a less distinct topographic character. The distance L between the upper and lower limits of the surge zone was greater (2 km above the terminus region, $L \approx 900 \text{ m}$), and the front height was smaller relative to the total ice thickness, making $\frac{h_2}{h_1}$ closer to 1.

Equations 2.1 and 2.2 show that, in the idealized geometry described above, this results in a reduction in the predicted strain rate and total strain across the front. This was observed, but it is difficult to apply the simple theory to long reaches on the upper glacier, where it is unrealistic to make the assumption that the glacier is a parallel-sided slab.

Figure 2.8 shows strain rates calculated from survey data at 3 widely spaced sites in the upglacier part of the terminus region. Figure 2.8a shows strain rate calculated on an (initially) 530 m baseline whose downglacier end lay at site BX (Figure 2.1a). Figure 2.8b shows strain rate calculated on an (initially) 500 m baseline whose upglacier end lay at site BX. Strain rates were calculated by dividing the current velocity difference by the current baseline, with velocities averaged over approximately 24 hours.

Once again, when calculated on 500 m baselines, strain rates show a slower onset of the initial compressive phase than the 50 m baseline data shown in Figure 2.7. The rise to maximum levels occurs over a period of 12 days on the baseline just above BX, and over a period of 11 days on the baseline below BX. The initiation of the rise occurs 9 days later on the downglacier baseline. The finite strain measured above BX was -0.596, and below BX was -0.730.

2.5.2 Strain Rate Based on Automatic Short Baseline Measurements

Method of calculation

Longitudinal strain was measured by short baseline strain meters at two locations in the terminus region during the passage of the front. One site (BX in Figure 2.1a), located approximately 45 m northeast of site B at the end of the surge, operated between 6 and 12 June, 1983. A lower site (DX) was located about 40 m southwest of site D and operated between 14 and 29 June. During these periods the change in length of a baseline was automatically measured and recorded, every 30 minutes at BX and continuously at DX.

Changes in baseline were measured by an LVDT transducer mechanically coupled to two aluminum piers set about 2 m deep in the ice. The initial length of the baseline was 1.5 m at BX and 1.4 m at DX. Neither the piers nor the strain meters were buried in snow to maintain a constant temperature. This would have been impractical at these sites since the snow cover had melted away, and was not critical to the accuracy of the measurements because the strain rates were so high. The piers were not actively frozen into the ice. This was generally not a problem because the longitudinal compression kept the piers gripped firmly in place. In brief episodes at both sites, however, the piers were forced up out of their holes, or twisted around a vertical axis, causing artifact extensions which were measured and removed in the data reduction.

The displacement data were recorded on chart recorders. Strain rates were calculated by dividing the recorded changes in length by the 30 minute intervals at BX, and by measuring the slope of the continuous record at DX. Total logarithmic strains were determined by integrating the calculated strain rates. (This is valid when the strain being integrated is coaxial.) At both sites, the pier spacing was measured manually at regular intervals, and the finite strain determined in this way was compared to the recorded strain data. This provided a verification of the automatic record at DX. At BX, ambiguities in the

periodically recorded data caused an uncertainty as to the magnitude of the total strain, and the manual measurements were used to scale the automatic data. Because of the high strain rates and large total strains, manual measurements of pier spacings were sufficiently accurate to be used as data together with the automatic recordings.

Data and discussion

The record of strain rate at BX is shown in Figure 2.9a, and the record at DX is shown in Figure 2.9b. The record at DX is most complete and shows the following pattern of strain rate: a very compressive initial phase, 24 hours or more in length, terminated by a sudden drop to a level about half that of the maximum phase, and then a series of lower level compressive events lasting a day or less, generally terminated by sudden drops to near zero or extensile strain rates. On a 15 minute or finer time scale the strain rate is erratic, showing rapid variations of about 20-30 % of average values.

The strain rate record at site BX starts 8 days after the arrival of the surge front at the site, so the compressive phase at the start of the record does not correspond to the first arrival of the surge. The high strain rate at 8 - 9 June ($\approx -0.08 \text{ d}^{-1}$) is the maximum value measured at this site, however. The strain rate at BX should be compared to the strain rate records shown in Figure 2.8. The strain meter at BX was located at the common point of the two baselines used in the calculation of Figure 2.8a and 2.8b. While the time of onset of the three records is spread over 9 days, all show a significant drop in compression on 9 June, constituting in all three records the termination of the phase of maximum compression. Of particular interest is the excursion into tension (to $+0.1 \text{ d}^{-1}$ at BX) shown in Figures 2.9a and 2.8a. These were measured by completely independent means, and represent a real tension event. This occurred during a significant glacier-wide slowdown on 9 June (see Kamb et al, 1985, Fig. 5) and is probably a consequence of the slowdown, rather than a typical feature of the strain rate pattern, to be expected at any other site. Two more compression events follow the termination of the maximum compression phase, one between midday on 10 June and midday on 11 June and the second from early on 12 June to the end of the record. These events show elevated but variable compression (up to -0.06 d^{-1} , with average rates of about -0.02 d^{-1}). Both events are initiated by a rapid rise.

Measurements at site DX (Figure 2.9b) were started before the arrival of the surge front, and the onset of compression (on 16 June) is very clear. Prior to the onset of

compression, the record shows a very weak but variable strain rate, mostly in extension at $0.001\text{--}0.002\text{ d}^{-1}$. A stronger extension event occurs two days before the onset of compression, during which the strain rate briefly reaches 0.01 d^{-1} . Temperature effects may be the source of the strain rate at these low levels, although higher sites in comparable circumstances showed much more stable near-zero strain rates before the onset of compression. Strain rates in the maximum compressive phase reached $\approx -0.13\text{ d}^{-1}$, and were terminated by a drop on 17 June, followed by a series of lower level compressive events. The very sharp termination of maximum compression such as occurred on 9 June at BX is absent, as anticipated, and while the drop on 17 June is a distinct reduction from the maximum levels, another drop on 19 June reduces strain rates nearly to the level observed before the arrival of the front.

The lower level compression following 19 June has a very complex structure, but includes four distinct "relaxation events" of reduced compression with their own characteristic structure. These are the 19 June drop, and three more on 21, 22, and 23 June. All are started by a very brief drop to a low compressive level, and immediate return to nearly the pre-existing level, and then a gradual decline to lower levels for the duration of the interlude. Strain rate rises sharply again at the end of the interlude to start the next compressive phase. A similar structure is visible in the record at BX. There, the tension event of 9 June, which terminates the maximum compressive phase, is itself terminated by a compression spike, which in turn subsides to lower compressive levels.

Sudden drops in strain rate might be caused by fault motion in the region near the strain meter site. Thrust or reverse faulting, occurring in response to longitudinal compression, will result in longitudinal shortening over baselines crossing the fault, and cause a temporary reduction in longitudinal stress and strain rate. If the reduction of stress is large enough, some elastic strain may be released adjacent to the fault, and a short episode of extension like the 9 June event at BX could be recorded over baselines which are also adjacent to the fault.

The relaxation events at DX follow a diurnal pattern, with the initiating drops in compression occurring in early evening, and the interval of low strain rate lasting through the night. Another reduction of compression also occurs on the night 20 June as well, but does not have the sharp character of the events already mentioned. This periodicity may be an instrumental effect, or the result of pier melting, but the strain rate fluctuations may

be closely controlled by some diurnally cyclic process such as englacial water flux. The discharge at the terminus stream at the time of these events was not strongly periodic, however (see Kamb et al, 1985 Figure 10). This brief correspondence between strain rate variations and time of day does not provide strong evidence that there is some diurnal control of short-baseline strain rate. The suggestion is plausible, however, and should be kept in mind when interpreting related measurements.

2.5.3 Synthesis of Estimates of Finite Strain in the Terminus Region

The total finite strain accumulated in the terminus region during the surge estimated from these different sources of data are compared on a longitudinal profile of longitudinal compressive strain in Figure 2.10.

The data in Figure 2.10 come from the three sources described above. First, the integrated strain rates presented in the preceding section cover most of the terminus region, and are a reliable measure of strain for the period 21 June - 5 July. Since points on the terminus profile above $XP = 18.0$ were already activated by the surge on 21 June, the strain profile above $XP = 18.0$ does not represent the total strain accumulated during the passage of the surge.

The second source is the short-baseline strain meter data. Direct measurements of pier spacing are a more reliable source of total strain information than integrated strain rates, since gaps in the strain rate data can add up to large errors in the accumulated strain. The integrated strain rate at site DX is included for comparison. It is 17% less than the strain determined by the pier spacing. Pier spacing measurements should be an accurate measure of total strain, given the large finite strains developed at these sites (-0.391 at DX and -0.467 at BX), and assuming that the strain meter baseline was coaxial with the principle compressive strain. The accumulated strain at a strain meter is not necessarily the same as the strain averaged over a larger region, however, if the strain is not longitudinally homogeneous. For example, fault motion like that discussed in connection with the relaxation events in the strain meter records would appear as an increment of compression over a long baseline crossing the fault, but would not appear or would possibly appear as extension at a short baseline strain meter on one side of the fault. Consequently, while pier spacing measurements are a good measure of local finite strain, they will not necessarily

agree with other equally good measurements made over longer baselines.

The third source of finite strain data comes indirectly from surveyed thickness differences before and after the surge at points fixed in the ice. The thickness change gives the depth-averaged vertical strain, which, assuming incompressibility and plane strain, equals the negative of the depth-averaged horizontal (longitudinal) strain. This in turn is the longitudinal strain at the surface if the flow does not vary with depth. (This is shown to be a good assumption in Chapter 4.) Longitudinal finite strains are estimated from thickness changes using the terminus profile data between $XP = 17.4$ and $XP = 18.5$ and using more widely spaced lower glacier survey data between $XP = 16.9$ and $XP = 18.0$. The coverage from the two sources overlaps, but they can be expected to agree only at the very end of the overlap at $XP = 18.0$, since above this point, the terminus profile strains are incomplete. This shows in the figure as a marked drop in the terminus profile strain between $XP = 18.1$ and $XP = 18.0$.

A source of error in the estimates of longitudinal strain from measurements of vertical thickness change arises if not all the vertical motion is due to straining of the ice. This problem is dealt with in Chapter 4. For the present purpose, we will simply use the results found in that chapter, namely, that approximately 12% of the thickness change caused by the surge occurs as the result of an increase in void space. Accordingly, the longitudinal strain based on thickness change is plotted both at face value, and with the final thickness reduced by 12%. Near the final position of the front, the figure of 12% becomes less accurate because the thickness change across the front is not fully developed. This can be seen in Figure 2.10, where the plotted values based on integrated strain rates and those based on thickness change agree more closely below $XP = 18.2$. The strain based on reduced thickness changes is not plotted all the way to the end of the profile, and presumably becomes less reliable as the downglacier end is approached.

The solid curve through the estimated values in Figure 2.10 is the best choice for a longitudinal profile of finite strain. In picking the curve, the most reliable estimates have been given greater weight. In the upper end of the profile, the estimates based on the complete thickness change modified for a 12% excess thickening are used, while at the maximum strain, a mean of the various closely spaced values is used. Below the maximum, the integrations of terminus profile strain rate are accurate, and are chosen over the thickness change estimates.

The maximum compressive strain developed in the terminus region during the surge appears in the thinnest ice which passed all the way through the surge zone. The maximum value is -0.75, which in terms of Lagrangian strain, corresponds to a 53% shortening. Downglacier from this maximum, the total strain diminishes rapidly in ice lying nearer to the final position of the surge front. Moving upglacier from the maximum, the total strain diminishes despite the fact that the estimates in this region include the entire episode of strain starting from the arrival of the surge front. Evidently, the total strain involved in the passage of the front is less in thicker ice. This makes sense qualitatively if the mechanism of advance of the surge front involves a thickening of ice until some threshold stress is reached. If the threshold stress involved is independent of the initial thickness, then the thickness change involved will be less in already thick ice, and the total strain will accordingly be reduced. Variations in velocity also contribute to the profile of finite strain. If the velocity of ice entering the front zone is increasing with time, the total strain involved in the passage of the front will increase with time as well. An episode of rising velocity will appear in the profile of finite strain as an increasingly steep gradient such as that between $XP = 17.4$ and $XP = 18.0$. Targets near the position of the surge front between 15 and 20 June, when the steepest part of the profile of finite strain developed (between $XP = 17.4$ and $XP = 18.0$) experienced maximum velocities at this time.

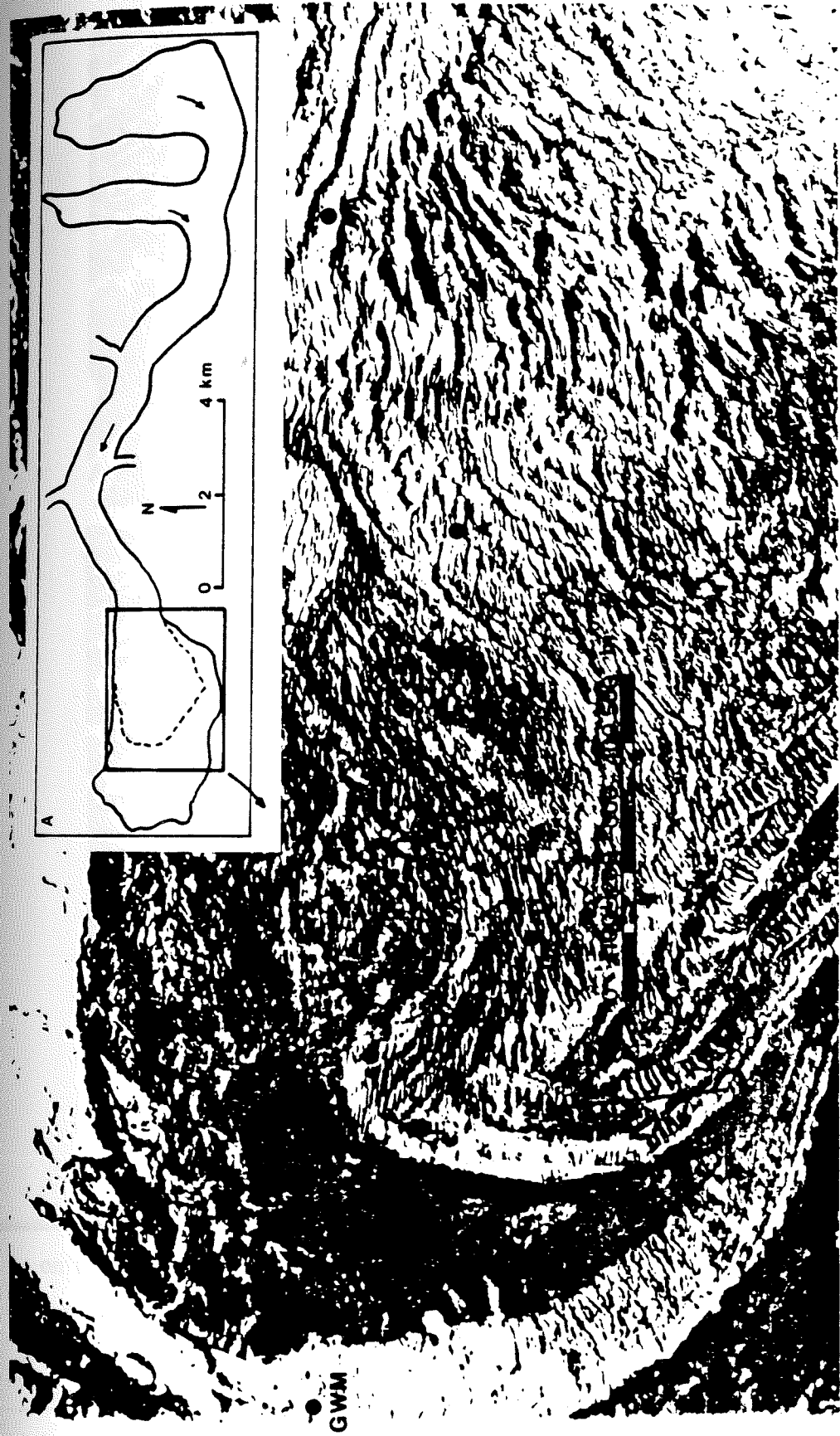


Figure 2.1. a) Terminus region of Variegated Glacier, showing location of reference markers.



Figure 2.1 (continued). b) Lower glacier and terminus region of Variegated Glacier on 18 June, 1983. Solid circles show positions of survey markers on 20 June, 1983. Open circles indicate markers no longer surviving on 28 August photo. Figure 2.1 (continued). c) Lower glacier and terminus region of Variegated Glacier on 28 August, 1983. Solid circles show positions of visible survey markers on 18 July, 1983.

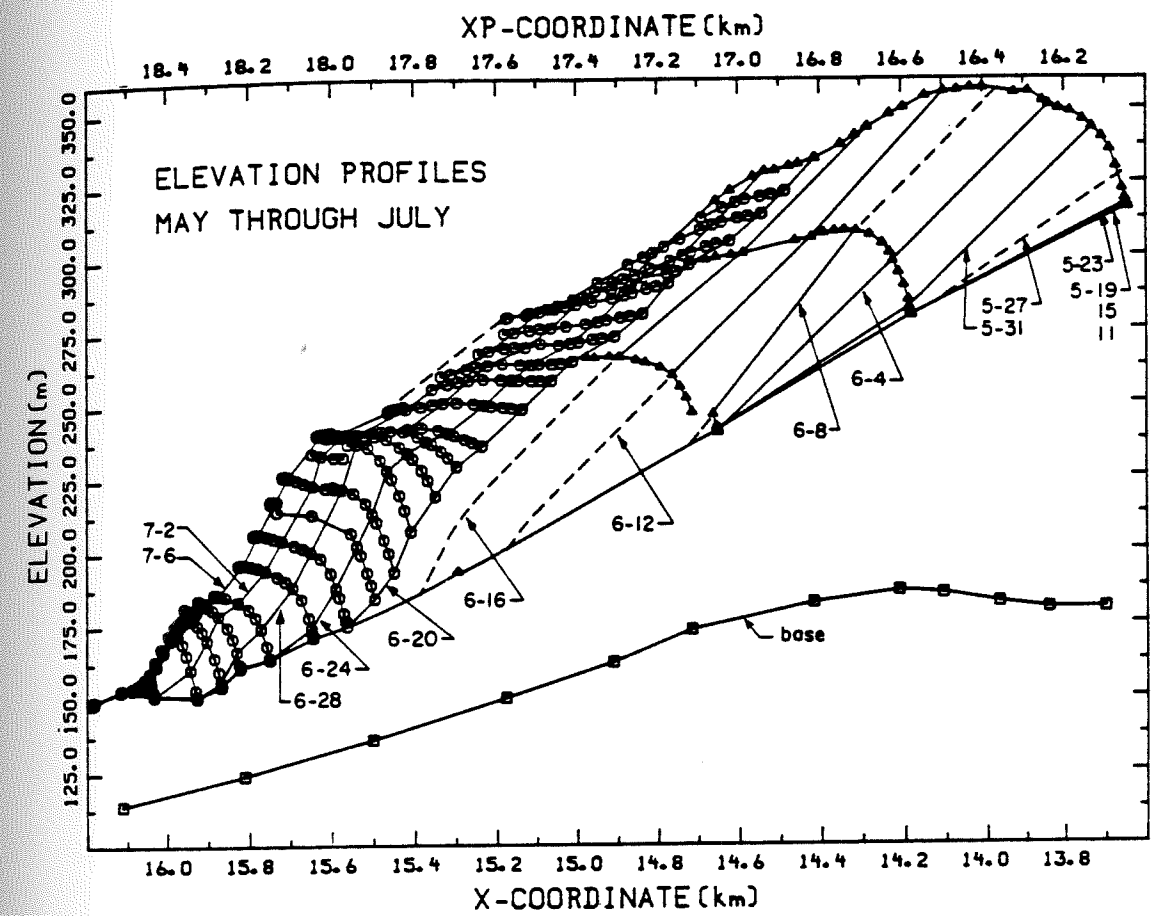


Figure 2.2. Longitudinal profiles of bed and evolving ice surface at selected times. XP denotes distance along centerline from the glacier head. Arcs show the space trajectories of markers.

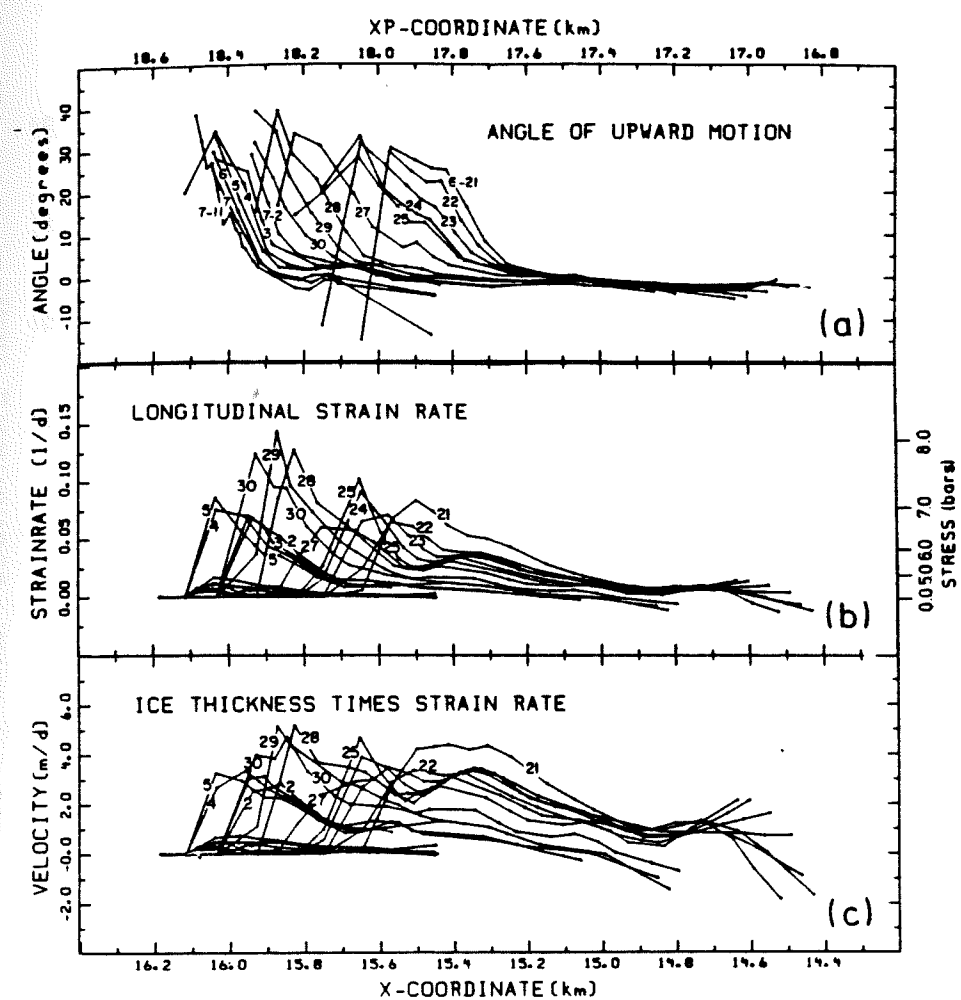


Figure 2.4. Longitudinal profiles of angle of (a) upward movement $\gamma = \tan^{-1}(v/u)$, (b) longitudinal compression rate $-\partial u/\partial x$, and (c) longitudinal compression rate times depth $-h\partial u/\partial x$. Longitudinal strain rate was computed from the longitudinal profiles of u in Figure 3b using optimal interpolation.

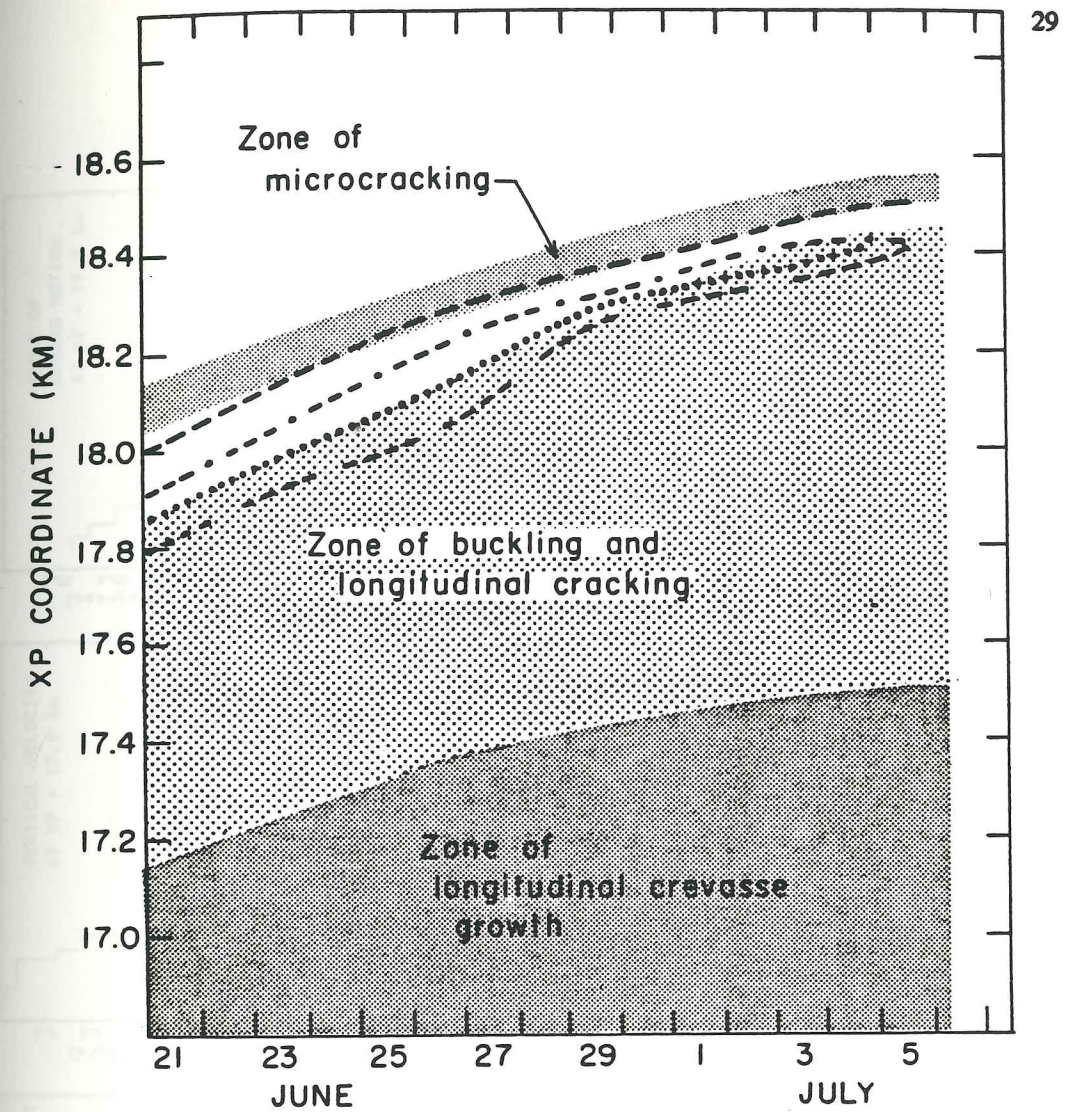


Figure 2.5. Longitudinal position versus time of the lower edge of the topographic and velocity fronts (dashed curve), of the peaks in angle of upward movement (dot-dashed curve), of longitudinal compression rate (dotted curve), and of vertical velocity (dashed-space curve). Shading shows zones of tectonic activity with approximate boundaries. Peaks in strain rate and thickness times strain rate coincide with the spatial resolution of the measurements.

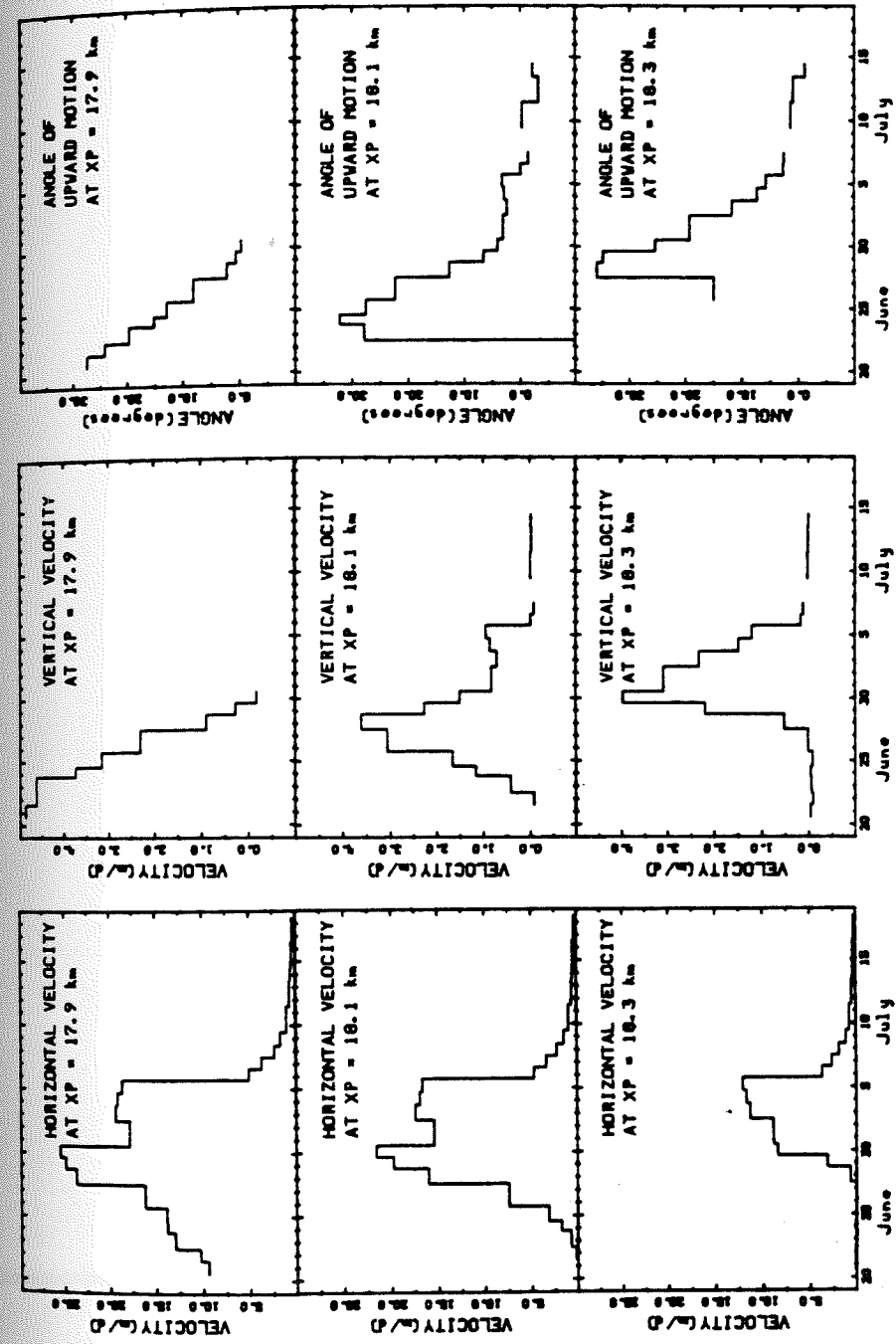
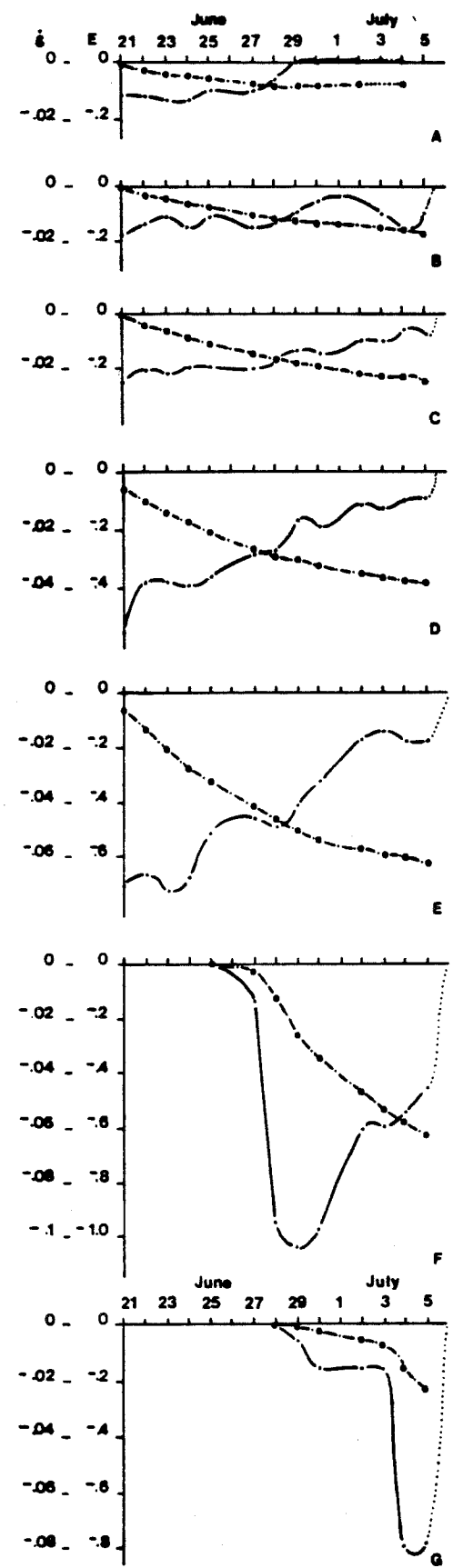


Figure 2.6. Variation of horizontal and vertical velocity with time at fixed locations.



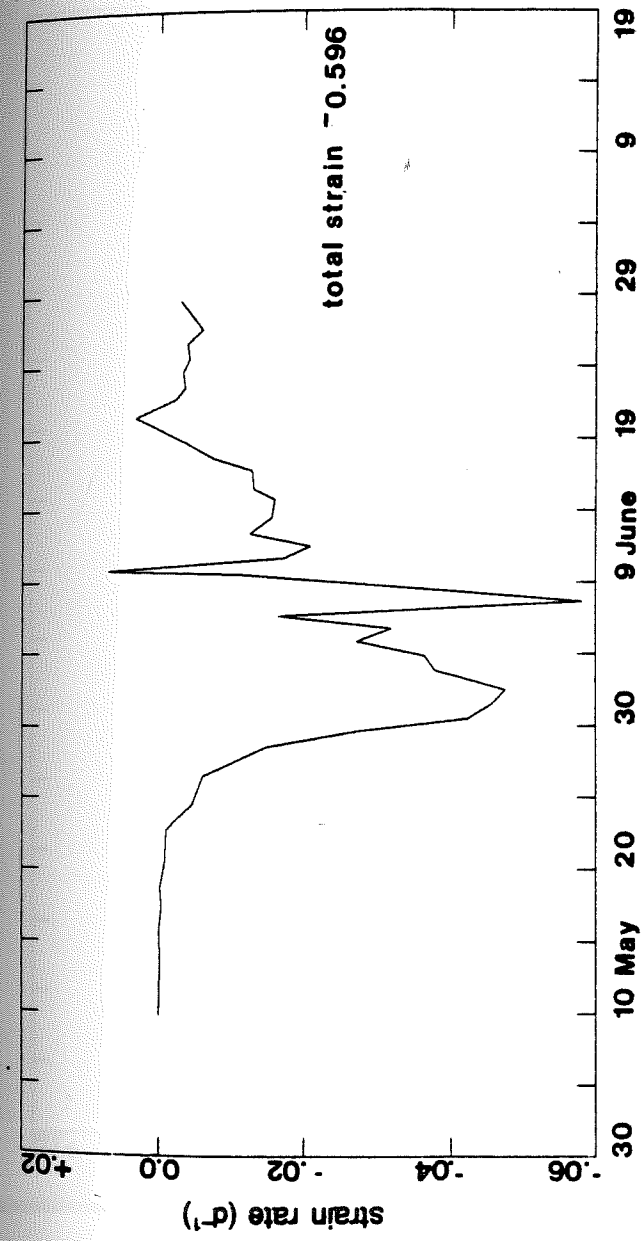


Figure 2.8. a) Strain rate based on survey data on 530 m baseline whose upglacier end is at site BX.

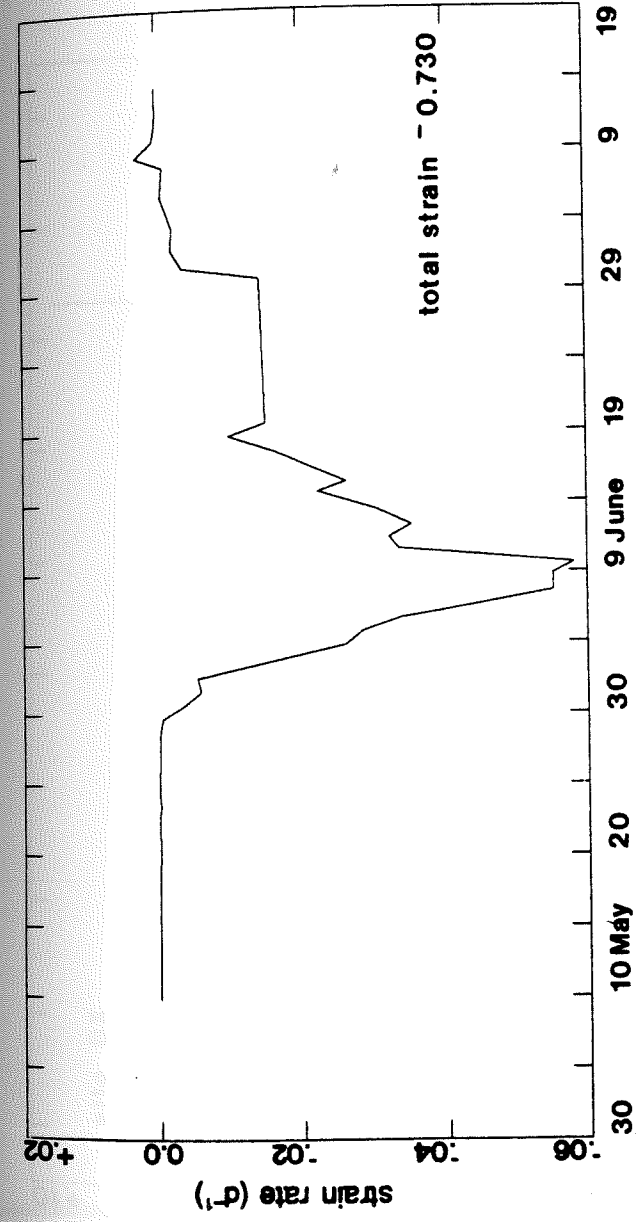


Figure 2.8 (continued). b) Strain rate based on survey data on 500 m baseline whose downglacier end is at site BX.

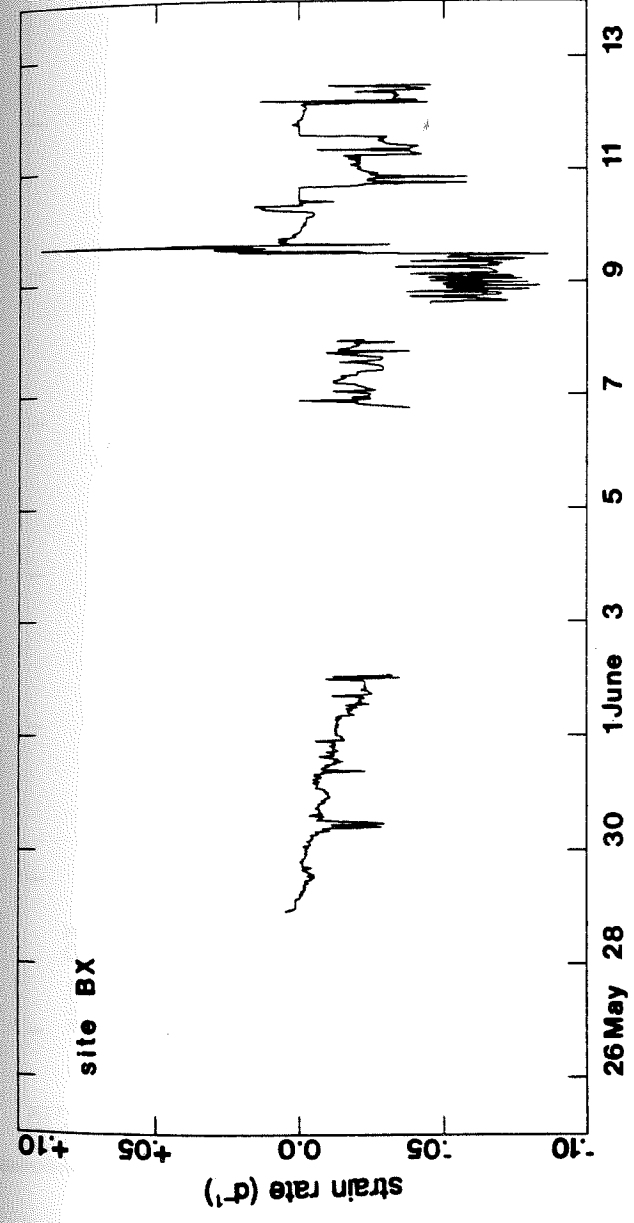


Figure 2.9. a) Strain rate recorded automatically on 1.5 m baseline at site BX.

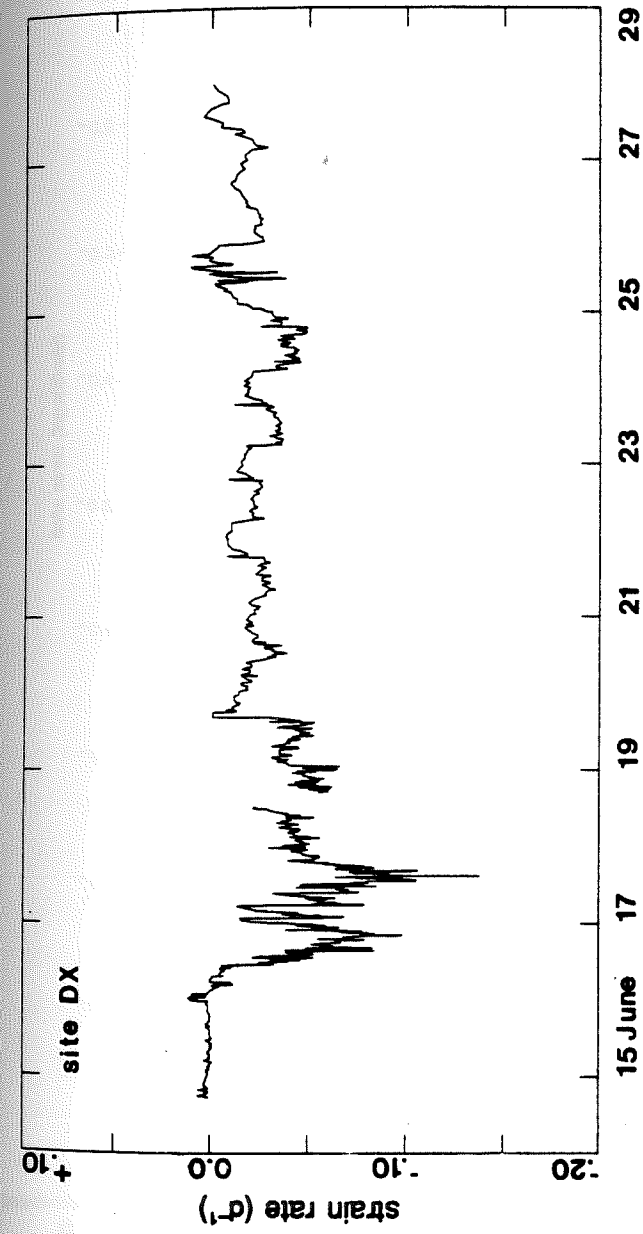


Figure 2.9 (continued). b) Strain rate recorded automatically on 1.4 m baseline at site DX.

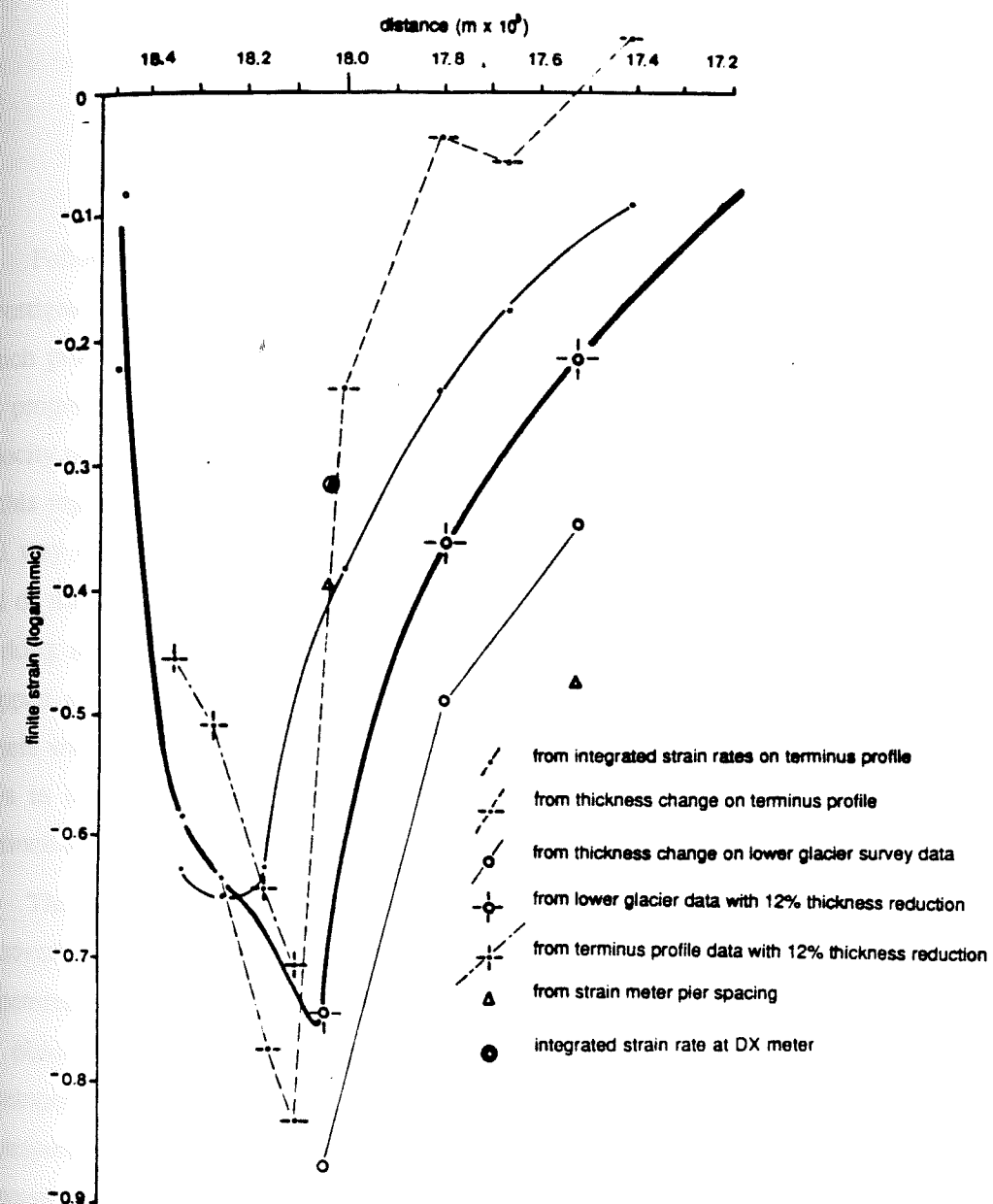


Figure 2.10. Profile of finite strain in terminus region calculated from various sources. Heavy line is optimum choice of finite strain variation.

CHAPTER 3

ENGLACIAL STRUCTURES FOLLOWING THE SURGE

3.1 Introduction

Following the 1982/83 surge of Variegated Glacier, an unusual opportunity arose to investigate englacial structures in a setting where a major part of the deformation history which produced the structures was known. A detailed observation was made in 1983 of the progress of the surge through the terminus region, as described in Chapter 2, including velocity profiles and tectonic developments. No detailed structural mapping had been done in this region prior to the surge, but the presurge state of the glacier was known in a general way from high resolution aerial photography taken at intervals between 1965 (at the end of the previous surge) and 1983, and from miscellaneous observations made by people working in and passing through the terminus region. Most important, the 1982/83 surge stopped short of the termination of the 1964/65 surge, leaving a zone several hundred meters wide in which the ice is still in its initial, pre-1983 surge state. Finally, annual surveys in the terminus region between 1973 and 1982 show that the ice remained nearly motionless during this interval.

The primary objective of a study of the structures in the terminus region is the discovery of a spatial pattern of evolution of structure associated with the surge motion. Structures found at each longitudinal position in the terminus region can be associated with the observed deformation history of ice found at that point. Estimates of finite strain developed in the surge front have been established, and it remains to compare them to the corresponding structures to develop both a relation between structure and deformation, and a sequence of intermediate stages leading to the final relationship.

The structural survey of the terminus region was undertaken in 1985 and 1986. The general strategy was to study in detail a zone corresponding to the terminus profile which provided the elevation and velocity data presented in Chapter 2, and to extend the survey to other parts of the terminus region by traverses taken out from the main study area. Another structural survey, conducted in 1986 and 1987 by workers from Cambridge University, will supply information on the whole glacier below the equilibrium line.

Two general categories of structure were studied, and the field work progressed along

two independent but related lines. First, a detailed survey and mapping was conducted of various structures: layering, foliation, folding, and faulting. This was done much like a traditional bedrock mapping project in structural geology. Second, optic axis fabrics were measured at sites along a profile through the map region. These two parts of the structural survey are presented separately, and their relationship is considered in a general discussion.

3.2 Presurge Conditions

Figure 2.1b, taken in July 1982, shows the condition of the glacier surface in the terminus region before the surge had entered the lower glacier. The area of interest lies on the upglacier side of the large white moraine (site of survey station GWM in Figure 2.1b), and extends up through the area of looped moraine structures into the narrower channel of the lower glacier ($XP = 15.0$). Not all of this area was mapped, but by July 1983, ice initially lying in this area had been compressed into the map region as discussed in Chapter 2 (Figure 2.1b and 2.1c).

There is a substantial change in the appearance of the glacier surface, evident in Figure 2.1b, which occurs at the position where the narrow lower glacier channel spreads out into the terminus region ($XP = 16.0$). Above this position, the ice is clean, with persistent and coherent longitudinal structures. Below, the structures are amorphous, fuzzy, and the ice is to a much greater extent buried in debris. There are also large looped structures visible on the south side of the terminus region. Horizontal velocities of 5 cm day^{-1} or less were observed in the terminus region prior to the surge during surveys conducted annually between 1973 and 1982. The vertical surface velocities associated with ablation were greater. Aerial photographs taken in 1974, however, show a slightly different picture of the terminus region (Figure 3.1): the same layout of structure is evident, but is more sharply defined and continuous. The fuzzy, broken appearance in 1982 is evidently the work of ablation, which redistributed debris in a more uniform blanket across the surface. The sequence of photographs taken between 1965 and 1983 suggest a kind of cycle of clarity in the surface expression of structures. In the years immediately following a surge, the remnants of the chaotic topography during the surge obscure the large view of structures, as was the case between 1983 and the present. Midway between surges, as in 1974, the redistribution of debris has stabilized somewhat. The structures and topography stand out most

clearly at this time. As the next surge approaches, continued ablation and redistribution of debris act to diffuse the small-scale patterns of topography and debris. This results in the loss of clarity evident between 1974 and 1982. Above the terminus region there has always been less debris and less local topography (as well as more downglacier flow), so the same cycle is not so evident there.

The uniform and thick (in places more than 1 m) debris cover in the lower terminus region before the surge prevented any casual observation of small-scale structures. Some large scale structures are visible in the 1974 photographs, however, which were covered by debris in 1982 but which were exposed again during the surveys of 1985 and 1986.

At the upglacier margin of GWM is a zone approximately 200 m wide which the 1982/83 surge did not enter (compare Figure 2.1c and Figure 2.2). The ice in this zone is composed of large (2-5 cm) interlocking crystals with varying degrees of bubble content. A strong horizontal foliation exists in ice at the very foot of GWM on the upglacier side, but weakens as it is traced upglacier. This will be described in greater detail in the following section.

Below GWM, ice has lain stagnant and covered with a very thick debris layer (up to several m thick) since the 1964/65 surge. Large collapse and settlement features are present in areas where old subglacial drainage systems are melting out. In many places, the ice below the debris cover is very large grained (10-15 cm) and almost entirely bubble-free. In other locations near GWM, strong subhorizontal bubble foliation is found. The attitude of the foliation is very irregular and it appears to have been deformed as the ice has flowed under the influence of small local topography. Flow into depressions and old crevasses, for example, causes the foliation to dip into the center of flow from all sides.

3.3 General Postsurge Conditions

In 1985, for the first time since the 1982/83 surge, the surface of the lower glacier and terminus region (below XP = 10.0) was easily accessible everywhere. A great deal of surface relief was still present, but only in the form of longitudinally elongated rounded hills approximately 10 m high and 100 m long. This topography appears to be the remnant of the ridge-and-chasm topography which existed at the end of the surge. The orientations

of the elongated hills and valleys matches those at the end of the surge; also, brecciated rock and ice debris are often found in the valleys, presumably the remains of the debris that filled the chasms during the surge. Prior to the surge, ice within about 1 km of GWM had a heavy mantle of debris; during and for a year after the surge, this debris cover was broken up by the displacement of the ice, but has since been redistributed through debris slides and ablation of the ice underneath. Upglacier from this debris-mantled area the ice surface is clear of debris (as of 1986), except for the north margin and a very distinct tongue of black debris extending downglacier from the margin at station MM (Figure 2.1c).

Underneath the debris cover, the ice throughout the terminus region is generally clean, with only occasional stones or dirt clumps appearing in excavations or visible within the ice. Exceptions to this are thin layers of debris associated with two of the categories of penetrative structures - the P and S₀ classes - to be defined in section 3.4.1. The ice is composed of large, elongated interlocking crystals, roughly 2 cm by 10 cm with tortuous, branching arms. No fine ice was found in the survey region within the limits of the 1982/83 surge. Some small layers of fine ice were found outside the survey region at two marginal sites, one at the upglacier foot of GWM in horizontally foliated ice just outside the limit of the 1982/83 surge, and another along the south margin in similarly foliated ice which was activated during the 1982/83 surge, but probably not subjected to much deformation.

Ablation reduced surface elevations substantially in the interval between July 1983 and July 1986 (Figure 3.2). Reductions in elevation range from 40 m at the upglacier end of the survey region to 10 m in the central part, to 30 m at the very bottom of the region. About 25 m of ablation would be expected in this area in 3 years. The greater change at the upglacier end was due to the very rough ridge-and-chasm topography in 1983, resulting in very rapid ablation there. Also, settlement at depth occurred after the surge in this region, as discussed in Chapter 4. At the downglacier end, the excess ablation was due to a change in surface drainage patterns: the low point in the 1986 profile marks the course of a new stream running transversely across the upglacier foot of GWM. Both GWM and the downglacier end of the survey region have experienced oversteepening and debris sloughs since 1983. In the central part of the survey region where ablation was a minimum, the survey profiles run through a deep east-west trending notch (formed by adjacent presurge

topography) and run through very thick debris cover. These may have sheltered the ice in this part of the profile and reduced ablation.

The main question raised by the comparison of these profiles is what the relationship is between the activity observed at the 1983 surface and the structures observed at the 1986 surface. This question is answered in detail in Chapter 4. For the present purpose it is sufficient to summarize the result presented there: the flow in the terminus region was almost completely independent of depth. Horizontal velocities at the bed of the glacier were very nearly the same as at the surface, and patterns of velocity and strain over time are essentially the same at all depths. This greatly simplifies the problem of relating observations in 1983 and 1986, and in subsequent discussions pertinent data such as strain rates, taken in 1983, will be regarded as directly applicable to the structures observed in 1986. Those phenomena of 1983 which pertained strictly to the surface at that time, e.g. buckle folds, are obviously excluded from this assumption. By 1986 all evidence of buckle folds and other such surficial tectonic developments had vanished.

3.4 Planar Structures in the Terminus Region

Structural mapping was concentrated in a strip roughly 1200 m long and 50 m wide laid out in the area of the terminus profile discussed in Chapter 2 (Figure 2.1a). Reference markers were set out and surveyed by theodolite and electronic distance measurements within this strip, and provided topographic information and reference points for placing individual measurement sites on base maps. Several traverses were made to extend the mapping out from the main grid. These were made laterally to the north and south, and also in the upglacier direction. Site measurements were made with a Brunton compass, and site locations were placed on base maps by estimating their position relative to nearby reference markers. The entire map region was photographed, and many individual measurement sites were photographed in detail.

3.4.1 Classification of Structural Types

A naming scheme has been developed to define and distinguish the types of structure and also to clarify their genetic relationship. Four sets of foliation are defined, and labeled S_0 , S_1 , S_2 , and S_b . Additionally, two fault or fracture-like structures are present, named P_0 and P_1 . The spatial relationship of the structures is shown schematically in Figure 3.3.

S_0 is a ubiquitous, subhorizontal, wavy or undulatory layering, formed of bubble density variations and debris horizons (Figure 3.4a). Individual layers are typically 10-20 cm thick. The wavy character of the foliation is defined by fold axes running across the glacier, i.e. an exposure running longitudinally shows the wavy pattern, but an exposure running across the glacier appears straight. This is shown in Figure 3.3. This relationship is reversed above the terminus region, where folding is about axes running longitudinally. S_0 is cut by all the other planar structures observed, and is folded wherever folding of any structure is present. In some locations in the terminus region, S_0 steepens abruptly and emerges at dips of about 20° - 30° (Figure 3.4b).

S_1 is a bubble foliation set in vertical planes striking transverse to the direction of flow (Figure 3.5). This foliation is not well developed by comparison with classic examples of foliation (e.g. Allen, et al (1960)) and does not have a continuous laminated structure, although such well-developed foliation was seen in other parts of the glacier. Rather, S_1 consists of flat clusters of bubbles approximately 20 cm in the transverse direction and 2 cm in the longitudinal direction, or an axial ratio in the horizontal plane of 1:10. Many closely spaced clusters of this shape set in otherwise clear ice produce an easily recognized, orientable foliation. The foliation is difficult to photograph, however, since without any continuous traces of laminae running along the surface, one needs binocular vision to see the foliation clearly. For the same reason, it was impossible to measure individual folia. The axial dimensions of 20 cm to 2 cm are an estimate, and were confirmed by an identical estimate made independently (W. Lawson, personal communication).

S_2 is a pervasive set of hairline cracks, dipping vertically and striking in the longitudinal direction (Figure 3.5). Frequently fine bubble trains surround and extend from the ends of the cracks, and sometimes appear alone without a crack. In addition to the hairline cracks, small crevasses exist in the S_2 orientation, usually occurring in longitudinally elongated fields about 10 m in length (Figure 3.6). These crevasses are as wide as 10 cm

and up to about 3 m long. They were usually full of water when observed, but when probed were about as deep as they were long. They are not new crevasses (i.e. post-surge), being obviously affected by ablation as much as any other feature on the surface.

A set of subhorizontal foliation, S_b (Figure 3.7), appears at the very downglacier edge of the survey area, and continues downglacier a short distance past GWM. This is a very well-developed laminated foliation and is in ice very near the base of the glacier. The foliation consists of thin (≤ 1 cm) sharply defined layers of milky ice separated by thinner bands of less bubbly ice, and in one instance, layers of fine ice (grain size ≈ 1 mm).

There is another class of named structural features in the terminus region, but these are not as well defined, either in orientation or proposed origin, as the S class. These, the P features, are extensive single planes, usually containing a fine dirt horizon (Figure 3.8). Large-grained clear ice lenses also appear at the P interface, typically about 1 cm or less in thickness with C-axes in the clear ice oriented perpendicular to the P surface. The P's strike roughly transverse to the flow direction, are somewhat convex downglacier, and can extend several hundred meters along their strike. They always dip upglacier, but seem to fall very approximately into two sets: those roughly parallel to, or extending up out of, S_0 ; and another set dipping between 60° and 90° . These are designated the P_0 and P_1 respectively. The P_0 is also distinguished by occasional thick layers of debris, including cobbles up to about 5 cm. P_1 on occasion contains small stones (≤ 1 cm), but is more typically marked only by fine dirt. The majority of P fall into the P_1 set. Neither the attitudes of the P's nor the location or grouping in map view shows any of the consistency or classifiability of the S class. Representatives have been recorded where present, but they appear to be independent of the S structures. There is evidence of displacement on certain P features, but no unequivocal indicators of the direction and magnitude of displacement could be found.

The P features are given a separate name from the S class to emphasize the important differences between them and the members of S: they are not penetrative, in the sense that they are isolated planar structures even at the map scale; and they are structures which were developed as a consequence of deformation (unlike S_0), but probably at some earlier time and at some other place than their position in 1986, and as such are not direct products of the surge.

3.4.2 Interpretation

Integrated picture of the penetrative structures

The distribution and representative orientations of S_1 and S_2 are shown in Figure 3.9 (map pocket). S_0 appears throughout the map region, so it is not included in the figure. The outcrop edges follow the surface contours, since S_0 is essentially horizontal. Table 3.1 lists the coordinates of the reference markers shown on the map, in the coordinate system described in Bindschadler et al (1977).

Table 3.1

Site	X-coordinate	Y-coordinate
A	15011.3	2961.9
B	15268.4	3026.9
C	15409.6	3055.5
D	15599.4	2994.0
E	15767.7	2893.6
F	15929.8	2798.3
G	16061.7	2740.0
H	16185.6	2669.2

In the most general terms, we believe that S_0 is original depositional layering, S_1 and S_2 are products of the 1982/83 surge, and S_b is produced by base-parallel shear over times much longer than any one surge. The category of P_1 we believe to be structures - probably closed transverse crevasses - created somewhere higher on the glacier and transported into the terminus region with little accompanying deformation. P_0 may have the same source, but its orientation relative to S_0 is hard to reconcile with an initially vertical orientation. More probably, P_0 are unusually prominent angular unconformities in S_0 .

An understanding of the unusual character of the flow in Variegated Glacier over the course of a surge cycle is fundamental to this interpretation. Before proceeding to a detailed discussion, it should be brought to mind that the main feature of surging flow - rapid sliding with little deformation in the main body of the glacier - causes ice and the structures in it to be transported large distances downglacier with very little of the shearing

deformation associated with structures seen in the termini of non-surging glaciers. A simple calculation using the typical surge displacement and non-surge velocities ($\approx 150 \text{ m yr}^{-1}$) on Variegated Glacier together with the length of the glacier and the duration of the surge cycle shows that a structure formed in the central part of the glacier will be carried further by surging motion in 1 year of the 20 year surge cycle than by ordinary motion during the remaining 19 years. About 3 surge cycles are required to carry ice from the central part of the glacier to the terminus. Accordingly, ice flows in a quiescent mode for a total of about 57 years and in a surging mode for about 3 years in its course from midglacier to terminus. During the surging mode, shearing strains are confined to narrow bands at the base and at the margins (see, for example, photographs in Kamb et al, 1985). The bulk of the glacier is moving at high velocity with only small strains of any kind developing, except at the surge front, where high longitudinal compression develops in plane strain. In the intervening non-surge years, sliding velocities still develop which are moderate to high by non-surge standards (Evolution of Variegated Glacier, Alaska, U.S.A., Prior to its Surge. C.F. Raymond and W.D. Harrison. manuscript submitted.) so base-parallel shear is low relative to non-sliding glaciers. Quiescent marginal shear strains are on the order of 0.05 yr^{-1} (Bindshadler et al, 1977) on the lower reach of the glacier, but structures developed here are obliterated in the shear zones developed during the surge.

At the upglacier end of the survey region only S_0 , P_0 , and P_1 are evident. The ice here and at points upglacier is uniformly bubbly and has a milky appearance. The bubble density variations which define S_1 are absent. (Far above the terminus region, various foliations appear, but these are separated from the foliation in the terminus region by a gap of about 1 km.) The small cracks which define S_2 are present, but not in the abundance found further downglacier. Relatively large local topography helps to bring out S_0 and P , since these are more noticeable in steep exposures, especially those facing transverse to the direction of flow. S_0 is fairly uniform in layer thickness, usually being 5-10 cm. No dramatic exceptions to this appeared anywhere. Small-scale (10-20 cm) fold-like features appear regularly in S_0 with axial planes oriented transversely. These are probably the result of amplification of pre-existing irregularities by longitudinal compression rather than buckling. It was noted (W. Lawson and M. Sharp, personal communication) that along the margin above the terminus region similar fold-like features appear with their axial planes oriented longitudinally. This was seen below a zone of longitudinal extension at $XP =$

10.0, and passive amplification by lateral compression again offers an explanation consistent with the direction of principal strain.

The occurrence of P appears to be most frequent in the upper part of the terminus region, but this may be due to the absence of debris cover here. The P features are large but widely (several hundred meters apart) and irregularly spaced, so they are likely to be missed if they are sought by sampling through excavations in debris.

Moving downglacier into the central part of the survey region, S_0 and P persist, S_1 appears, and S_2 becomes more abundant and consistent in orientation. The orientation of S_2 is somewhat scattered in the upper end of the survey region, but is confined within about 10° of the flow direction. By the middle part of the survey region, strikes are quite consistent locally, with some variation occurring in organized patterns. S_2 dies out several hundred meters above the final position of the surge front. Finite element calculations indicate that maximum stress levels were reached within the front itself, so evidently some activity within the zone above the front ramp is involved in the formation of S_2 , or else it would have been traceable all the way to the front. Alternatively, the heavy debris cover in the lowest part of the terminus region may simply obscure S_2 , which is not as completely pervasive as S_1 and could therefore be missed. Sampling in the debris cover was sufficiently dense, however, that the relative absence of S_2 definitely represents some marked decrease in its occurrence.

S_1 appears pervasively in the upper survey region as soon as the bubble content becomes sufficiently variable for a bubble-density foliation to exist. It persists throughout the middle and lower survey region until part way down the topographic ramp of the surge front. The visibility of S_1 varies somewhat where it exists, but tends to intensify somewhat in the downglacier direction, and is traceable virtually anywhere one looks until its disappearance at the surge front. In the debris-covered part of the terminus where S_2 becomes scarce, S_1 is still present in all sites excavated. About half way down the topographic ramp, S_1 vanishes over a zone about 5 m wide and running transversely across the front. Its presence on one side of this zone and absence on the other was verified by an especially dense sampling of sites.

In exposures cut by the drainage stream running transversely across the upglacier foot of GWM, the very distinct horizontal S_b foliation is obvious. S_b can be traced back

upglacier several hundred meters from the stream exposures to the zone where S_1 disappears. S_b persists with a progressive weakening of the intensity of foliation, but still easily traceable upglacier in continuous exposures in a stream cut, until it vanishes abruptly at the downglacier edge of the zone. Within the zone itself, a very vague organization of bubble density is present. Amorphous, ropey structures are discernible, but have no planar structure. S_b can also be seen in exposures on GWM and near GWM on the downglacier side, but is not generally present in the old ice outside GWM.

Origin of structures

S_0

S_0 is evidently the earliest generation of structure present in the terminus region, for any deformation or displacement observed invariably involved S_0 . This fact, the ubiquitous occurrence of S_0 , its subhorizontal orientation, the continuity of its layers, commonly occurring debris layers, and the aforementioned fact that structures can be carried long distances downglacier by the surge motion with little deformation, lead us to the conclusion that S_0 is primary depositional layering.

S_2

The orientation and consistency of S_2 suggest that these features formed in response to transverse lateral extension or longitudinal compression, or both, in the surge front. It was between the upper and middle parts of the survey region that the surge front developed a really well defined topographic ramp, and this may be an expression of the same large-scale organization of stress that produced the change in consistency of the S_2 strikes. S_2 cracks were observed on 2 July 1983, in an orientation perpendicular to the observed local direction of extension rate (Raymond et al, 1987). Moreover, the time of maximum extension rate occurred after the time of maximum compression rate, and after a change in the principal stress directions. Unlike most interpretations of foliation, S_2 is unrelated in orientation to the finite strain in the locality. Rather, it was created by a transient orientation of maximum extension rate which caused the rapid development of a pervasive set of cracks and crack-related features.

S_b

The S_b foliation appears to be the product of large shear strain parallel to the bed (the C-axis fabric measured at this site supports this, as will be discussed in section 3.5).

Additionally, the glacier is less than 40 m thick at this site, so the ice exposed at the surface now was very near the bottom of much thicker ice in the past. It is reasonable to conclude that ice so near the bed of the glacier was included in the narrow zone of intense basal shear during one or very possibly several surges in the past, or has been in constant shear strain at very low levels during quiescent phases. The presence of S_b on GWM requires additional consideration, for the locations here are at considerably higher elevations than at the upglacier foot of GWM where S_b is so well developed. Some complexity in the flow may have existed at GWM during the 1964/65 surge, for photographs taken in 1965 show a significant shift in crevasse patterns at this position. S_0 may have provided an original inhomogeneity for S_b , but it is hard to see how S_b could be formed simply by vertical compression of S_0 , for many characteristic features of S_0 (as well as features typically found with S_0) which one would expect to be preserved by compression, are absent. These features include, most notably, dirt horizons in S_0 and P features.

The relationship between the present distributions of S_0 and S_b is unclear. No evidence of S_0 was found in the region where S_b is present, but it may be present and obscured by debris cover. The general impression while working in the region was that S_0 is absent, which would be consistent with the idea that S_b is formed as the consequence of large shear strains. The best conclusion to make with the information at hand is that S_b is the product of large base-parallel shear strains, in which S_0 may have served as a primary inhomogeneity, or may have been obliterated. A large area of ice in the region of S_b would have to be cleaned of debris and a more detailed survey made to further resolve this issue.

S_1

The appearance of the amorphous bubble distribution in the transition zone between S_1 and S_b might lead one to conclude that S_b is being destroyed by some process which simultaneously produces S_1 as the zone moves downglacier. The transition from weak S_b at the downglacier edge of the zone to the amorphous structure within the zone is gradual and continuous, while the transition from amorphous to distinct S_1 at the upglacier edge is quite rapid, but nonetheless smooth. Some process, presumably deformation within the moving surge front, has evidently converted unfoliated ice, and possibly horizontally foliated ice, into ice having a vertical transverse foliation. Referring back to Figure 3.2, it can be seen that before the surge, the transition zone lay in a rather flat portion of the terminus region, undistinguished by any special topographic feature. The 1964/65 surge extended

past this point. In short, the only event or feature of significance associated with the location of the transition zone is that it coincides with the final position of the 1982/83 surge front. It could be established unequivocally that S_1 is the direct product of the passage of the 1982/83 surge if a survey conducted before the surge showed no signs of S_1 , but this was not done. Nevertheless, the disappearance of S_1 at the front argues strongly that S_1 is a product of the 1982/83 surge. The progressive weakening of S_b moving upglacier from the foot of GWM is probably independent of action within the transition zone, and only reflects exposure of ice closer to the bed at the downglacier end of the survey region. It is possible that the postulated conversion of S_b to S_1 could not have happened to the most well-developed S_b observed.

Hooke and Hudleston (1978) consider foliation to be a product of passive deformation of some existing inhomogeneity, rather than the result of bubble migration in the ice. If deformation is to be the source of S_1 , however, the strains measured in the terminus region should be comparable to the strain required to produce the anisotropy of the bubble distributions in S_1 .

The initial state of the ice is not precisely known. The S_b foliation on the downglacier side of the S_1/S_b transition is probably not typical of the initial state, for S_1 appears throughout the terminus region above the surge front, while S_b is evidently limited to ice near the bed of the glacier. The S_0 layering is a better choice for the initial state of the ice, but there are no good examples of this in its pre-surge condition. The best choice for a representative of the initial condition is the ice in the transition zone between S_1 and S_b , where no foliation is present, but only a patchy, inhomogeneous distribution of bubbles. This also agrees with the appearance of isolated sites upglacier where S_1 was absent: bubbles were present, not uniformly distributed through the ice, but in scattered patches with no particular elongation.

If the S_1 foliation is to be created from isotropic patches of bubbles, the compressive strain required to produce the observed horizontal axial ratio of 1:10 in the resulting folia is -2.3 (logarithmic), assuming plane strain in a vertical longitudinal plane without volume change. This is much more strain than was observed in the surge front, where the maximum compression was -0.75. The longitudinal strain required to produce a 1:10 axial ratio in a horizontal plane can be reduced by assuming other modes of strain: in uniaxial compression a strain of -1.53 is required, and in horizontal plane strain only -1.15 is

required. These are still not consistent with the measured strains, and in any case are not plausible modes of deformation given that only very small lateral extensions were observed. Furthermore, the very sharp zone where S_1 disappears is not located in the region of the terminus where the maximum strain is calculated to have developed (at $XP = 18.0$). It is 400 m downglacier from this, at a point more closely associated with the furthest downglacier extent of the high stress at the leading edge of the surge front.

If we reject the possibility that bubble migration is involved in the formation of S_1 , we are left with the possibilities that the estimated axial ratio of 1:10 is incorrect, or that the initial state of the ice was not isotropic. It must be emphasized that the estimated axial ratio is very approximate, although it was reached independently by two observers. The discrepancy in strain cannot be simply ascribed to faulty estimates, however, since the maximum observed strain of -0.75 would produce an axial ratio of only 1:2.1, which is entirely outside the range of possible ratios, as is evident even in the photographs of S_1 (e.g. Figure 3.5). In connection with the visibility of S_1 , we note that since the principle extension direction was vertical, the bubble anisotropy of S_1 should be much more pronounced in vertical exposures. Such exposures were occasionally found, and S_1 was quite clear in them, but such exposures were generally very small and tended to be weathered. Horizontal exposures of S_1 were predominant because ideal viewing conditions were created by washing away pools of mud from flat surfaces, which left a very smooth, unweathered surface.

If the initial condition of the ice was not isotropic, then either the ice was visibly foliated, and no areas of foliated ice are left outside the limits of the 1982/83 surge, or the bubble distribution was anisotropic in transverse planes, but not to an extent which resulted in visible foliation. This latter case is especially probable given the tenuous character of the final state of S_1 . It is possible that a longitudinal extension of the same magnitude as the measured compression in the terminus region might be sufficient to render S_1 essentially invisible. This is a difficult assertion to test quantitatively, since it is so dependent on the perception of patterns in three dimensions.

The remaining consideration in explaining the origin of S_1 is the possibility that bubble migration is involved. Bubble migration is not well understood, but has been observed under conditions similar to those in the surge front. Kamb (1972) observed bubble migration under biaxial compression at 6.4 bars at 0°C. He did not discuss this observation in

that paper. What stands out in the present situation is that the S_1 foliation (if not already present) was evidently produced very rapidly during the advance of the surge front, and that its downglacier limit corresponds to the final position of the front but not to the point at which the finite strain was sufficient to produce it by deforming initially equidimensional bubble clusters.

The final point to be addressed involving S_1 is the question of whether it can be expected to persist from one surge to the next, or whether by some mechanism it weakens in the interim. Annealing may occur in the interval between surges, bubble diffusion may be significant, and spreading of the ice during the stagnant phase may contribute a small amount of extension. No firm conclusion can be reached about the extent to which S_1 may deteriorate between surges, but some change cannot be ruled out. If S_1 does persist between surges, then the question arises as to where previous generations of S_1 are. If S_1 can persist between surges, then the possibility is open that finite strain accumulated over several surges has produced the observed foliation. This does not explain the abrupt disappearance of S_1 at the edge of the most recent surge, however.

P

The various features in the P category are quite distinct from the other planar features found in the terminus region, but we do not have a definite origin assigned to them. They are larger and more continuous than the other steeply dipping features found in the region, and are particularly distinctive because of the dirt or debris layer typically found along them. This ranges from a thin (≤ 1 cm) lens of clear ice discolored by fine dirt on P_0 and P_1 to layers of mud and cobbles up to about 5 cm on some P_0 . The P's are not easily visible in aerial photography taken since 1983 owing to the chaotic surface, but similar features are visible in the 1974 photographs. The P's evidently extend quite deep in the glacier, and persist after ablation has removed the smaller obscuring features near the surface. They will probably become visible again in about 10 years.

There are three main questions to be answered relating to the P category. First, what kind of structure are they? Possibilities include closed crevasse traces, old ablation surfaces, and faults. Second, is P locally formed or is it carried into the terminus region from above? Finally, is fault motion along P involved in the deformation during the surge? This is a possibility whether P originates as faults or whether P surfaces have a separate

origin and become activated as faults during surge activity.

The **P** category probably originates upglacier and is carried into the terminus region. Two separate origins are proposed for P_1 and P_0 . In neither case does fault motion seem to be a realistic origin, for very large displacements (corresponding to the distance along the slip plane to the bed) would be required to entrain the quantities of debris observed. Nowhere on the glacier, either during the surge or before, was faulting of sufficient magnitude observed. The remaining possibility is for debris to be introduced from above when the **P** are open surfaces. We propose that P_1 are formed from transverse crevasses and that P_0 are formed from ablation surfaces exposed above the equilibrium line. P_1 debris layers are limited to fine dirt and occasionally small stones, while P_0 debris layers can be several centimeters thick and contain cobbles up to about 5 cm. This is consistent with the kind of debris that could be expected to accumulate on the steep walls of a crevasse (for P_1) as opposed to a more or less level surface (for P_0). It should be noted that large amounts of debris accumulate on Variegated Glacier from rockfall and debris slides from the valley walls, so the accumulation of thick debris horizons on surfaces briefly exposed in the accumulation zone is quite possible.

A further reason for supposing that P_1 originates as transverse crevasses in some upglacier location is the dip orientations observed. These are not vertical, and hence cannot have been crevasses in their present orientation, but do have a dip consistent with a small amount of rotation by vertical shear during the passage from their original position to their final position at the terminus. A logical source for the transverse crevasses is in the icefall at $XP = 10.0$, although other sites are possible.

If P_0 are old ablation surfaces, then the designation " P_0 " is a spurious class, and these features properly belong to S_0 . However, they stand out strikingly against S_0 in the terminus region. A closer examination of some particularly clear examples of P_0 suggests that the apparent cross-cutting relationship of P_0 and S_0 is in fact an angular unconformity in S_0 in which the surface of unconformity is debris-laden (Figure 3.10). The designation P_0 has been retained because of the possibility of fault displacement along these surfaces during surge motion.

The final consideration regarding the question of local or remote origin of **P** is the deformation of **P** observed in many locations: both P_1 and P_0 exhibit the same folding seen

in S_0 , indicating that the P features have been in place at least as far back as some of the strain events that produced the folding.

Evidence of displacement on P_1 is plentiful. Many cross-cutting markers are displaced across P_1 features, although in no case could a magnitude and net direction of displacement be determined. Displacements of individual markers along traces of P were typically 10 cm or less, with some rarer displacements up to 50 cm. As has been mentioned, no large fault displacements of any kind were observed during the surge; however, displacements of several centimeters could easily have occurred without being noticed. If the displacements on P_1 occurred in association with the surge motion in the terminus region, only reverse faulting (hanging wall moving up) would have been consistent with the existing stresses. However, both reverse and normal displacements appeared in markers along traces (sometimes both on the same trace, indicating a component of slip normal to the trace surface). Furthermore, displacements of either sense can occur during formation and closure of the crevasses that may be the source of P_1 .

No cross-cutting relation could be found that indicated positively that motion on a P surface occurred in its present position (for example, displacement of S_1 or S_2 by P). At one site, P_1 appears to have undergone a small (5 cm) displacement following the folding that affects both P and S_0 (Figure 3.11). Displacements on P_0 are harder to establish since potential markers (mainly S_0) are nearly parallel to the potential slip planes. Our conclusion is that displacement has definitely occurred on P_1 and possibly on P_0 , and that it has possibly occurred as fault displacement on the surfaces after their closure. The displacement may have occurred when the P features were at or near their present positions, but no displacements of a substantial magnitude occurred. In another part of the terminus region, thrust faults developed at the leading edge in very thin ice and underwent displacements of a few meters. These are important parts of the deformation in that part of the glacier, and may be the ultimate development of the narrowing, steepening surge front as it enters thinner ice. In the part of the terminus region considered here, however, the observed spacing of faults and the probable displacements on them does not account for a significant amount of deformation. The magnitude of longitudinal shortening due to fault displacement may be estimated by taking the typical fault spacing to be 100 m, the typical fault displacement (in dip slip) to be 0.1 m, and the typical dip angle to be 75° . This results in a longitudinal shortening of $\approx 2 \times 10^{-4}\%$, several orders of magnitude smaller than the observed

compressive strain. The possible component of motion during the surge by faulting is therefore small enough that it may be neglected in models of flow. This is an important consideration in the finite element calculations presented in Chapter 4.

Evolution of structures

In the preceding sections we have presented the categories of structure defined in the terminus region, described their occurrence and interrelation on the glacier, and presented what we believe to be the most probable origin of these structures. We now proceed to describe what we believe to be their temporal evolution. This is done in light of the facts presented in this chapter and the preceding one, but including knowledge of information not yet presented. A final, fully comprehensive discussion can be undertaken only when these latter topics have been dealt with. It is useful, however, to summarize matters at this point with a picture of the evolution of the structures based primarily on the information already in hand.

Immediately before the passage of the surge into the terminus region, the condition of the ice must be compatible with what is known about conditions in 1982, and must be reasonably derivable from post-surge conditions as seen in 1986. The glacier surface immediately before the surge was deeply buried (on the order of 100 m) in the glacier at the end of the previous surge. Ablation in the intervening years has exposed the presurge surface, and diffusive processes may have been at work to alter some structural characteristics such as bubble distributions. The large-scale structures - S_0 and P - were certainly present, probably in a state indistinguishable in essential details from their state immediately after a surge. S_b probably persists in a thin layer at the bed everywhere in the terminus region. S_2 cracks may be absent, having never developed at the depth which eventually becomes the presurge surface. Alternatively, S_2 may have developed but is no longer present, due to a combination of diffusive and healing processes, and the fact that even if originally present, open cracks cannot survive at depth for any length of time after a surge. In support of this conclusion is the fact that only one longitudinal crack set was found, instead of a fresh set superimposed on an older set with some different orientation. The possibility that the new and old sets might have exactly the same orientation is extremely remote. A final possibility is that the old set of S_2 is reactivated in the new surge, in spite of what may be a less than optimal orientation. This possibility also seems remote, however, since so many of the S_2 features are fine hairline cracks and bubble traces which

seem too ephemeral to be the surviving product of years of diffusion and recrystallization between surges.

The possible changes in S_1 following a surge were considered in the previous section. The best conclusion that can be made for the present purpose is that the transverse foliation might be expected to persist between surges with varying degrees of recognizability.

With this initial condition in mind, we can now visualize the entrance of the surge front into the terminus region. No structural changes involving accumulated strain occur before the front, although we will see in Chapter 4 that fractures related to the buckle folds described in Chapter 2 may be forming here. As ice meets the downglacier edge of the front, it experiences a sudden onset of longitudinal compression rate, and a rapid displacement both in the downglacier and vertical directions. These events are clear in the measurements presented in Chapter 2. The times of maximum longitudinal compression rate and maximum lateral extension rate do not necessarily coincide, nor are their orientations necessarily perpendicular (Raymond et al, 1987). S_2 cracks form at the time of maximum lateral extension rate.

Longitudinal compression was observed to be much larger than lateral extension (Raymond et al, 1987), and throughout the passage of the surge front, the dominant deformation is plane strain compression with the principal compression in the longitudinal direction and the principal extension in the vertical direction. In response to the compression, buckle folds develop near the surface, warping surface layers of ice up into the folds described in Chapter 2.

The longitudinal compression amplifies irregularities in planar structures with any component of strike in the longitudinal direction: in particular, the S_0 and P structures. If individual P structures are mechanically weaker in shear across their surface than the surrounding ice, then longitudinal compressive stress may initiate faulting on the surface. From the evidence of displacement seen on P_1 , this may have happened, but nothing indicates that large displacements occurred. Fault motion, if any, was an incidental aspect of the overall picture of the deformation in this part of the surge front.

After the surge, the sequence of structural developments associated with the surge front is visible in the appropriate locations along the final position of the front. Above the front, S_2 cracks have developed into crevasses which enlarge and coalesce into chasms with

distance upglacier. S_0 and P are distributed throughout the terminus region according to their displacements from initial positions before the surge.

3.5 Crystallographic Fabrics in the Terminus Region

The previous sections of this chapter have addressed the spatial inhomogeneity of ice in the terminus region. Here we will consider the anisotropy of the ice on a small scale. During the 1985 and 1986 structural surveys, samples from a series of sites along the terminus profile were collected and analyzed for optic (c) axis orientations. The results of these analyses are presented here, with a discussion of the relationship between the c-axis fabrics and the stress and strain during the surge.

3.5.1 Method

Since no facilities existed for storage or transportation of ice, all handling and measurements were conducted immediately after collecting samples. Once thin sections were prepared, measurements had to be made quickly, for the ambient temperature was typically about 10°C and sections lasted only about 10 minutes. The rapid melting turned out to be less of a problem than anticipated because the grain sizes in the thin sections were large (typically ≈ 2 cm). This meant that the thin sections 2-3 mm thick were still usable, and could be measured quickly since only 10 grains or so were present.

At each site, a clean, level ice surface was prepared by cutting below debris and the surface weathering zone with a chain saw. The excavated site was usually a single strip about 1 m wide and 3 m long. Oriented sections were cut from the strip at 20-30 cm intervals to ensure that single crystals did not appear in more than one section. The excavated samples were cut about 5 cm thick to allow for melting during the interval before preparing thin sections.

Thin sections were prepared at a central measurement site by first cutting the section down to 1 cm thick with a "sven" type hand saw, then melting the section on a hot plate until a workable thickness was achieved. The thin section was then fixed in a plexiglass sample holder with wire grips, and placed in a conventional Rigsby universal stage. Available daylight was used to illuminate the stage. Measurements, refraction corrections, and scatter diagrams were made by the standard method described in Langway (1958).

The contoured data presented here were calculated by a computer program based on the Kamb method for statistically analyzing orientation data (Kamb, 1959). The plotted contours are increments of standard deviation (σ) away from a random distribution. Regions of the contour diagrams with population densities greater than twice the expected number for a random distribution are interpreted to be significantly overpopulated (M. Brandon, written communication).

3.5.2 Crystallographic Fabrics

The ice throughout the terminus profile was uniformly coarse-grained, with crystal diameters in thin sections typically ≈ 2 cm. Bubble content varied between low and moderate. Figure 3.12 shows the typical bubble content in what is referred to here as coarse bubbly ice. Figure 3.13 is a sketch showing the typical grain structure in thin section.

C-axis orientations, both as scatterplots and as contour diagrams, are shown in Figure 3.14 for a profile of 10 sites in the terminus region. The data are plotted in lower hemisphere equal area projections. Site AA lies at the upglacier extreme of the profile, above the map region of Figure 3.9, and about 600 m above site A. Sites A through H lie along the map region in Figure 3.9, and site GWM is located at the top of the moraine GWM.

Ice in the terminus region was stagnant and at 0°C for most of the time between the end of the surge in 1983 and the collection and analysis of fabrics in 1985 and 1986. Rigsby (1960) showed that recrystallization can occur very rapidly at 0°C , and that a well developed fabric can be completely annealed to a new random fabric in the space of a month. The fabrics in Figure 3.14 are evidently not random, and surprisingly, even ice taken from below the final position of the surge front (sites G,H, and GWM) shows evidence of a fabric despite the absence of deformation since 1965. It seems probable, however, that some dispersion of maxima has occurred since 1983 and that the fabrics shown may have been stronger immediately following the surge.

In connection with Rigsby's observations on recrystallization, it should be noted that his striking example of recrystallization of a natural fabric from glacier ice in Greenland started from very fine grained ice with about 300 grains appearing in a 3-inch diameter thin section. This would have provided many grain boundaries along which new crystals could

grow and may have caused much more rapid recrystallization than would be observed in a coarse grained specimen.

A consistent pattern appears in Figure 3.14 in the sequence of sites from AA to F. All show a broad elongated maximum, or double maximum, pointing approximately in the direction of principal compression and having only a slight dip in the upglacier or downglacier direction. The principal compression direction is designated on individual fabric plots by an arrow on the equator point parallel to the principal compression direction. At sites G and H below F, a pronounced change takes place in the orientations. Maxima become more diffuse, and more importantly, take on a nearly vertical orientation. These sites lie on the downglacier side of the S_0/S_b transition, in the region where the horizontal S_b foliation exists. The intensity of S_b is moderate at G and very strong at H. The fabric has followed the same pattern as the foliation in this region, changing its orientation 90° in parallel with the poles to the foliation. The contour diagrams at sites G and H faintly suggest multiple maximum (possibly 3-pole) orientations. A moderately strong fabric returns at site GWM, with the single c-axis maximum lying very close to the pole to the S_b foliation. Note that S_b is not flat-lying here; this is the result of the deformation associated with flow into local depressions that was described in section 3.2. The statistical validity of the c-axis maxima is evident in the contour diagrams, where the center of the maxima are seen to lie between 9 and 15 σ above a random distribution. The double maxima at sites C,D,E, and F, and the multiple maxima at G and H are somewhat less certain, for the weaker maxima at each site stand only 3σ above the area separating them from the main maxima. This is above the defined criterion of 2σ for significance, but not by the margin seen in the main maxima. An examination of the scatterplots for these sites does not always reveal convincing secondary maxima. It is questionable whether the orientation of the maxima can be specified very precisely. The maxima are broad, and if the multiple maxima are regarded as one diffuse maximum, the orientation becomes even less definite. An eigenvalue decomposition of the orientation distributions would provide principal directions of a best fit ellipsoid to the data, but this technique is inappropriate for distributions with less than orthorhombic symmetry. The best characterization of the fabrics between sites AA and F is that they are elongated, possibly double maximum patterns oriented approximately in the principal compression direction.

The relation between the orientation of the c-axis maxima and the direction of principal compression is striking when compared to the fabrics presented by Kamb (1972) for uniaxial compression and pure shear at 0°C. Kamb deformed ice at 0°C in an apparatus designed to impose plane strain, but pressure melting of the sample resulted in a strain more nearly resembling uniaxial compression. Ice taken from the base of an icefall at Blue Glacier, Washington had been deformed in a state closer to pure shear, although some extension in the intermediate strain direction is known to have occurred (C.F. Raymond, personal communication). The state of stress at the surge front is very nearly pure shear, being plane strain with the principal compression direction horizontal, principal extension direction vertical, and only small amounts of extension in the lateral direction. In his experiments and on Blue Glacier, Kamb found small circle fabrics approximately centered on the direction of principal compression (Kamb 1972, Figure 17). The small circles were incomplete, and appeared rather as two maxima lying adjacent to the principal compression direction. The strength of the maxima at sites AA through F lie intermediate between Kamb's maxima, being stronger than Kamb's experimentally produced fabric (at 4-6% per 1% area vs 3% per 1% area) and weaker than the maxima at Blue Glacier (4-6% vs 8%). It should be recalled, however, that some dispersion may have occurred between the end of the surge in 1983 and the collection of samples in 1985 and 1986.

The finite strain in Kamb's experimentally produced fabric (-0.37 logarithmic) was less than the probable total strain in the terminus region. The strain in the Blue Glacier sample was unknown, but a strain rate of about 0.3 yr^{-1} (logarithmic) was measured over 1 year. The grain size in the experimentally deformed sample was initially small (0.5-0.9 mm diameter), and grew to larger sizes, but still substantially smaller than what was observed in the terminus region. The Blue Glacier ice type was described only as coarse bubbly, but was probably similar in grain size to the ice in the terminus region.

No clear correspondence exists between the orientation of S_1 and S_2 and the fabric maxima, beyond the fact that S_2 is more nearly parallel to the flow direction than perpendicular, and *vice versa* for S_1 . This is persistent with the proposed origins for S_1 and S_2 presented in section 3.4, where it was suggested that neither feature formed in response to the total compressive strain.

The orientation and pattern of fabric maxima at sites AA through F indicate that some complex maximum or maxima developed roughly coaxially with the direction of

principal compression. The fabrics are similar to Kamb's fabrics for compression at 0°C, and give support to the notion that these fabrics are typically associated with pure shear. The fabrics in Figure 3.14 are not all as clear as Kamb's, but if one were to be chosen (e.g. site C) for comparison with Kamb's one example from a glacier, the similarity would be very satisfactory. The consistency in orientation between the principal compression direction and the mid-point of the elongated maximum at sites AA through F is variable, but is close enough to provide evidence of a connection.

Below the S_1/S_2 transition, sites G and H show what may be a multiple (possibly 3-pole) maximum oriented vertically. This fabric resembles those seen at Blue Glacier (Kamb, 1959) in coarse ice subjected to large magnitudes of simple shear, although the classic "diamond" pattern is not evident here. The resemblance includes the fact that the maxima are centered on the pole to foliation, and appears to confirm Rigsby's suggestion (communicated in Kamb, 1959) that the multiple maximum fabric is more typically composed of 3 maxima. The weakness of the fabrics at G and H is not unexpected; in fact, given the length of time this ice has been stagnant, these fabrics are surprisingly strong. At GWM, the maximum is still somewhat elongated, but more nearly resembles a single maximum than at most of the other sites. This is in ice with a strong S_2 foliation. The pairing of a single maximum fabric with a strong foliation resembles the situation described by Hudleston (1977), in which a zone of intense shear strain developed a strong single maximum fabric, flanked by double maximum fabrics in adjacent ice subjected to smaller amounts of shear. It is not clear why the ice at GWM should have a substantially stronger fabric than G and H, for GWM is located in ice well above the bed of the glacier. The differences between these sites may be due to differences in their strain histories during the 1964/65 surge, although such distinctions are difficult to separate now from annealing effects that may have occurred since that time.

In summary, c-axis fabrics developed in ice above the S_2/S_1 transition which are consistent with other fabrics developed in pure shear at 0°C. These are broad single, possibly double, maxima oriented at or near the principal compression direction, which in the terminus region is roughly horizontal and in the flow direction (and perpendicular to S_1). Below the S_2/S_1 transition, there is an abrupt change in the fabric type to nearly vertical maxima. These are either broad (or diffused) or multiple maxima and may be the product of shear in the S_2 planes.



Figure 3.1 Terminus region of Varigated Glacier on 1 September 1974.

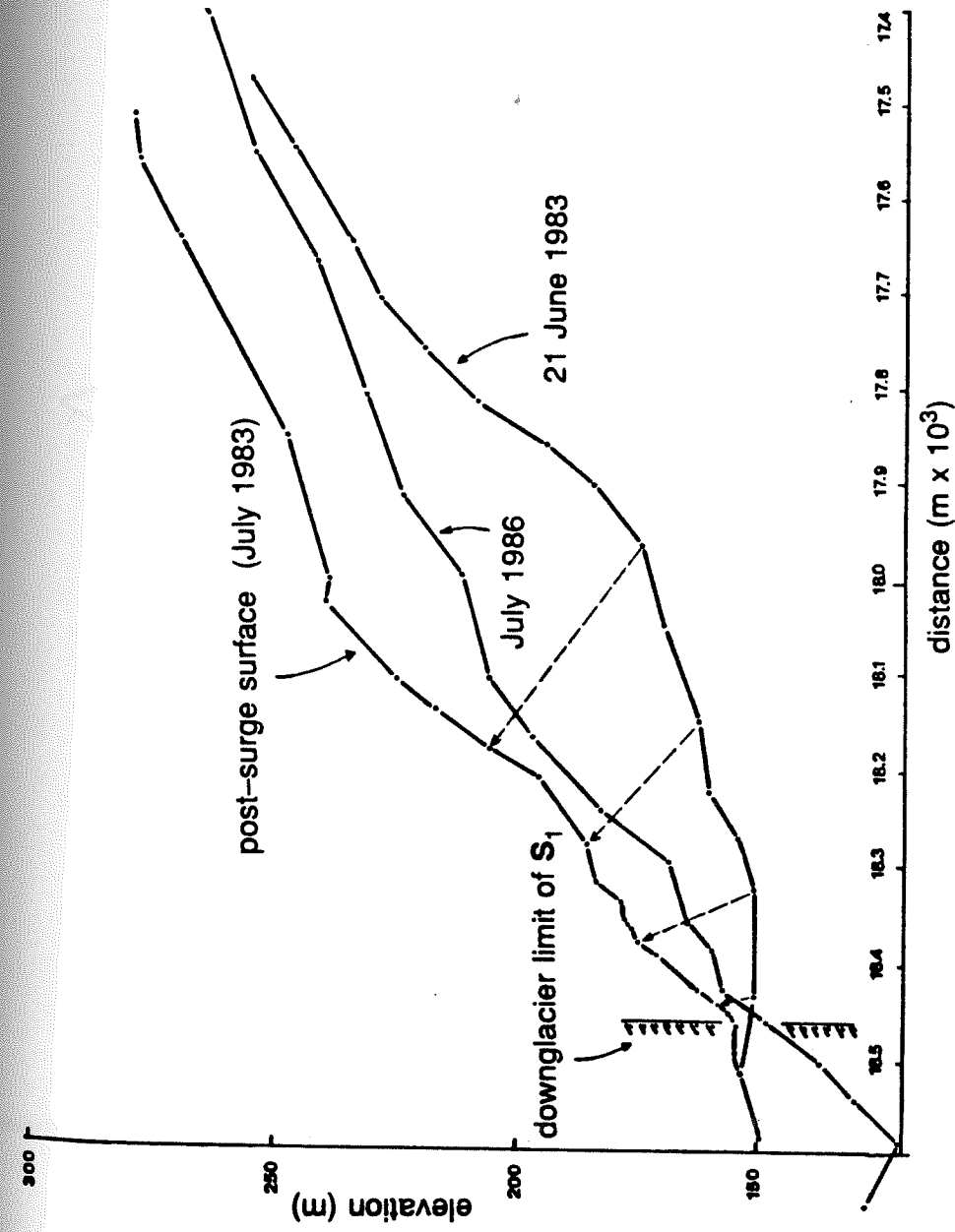


Figure 3.2. Surface elevation profiles in terminus region on 21 June 1983, following end of surge in July 1983, and in July 1986.

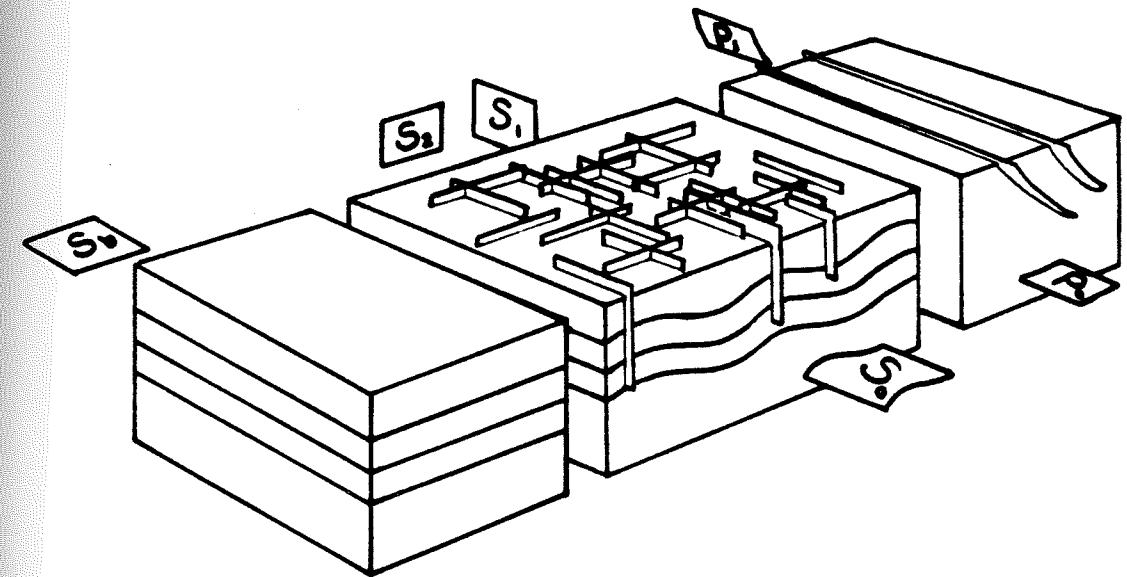


Figure 3.3. Schematic of structural elements defined in terminus region.



Figure 3.4. a) Primary layering S_0 . b) S_0 showing steeply dipping area.

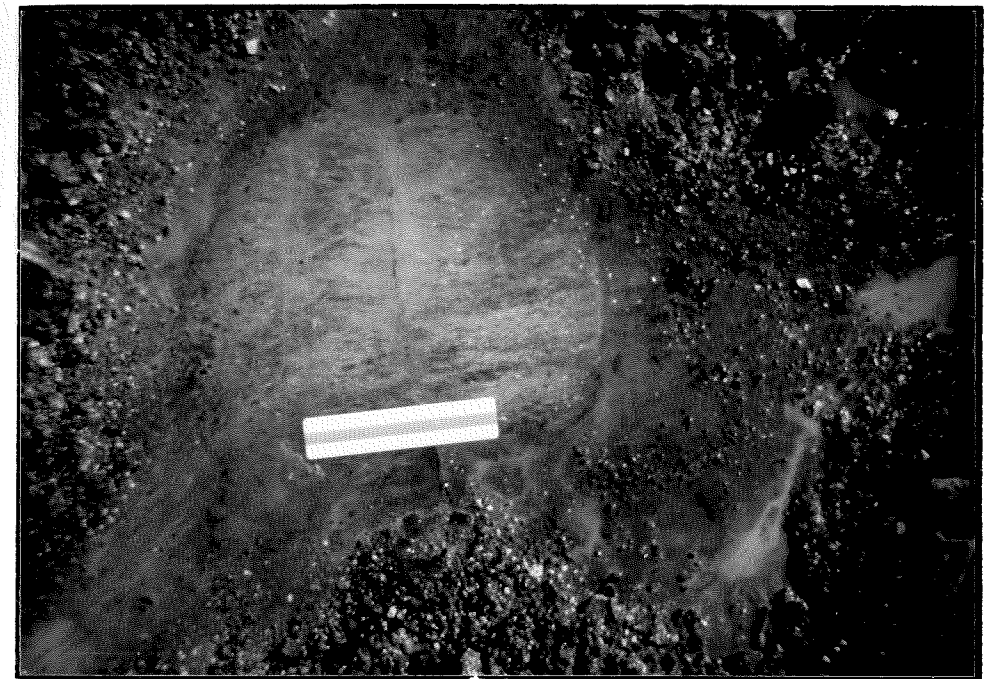


Figure 3.5. Typical exposure showing S_1 (parallel to ruler) and S_2 (perpendicular to ruler). Ruler is 15 cm long.



Figure 3.6. Crevasses with S_2 orientation.



Ph 28-3

Figure 3.7. Subhorizontal foliation S, exposed in stream cut at downglacier end of terminus region.



Figure 3.8. Cluster of typical P_1 structures.



Figure 3.10. Cross-cutting P_1 , P_0 , and S_2 . P_1 steeply dipping, rises left to right; P_0 gently dipping, rises left to right; S_2 steeply dipping, rises right to left. P_0 can be seen cutting S_2 near the upper right corner of the picture.



h25-1 Site 25-1 Square DE

Figure 3.11. Displacement in fold in P_1 .



Figure 3.12. Thick section of coarse bubbly ice.

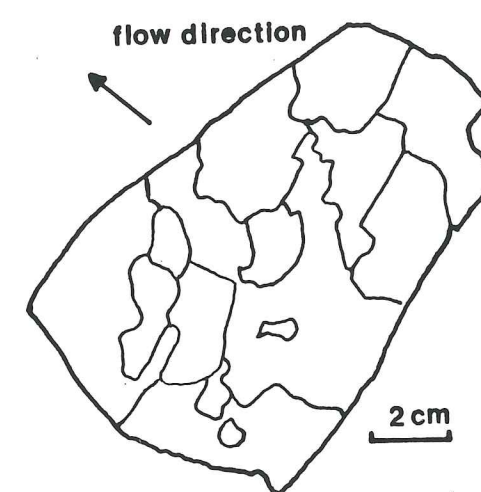
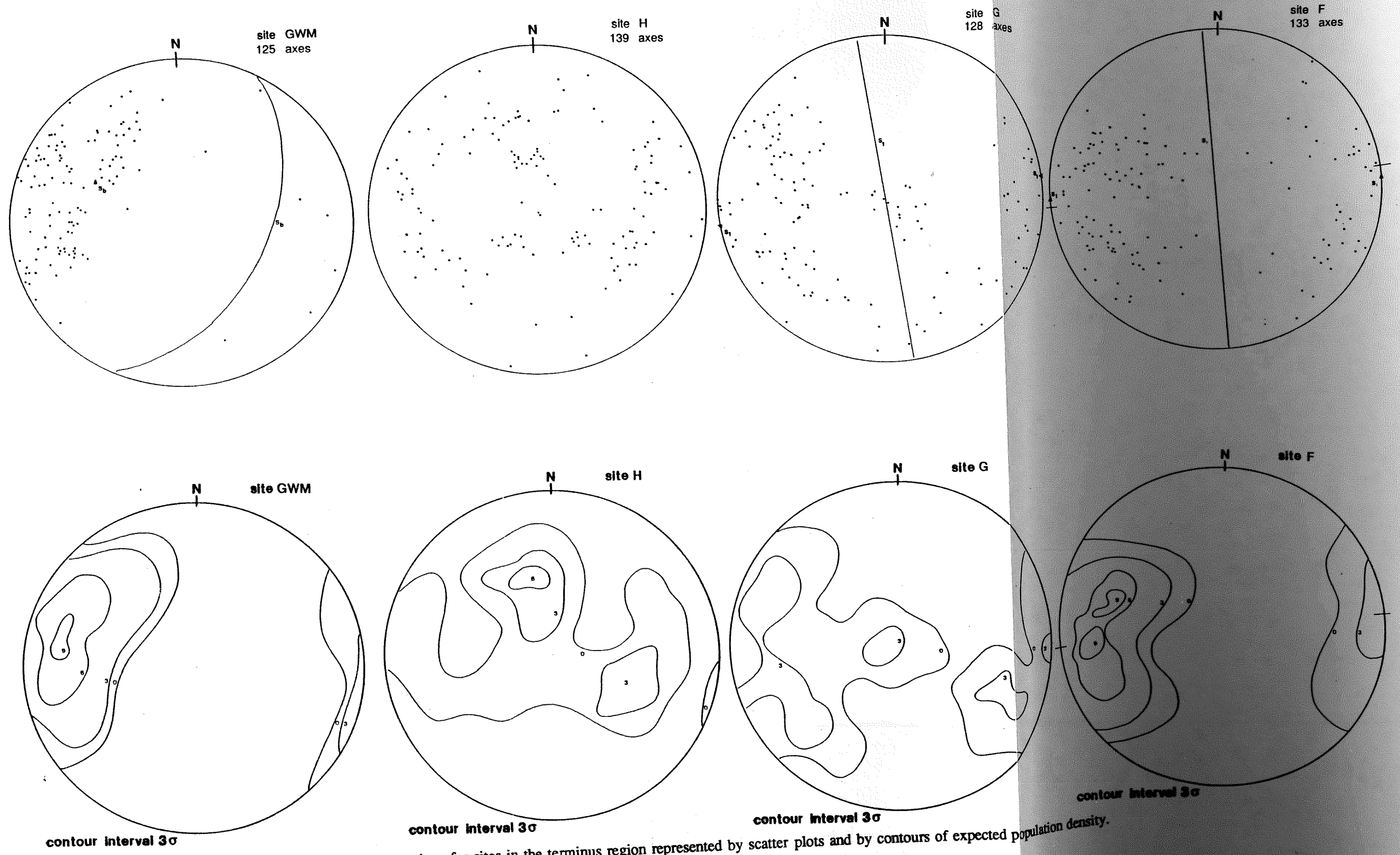


Figure 3.13 Sketch of thin section at site C.



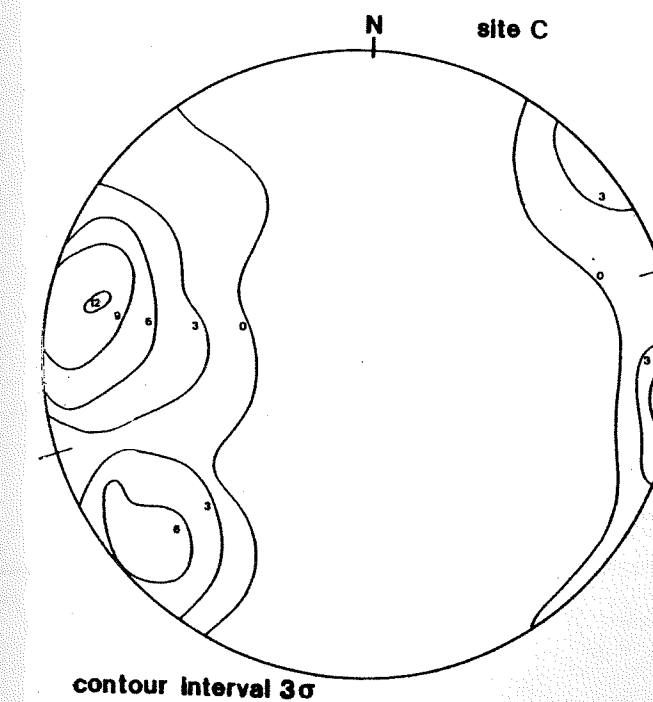
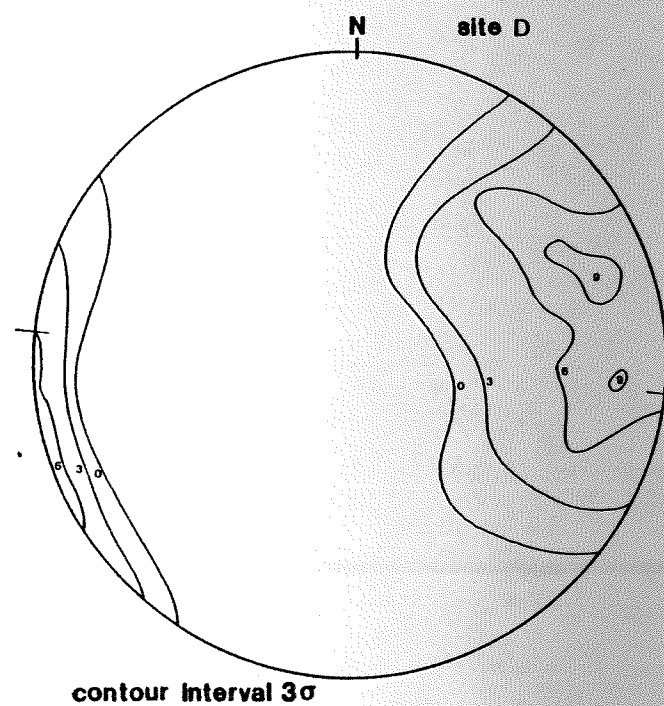
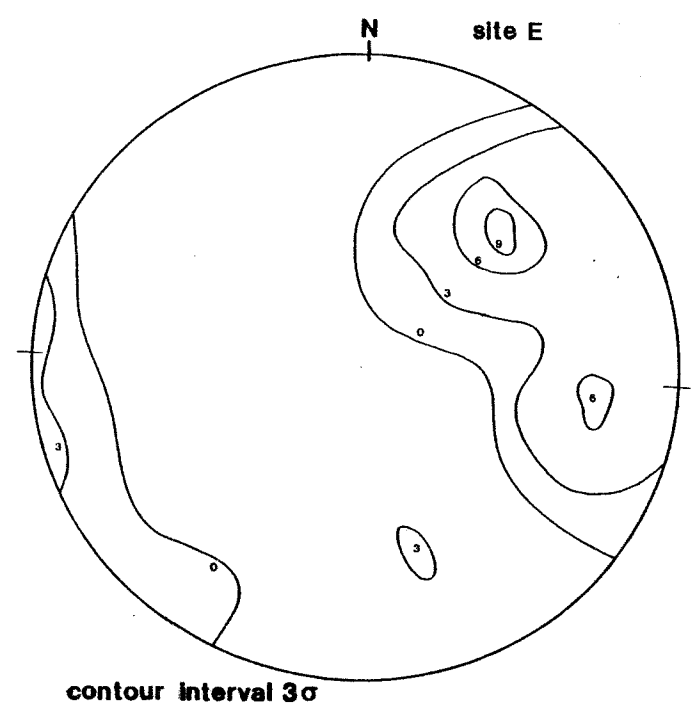
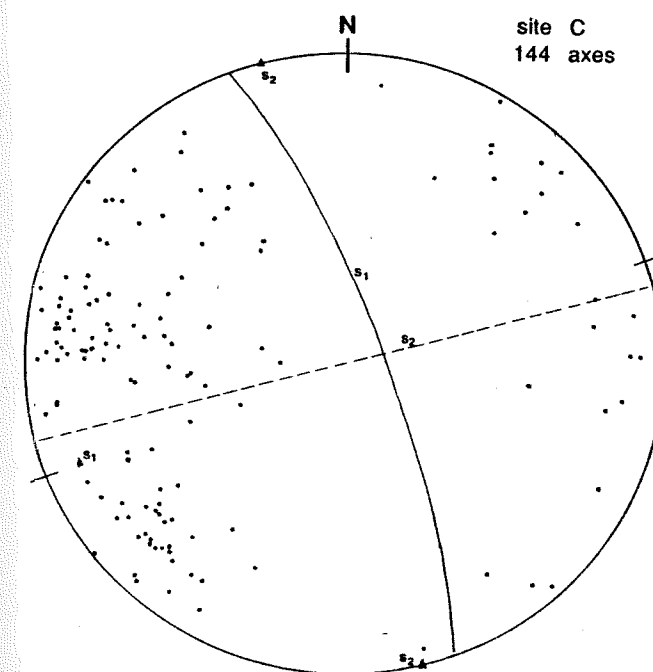
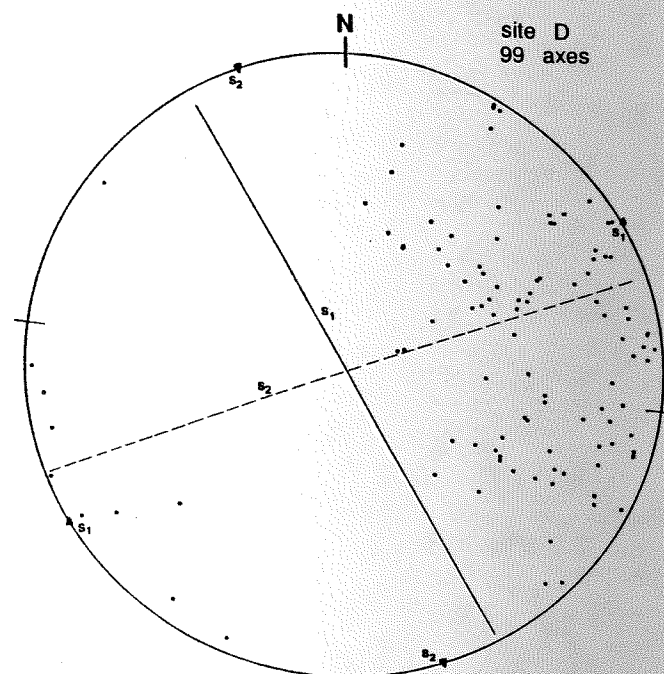
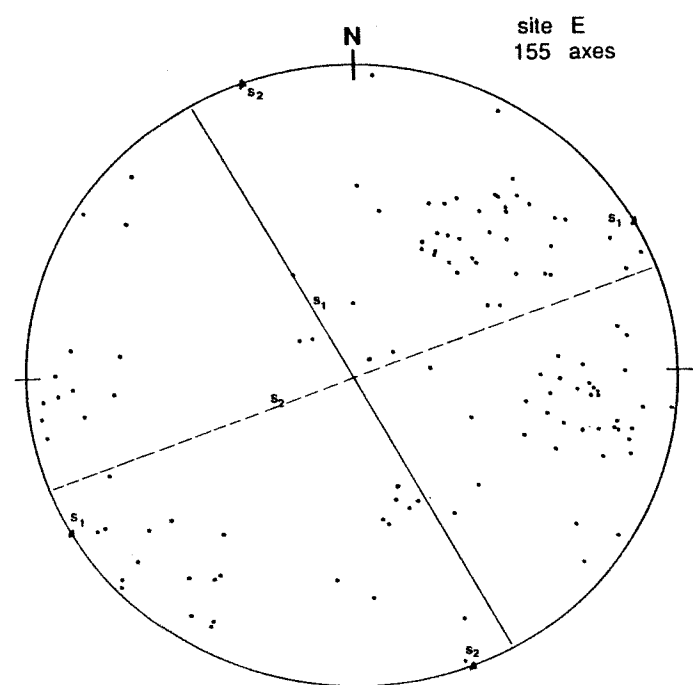


Figure 3.14 (continued)

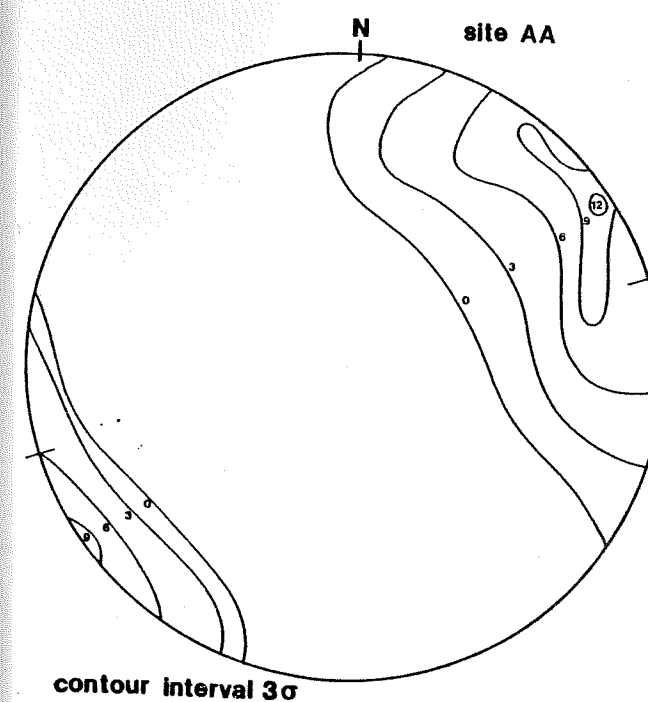
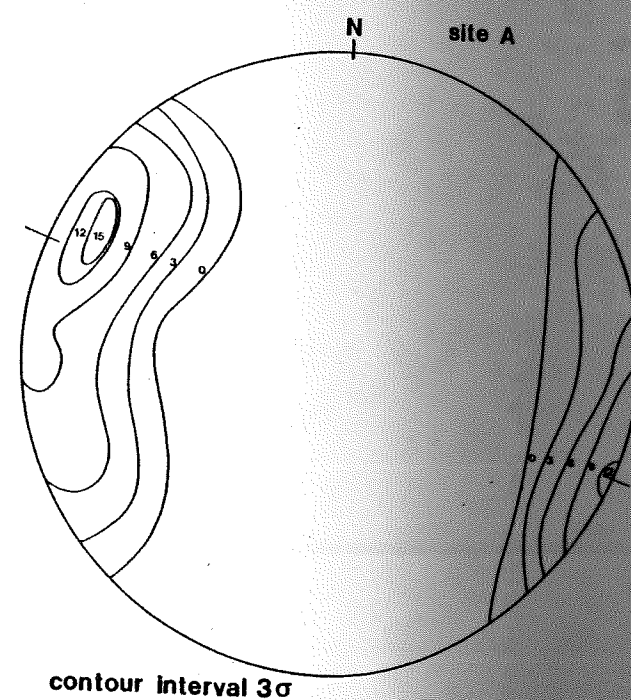
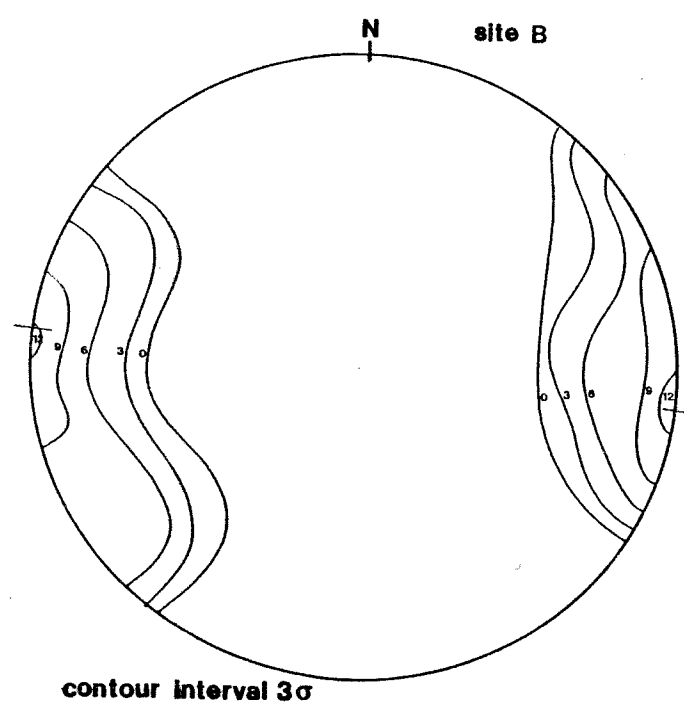
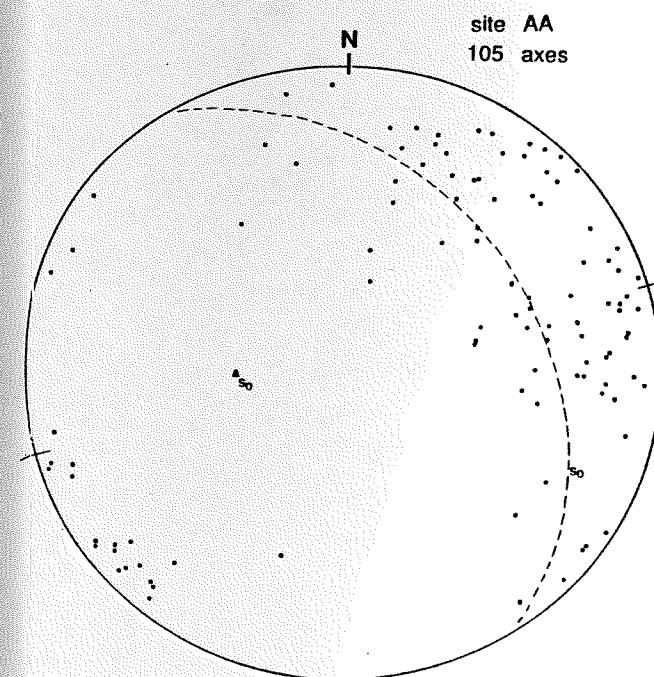
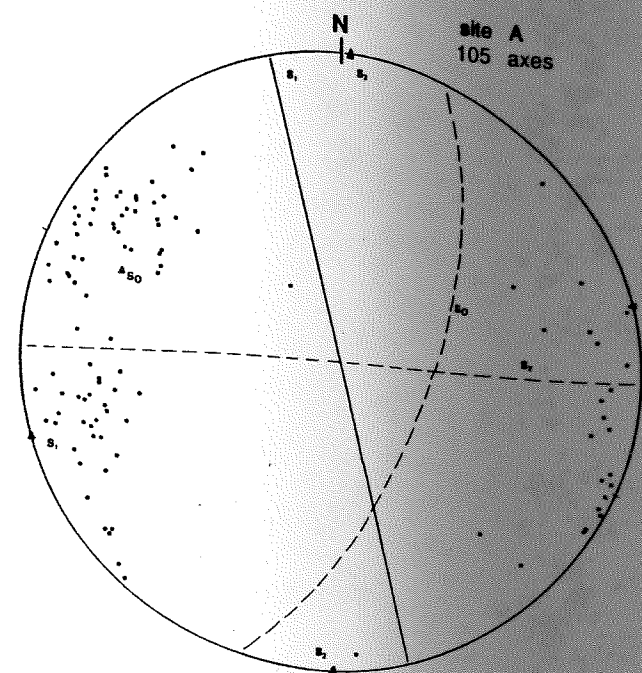
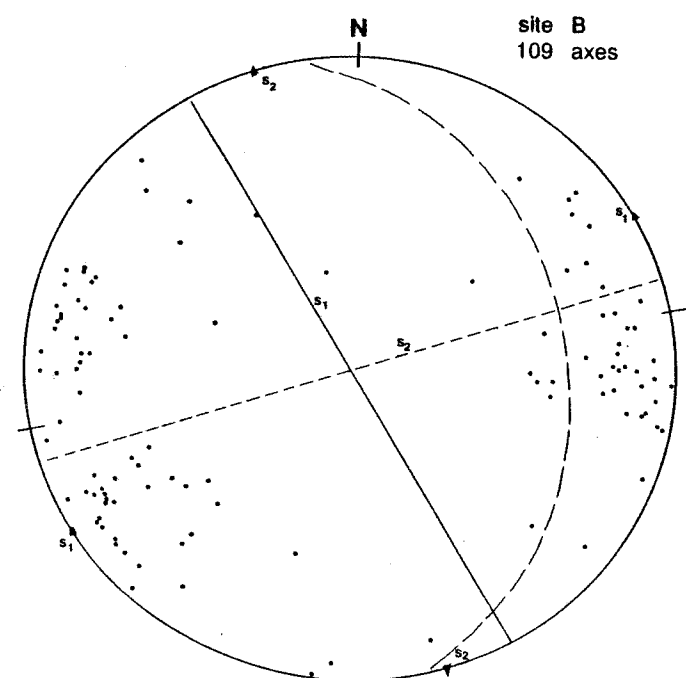


Figure 3.14 (continued)

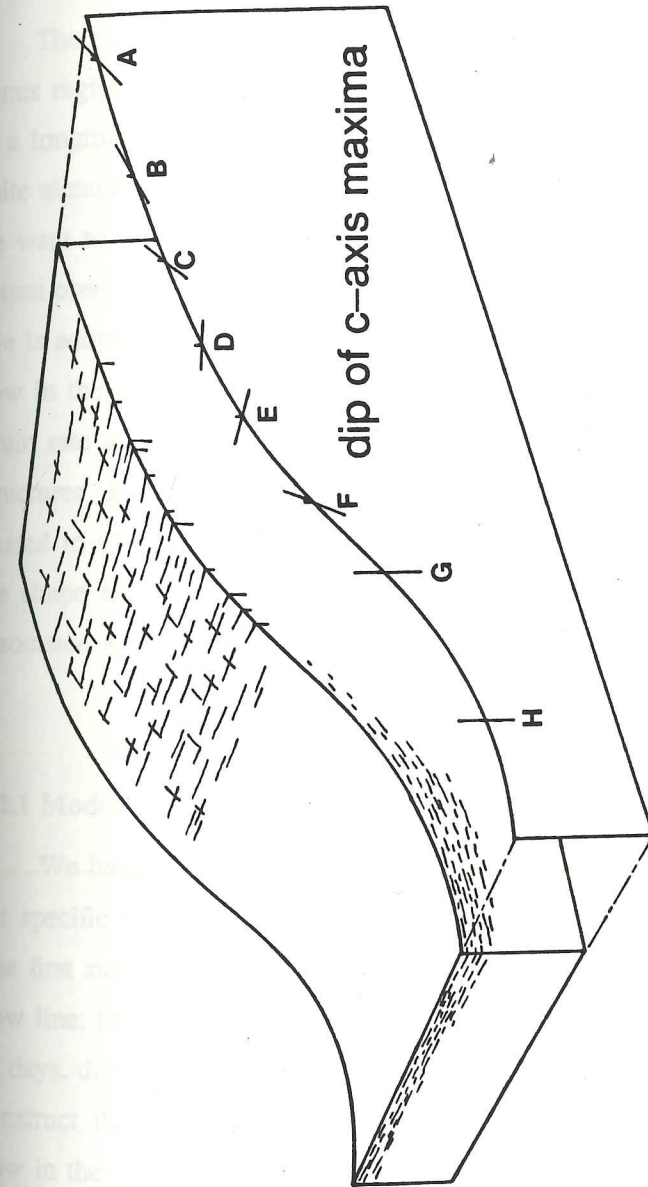


Figure 3.15. Schematic of relation between orientation of c-axis maxima and macroscopic structures in the terminus region.

CHAPTER 4

MODELING OF FLOW IN THE PROPAGATING SURGE FRONT

4.1 Introduction

The purpose of this chapter is to present the results of modeling of flow in the terminus region of Variegated Glacier during the passage of the surge front. Models of flow in a longitudinal section have been made using simple analytic theory and also by using finite element calculations. The objectives of the modeling fall into three categories. First, we want to know the velocity distribution at the bed that will produce the velocity distribution observed at the surface for the given geometry and boundary conditions. This objective is addressed here. Second, we want to know what basic kinematic elements define the flow in the front. This is addressed in Chapter 5. Third, we need accurate calculations of strain rate and finite strain to use in connection with studies of c-axis fabrics and tectonic structures developed in the terminus region during the surge. This objective has been treated in Chapter 2. The modeling provides a better understanding of factors controlling the shape and speed of the advance of the surge into the stagnant terminus, and stresses associated with the motion.

4.2 Model Design

4.2.1 Modeling Strategy

We have developed a modeling strategy that leads from the calculations of flow made for specific geometries to the generalizations about propagation which are our final goal. The first step in this strategy is to calculate in a reliable way the velocity at depth along a flow line, based on the observed geometry and surface velocity for a representative sample of days, during the passage of the surge through the terminus region. The second step is to construct the simplest possible model which can reproduce the essential features of the flow in the finite element calculations. As will be seen, this simple model is based on continuity alone, and dynamics are absent. The third step is to construct an hybrid of the preceding two models. Here we attempt to reproduce phenomena which can be explained in terms of the simple model, but we perform the calculations by the finite element method so that dynamics are included. The third model behaves in a way which is explicable in the simple terms of the second model, but has the realistic structure of the first. Its results can

be compared directly to the results based on observations during the surge.

4.2.2 Finite Element Program

Raymond (1978) describes a finite element method used to calculate flow in plane strain for an incompressible non-linear viscous medium. That method is the one used here, with the addition of certain facilities to make the calculations more accurate over a wider range of strain rates, to resolve pressure instabilities, and to more accurately calculate stresses.

Briefly, the method is applied to a longitudinal flow plane subdivided into quadrilateral 4-node elements, each of which is further subdivided into 4 subtriangles with a common vertex and implicit node at the element center. Within each subtriangle, the velocity varies linearly and the strain rate is constant. Incompressibility is imposed as an additional constraint. Nodal velocities depend on the element viscosities, which in turn depend on the effective strain rates, so an iterative algorithm is used to calculate velocities for the current step based on strain rates from the previous step. Boundary conditions may be either imposed stress, imposed velocity, or some combination of the two. The solution yields nodal velocities, element stresses, strain rates and pressures. Nodal forces are calculated on parts of the boundary where velocity boundary conditions were applied. These are converted to boundary stresses.

4.2.3 Rheology

Ice rheology in the finite element program is governed by Glen's law, with a modification used at low stress. At low stresses (where strain rates approach zero), Glen's law dictates that ice becomes very stiff; in the limit of zero effective strain rate, the stiffness (effective viscosity) becomes infinite. Because of the high velocity gradients applied as boundary conditions at the bed, high stresses are transmitted longitudinally downglacier from the surge front to the stiff motionless ice below the front. This causes numerical difficulties which we resolved by adopting a transitional linear/non-linear law which dictates a linear viscous flow at low stresses and a Glen's law flow at high stresses. This transitional law has the form

$$\eta = \frac{\eta_0 B}{\eta_0 \dot{\epsilon}^\alpha + B}$$

where η_0 is a parameter: it is the value of effective viscosity at which the linear and non-

linear components act in equal proportion. Corresponding to the transition viscosity is the transition stress τ_0 where $\eta_0 = B(A\tau_0)^{-\alpha}$. In these calculations we have used $\tau_0 = 0.05$ MPa (0.5 bars). The exponent $\alpha = 1 - 1/n$ and $B = \frac{1}{2}A^{-1/n}$.

4.2.4 Grid Geometry

The grid geometries for the terminus region models are based on survey data during the surge (Raymond et al, 1987) for the surface profile, and seismic (Bindschadler et al, 1977) and radio echo sounding data (K.A. Echelmeyer and H.F. Engelhardt, personal communication, 1983) for the bed profile. The bed in the terminus region is very nearly a uniform slope, so a straight line was passed through the available bed elevations to produce a straight bed with a down glacier slope of 0.04. At the surface, the raw elevation data were filtered to remove small scale roughness. The upglacier and down glacier ends of the section were truncated with vertical boundaries.

Extensive experiments early in the modeling work showed that a very smooth grid geometry was needed to obtain acceptable convergence when dealing with high velocity gradients on the boundary. Similarly, the element spacing within the grid must be very smooth, with concentrations of elements placed at the areas of high velocity gradients. All the grids were composed of 210 nodes and 174 elements, with the elements arranged in 29 vertical columns each 7 elements deep.

4.2.5 Boundary Conditions

The finite element grids have been made long enough to extend well into the surging zone of the glacier at the upstream end, and well into the stagnant zone below. At the upstream end, the surface velocity was measured to be of the order of 30 m d^{-1} , of which only a small fraction could be the result of internal deformation. (No direct confirmation of this assumption is available for the terminus region, but borehole inclinometry on the upper glacier as reported in Kamb et al (1985), fig. 6, shows that for one site, 97 % of the surface displacement was the result of basal sliding.) Therefore the velocity at the bed at the upstream end is very nearly the value at the surface, and the upstream end velocity boundary condition can be plug flow at the value measured at the surface. The effect of some reduction in velocity at depth was investigated but was found to be negligible. At the downstream end, the surface velocity is zero, and the velocity at depth can be assumed to be zero as well.

Only the velocity at the bed remains to be specified. No direct information is available to dictate a choice here, but this velocity boundary condition is effectively the only variable remaining in the problem. The geometry and rheology are specified, the boundary conditions at the ends of the region are fixed, and while the surface is free, acceptable calculated velocities there are constrained by data. What remains is to assign a reasonable distribution of velocity at the bed and perform the calculation. If the calculated velocity at the surface does not match the observed velocity, the chosen bed velocity is rejected and another choice is made.

4.2.6 Scheme for Matching Surface Velocity

Central to the first step in the modeling strategy described above is the assumption that a good match between calculated and observed velocities at the surface means that the basal velocity distribution is correct. This assumption needs clarification on three points.

First, we again emphasize that the rheology of the ice is regarded as known. There is, of course, uncertainty about the appropriate values of A and n to be used in Glen's flow law, and even whether this type of flow law is the best choice for a constitutive relationship. There is also a question of whether the flow in the surge front can be adequately represented by a continuum model, or whether fractures and fault displacements must be included. This has been discussed in Chapter 3, and will be discussed again later in this chapter. We have performed tests on the effect of varying A and n ; these are discussed in the next section. We will say in advance, however, that the effect on the flow pattern is small. In fact, it will be seen when simpler models of flow are discussed that continuity relations alone adequately describe the phenomena observed, and that dynamics play only a minor role.

The second point to be clarified is the question of whether the bed velocity distribution chosen is the only distribution that will reproduce the observed surface velocity. Our experience in finding appropriate velocity distributions has shown convincingly that there are no obscure choices of bed velocity which will produce a reasonable looking surface velocity. All the models represent situations where longitudinal gradients dominate vertical gradients, and there is consequently a strong coupling between basal ice and surface ice directly above. As a result, all the large features of the flow at depth are expressed at the surface.

Finally, while the large features of the basal distribution of velocity are unique, the fine details are not, and we make no claims about the small scale character of the velocity at depth. To the extent that small scale variations in bed velocity have no expression at the surface, we claim that such variations are not significant to the flow of the glacier on a large scale. Balise (1987) presents a detailed analysis of the surface expression of velocity variations occurring at the bed. Such small variations at the bed are of major significance when considering the detailed nature of basal sliding, but this is not the focus of the present work. Our results here will have application only on a larger scale, i.e., on length scales comparable to the width of the front zone.

There are two components of velocity (horizontal and vertical) to be matched at the surface, but only one component free at the bed (parallel to the bed). Velocity components perpendicular to the bed could arise from basal melting or development of cavities, but we have not allowed these, nor have we adjusted the position of the bed in an attempt to produce a better fit of velocities at the surface. Since the horizontal component of the velocity is the main component (approximately five times the vertical component), only the agreement between the horizontal component of the calculated and measured velocity at the surface is considered. No attempt is made to match the vertical component, and in fact, discrepancies develop. The discrepancies are significant, and have an interesting interpretation, as will be seen in section 4.3.2.

4.2.7 Sensitivity Tests

Rheology

Ice rheology is governed at higher stresses by Glen's law, in which we have specified $A = 0.148 \text{ bars}^{-n} \text{yr}^{-1}$ and $n = 4.2$ (Glen, 1955). These are laboratory-derived values and are higher than would be appropriate for typical glacier flow, but they are consistent with high strain rates of the surge front, and with the flow in the active regions of the glacier before the surge (Raymond and Harrison, 1987). The specific values of the parameters A and n do not critically affect the results derived below provided that they lie within a reasonable range of values defined by experiments and field results for temperate ice.

The sensitivity of solutions to changes in the chosen values for the rheological parameters A and n was evaluated by recalculating solutions for the 21 June grid using identical boundary condition and new values for A and n : n reduced by 10%, and A increased by a

factor of 1.5 (corresponding to a reduction of $B = \frac{1}{2}A^{-1/n}$ by 10%). The result was indistinguishable in the general pattern of velocity from the solution using unperturbed values. This insensitivity to specific values of the rheological parameters is not surprising, since the large velocity gradients in the boundary conditions put such large kinematic constraints on the flow that the solutions are largely dominated by continuity.

Choice of grid

The fact that a carefully smoothed grid was necessary to obtain good convergence has already been mentioned. The production of a smooth grid from raw survey data involves two steps. First, the raw surface profile is smoothed, using a rectangular ("boxcar") filter whose width is proportional to the local ice depth. A filter width of three times the ice depth provided sufficient smoothness for the finite element calculations to converge given the chosen element density, and preserved surface topography above what was felt to be an appropriate length scale. Second, the columns of elements were spaced to match the gradients along the flow plane. These could be spaced in accordance with the gradients of velocity or thickness; experiments showed that spacing according to the velocity gradient produced superior convergence.

End boundary conditions

Both velocity and stress boundary conditions were tried at the vertical upstream and downstream boundaries. Since velocities were measured on the glacier, velocity boundary conditions were much easier to make, but stress boundary conditions were tried in an effort to solve the pressure instability problems discussed below. Velocity boundary conditions were eventually chosen for the ends of the grid.

The rationale for assigning vertical distributions of velocity at the ends has been discussed. The choice of zero velocity at the stagnant downstream end is clear. At the upstream end, there is no predetermined constraint on velocity at the bed; however, it quickly became clear in the first trials that the strong vertical coupling present throughout the section required that the bed and surface velocities be very nearly the same. Velocity differences of about 5% between surface and bed were admissible, but did not produce significantly different results than plug flow. The final choice for the upstream end boundary condition for all grids was to set the horizontal velocity at all depths equal to the measured horizontal component at the surface, and to vary the vertical component linearly

4.3 Calculations Based on Front Data

4.3.1 Representative Days

In Chapter 1 the evolution of the front velocity profiles between 21 June 1983 and the end of the surge was presented. Finite element models have been made for eight representative days spread throughout the 16 day interval between 21 June and 6 July. These were all similar in essential details. Presented here are five of the eight days, one for each of the four phases of flow through the terminus region and one for the beginning of the period. These days are 21, 25, and 29 June, and 4 and 6 July. Figures 4.1 - 4.5 show for each day the velocity and stress distribution on the finite element grid. The match between measured and calculated surface velocity (two components) and distributions of basal stress (normal and shear).

4.3.2 Pattern of Velocity

The pattern of velocity at depth (part (a) of Figures 4.1 - 4.5) in all cases shows minimal shearing deformation. The absence of internal shearing deformation can be seen more graphically in Figure 4.6, which is the finite element grid for 25 June in which selected nodal coordinates have been traced from their initial position to their position after 24 hours. Internal deformation has caused a vertical extension of these lines, but has not produced substantial bed-parallel simple shear. The models for all days shared this characteristic.

The vertical velocity distribution with depth follows the pattern required by column-wise continuity, varying more or less linearly between the values at the bed and the surface. The diminution of the velocity magnitudes as the front is approached is controlled by the basal boundary condition. The coupling between bed and surface is most obvious in this part of the grid. In order to bring the surface velocities down to zero in a way dictated by the measurements, the basal velocity had to be reduced in the same way.

Sections c and d of Figures 4.1 - 4.5 show the calculated and measured surface velocities (horizontal (c) and vertical (d) components). All distributions of horizontal velocity components show good agreement between calculated and measured values. This agreement was the criterion for validity of the calculated distribution, and was generally found after only two or three trials. The distributions of vertical velocity components, however, show substantial disagreement with the measurements. In all cases, the calculated vertical

velocity at the steepest part of the front is less than the measured vertical velocity. Furthermore, a secondary peak that appears in the calculations is absent in the measurements. On the upglacier side of the vertical velocity peak, another discrepancy appears on most days, in which the calculated velocity is approximately 1 m d^{-1} higher than the measurements. This occurs in the surging zone, where longitudinal strain rates are low, and plug flow dominates. The surface velocity vectors are oriented parallel to the bed, and uncertainties in bed slope result in discrepancies in vertical velocity. The difference between the measured and calculated vertical velocities corresponds to an error in bed slope of about 1.5° , well within the limits to which the bed slope is known. Note that this error does not reduce the discrepancy at the peak in vertical velocity, but rather increases it.

Various explanations of the peak vertical velocity anomaly at the front have been considered. The inclusion of lateral straining across the flow plane would affect these results, but since the small lateral straining observed was extensile, the effect would only be an increase in the anomaly. Errors in the elevation of the bed are another possibility, but an error on the order of 20 % would be required to explain the difference. Errors of this magnitude are unlikely in the bed data. If the bed slope were wrong, the vertical velocity would be affected, as discussed above, but it would be affected most at the region of maximum horizontal velocity, rather than at the region of maximum compression where the upward anomaly appears. Finally, there is the fact that the main peak of the anomaly moves with the front. This is difficult to explain in terms of errors fixed in the geometry. More likely, some form of deformation not accounted for in the model was acting during the surge. Note, however, that this unknown deformation does not conserve volume (since the model does). We propose that the vertical velocity anomaly is caused by the development of cavities within the glacier whose growth causes a vertical swelling of the ice. A rough estimate of the amount of swelling, or excess thickening, was made by assuming that a given days vertical velocity profile represents a steady state profile which propagates downglacier at the speed of the surge front (approximately 40 m d^{-1}). The excess thickening can be calculated by integrating the excess vertical velocity ($v_{\text{measured}} - v_{\text{calculated}}$) as the profile propagates past a fixed point at 40 m d^{-1} . The result of this calculation is an excess thickening of approximately 14 m, or 11 % of the thickness. Finally, between the end of the surge in July 1983 and August 1984, the glacier surface was observed to drop by about 12 %, which is consistent with the closure of cavities following the end of the surge.

In addition to assuming that the bed elevation is adequately determined in reaching this conclusion, it has also been assumed that the profile propagates in a steady state, at a known speed, and that the horizontal component of the calculated velocity matches the observations exactly. None of these are precisely true, and deviations from these assumed conditions create uncertainty in the calculation of the excess thickness. For these reasons, the conclusions should not be taken as an accurate calculation of the quantity of void space created, but rather as evidence that volume was not conserved in the observed geometry changes, and that the magnitude of the volume change is consistent with other evidence suggesting void space as the cause.

4.3.3 Pattern of Stress

Internal deviatoric stresses are shown in part (b) of Figures 4.1 - 4.5. This shows principle deviatoric stress directions and magnitudes of the finite element grids. Directions of tensile stress are depicted by vectors with arrowheads. The patterns are characterized principally by large stresses (typically as great as 3.5 bars in the front zone), brought about by transmission of stress longitudinally through the high compression in the front. The stress directions in the front zone are very nearly parallel and perpendicular to the bed, reflecting the principle directions of strain. Below the front the stress directions rotate clockwise near the base, following the pattern associated with more typical shear deformation. In the early days of the interval (represented here by 21, 25, and 29 June), a large zone of stagnant ice extends to the downstream end of the grid; in this zone stresses are somewhat irregular in magnitude and orientation. This is a numerical artifact of incomplete convergence which has resisted removal. The large range of stresses in the grid result in a large range of residuals between iterations; the magnitudes of the residuals in the stagnant zone are very small when compared to the residuals in the front zone which control the numerical convergence. Consequently, the residuals in the front zone can be reduced to a level which achieves acceptable convergence while the residuals in the stagnant zone remain variable. The grids for 4 and 6 July do not include a stagnant zone and do not have this problem. On all grids, however, there are end effects associated with the boundary conditions at the vertical ends of the grid. These appear as anomalous rotations of the principle stresses at the ends of the grid (especially noticeable on 21 and 29 June). These anomalies are the strongest effect that the *ad hoc* choice of end boundary conditions has on the solutions; they do not, however, extend into the front zone where accuracy is most

needed.

Figure 4.7 shows the distribution of basal normal (σ_b) and shear (τ_b) stress on 22 June for two states: the normal surging state as presented so far, and a "stalled" state in which the calculation is performed with the same geometry, but with no slip at the bed. This distribution is expected if the surge were to terminate suddenly on this date as it did on 5 July. A comparison of the two states shows the stress redistribution associated with the surge motion. The shear stress has been smoothed in the driven case to remove oscillatory errors connected with the pressure instability.

Whether the surge zone is in rapid motion or not, there is a substantial jump in τ_b across the front from near zero values downglacier to 0.16-0.18 MPa (1.6-1.8 bars) or more upglacier. Above the front, τ_b is consistent with the stress level where surge motion initiated (Evolution of Variegated Glacier, Alaska, U.S.A., Prior to its Surge, C.F. Raymond and W.D. Harrison, manuscript submitted).

During the surge motion the distribution of τ_b through the front shows a low beneath the upglacier part of the front and a high beneath the downglacier part. This pattern is explained by the strong compression in the central part of the front and the resulting stress redistribution. The strong compression is absent in the "stalled" case, and the distribution of τ_b more closely fits what would be expected from standard considerations using depth and surface slope.

The basal velocity distribution found for the surge motion decreases monotonically through the front (Figure 4.7a). Comparison with τ_b implies that beneath the upper part of the front there is rapid sliding at a relatively low τ_b , but beneath the lower part of the front the opposite relationship exists. Consequently, there is a rapid downglacier transition from a zone of easy "lubricated" to one of difficult "locked" sliding.

The compressive normal stress (σ_b) on the bed shows a simple pattern. During the surge motion the strong longitudinal stress gradients and the corresponding longitudinal gradient in τ_b described above should affect σ_b . Such an effect is apparent by comparison to the stalled case, but proportionally, the differences are not large. The small differences can be explained in terms of the vertical force balance equation in the form

$$\partial\sigma_y/\partial y = -\rho_i g + \partial\tau_{xy}/\partial x \quad (3)$$

which shows that σ_b (approximately $-\sigma_{yy}$ evaluated at the bed) is increased above the weight of the overlying ice where $\partial\tau_{xy}/\partial x$ is positive. For example, consider the area near $XP = 17.9$ km with depth of about 60 m (Figure 2.3a). During surge motion $\partial\tau_{xy}/\partial x \approx +3 \times 10^{-4}$ MPa m^{-1} (Figure 4.7d), which integrated over depth predicts σ_b to be 2×10^{-2} MPa (0.2 bar) larger than overburden. For the stalled case, $\partial\tau_{xy}/\partial x$ is much smaller, and σ_b is very close to the overburden stress of 0.55 MPa (5.5 bars).

4.4¹ Fractures

While the finite element method used here cannot treat fractures, we can use the information found about stresses to identify regions of tensile stress, and thereby in a general way where and in what orientation tensile fractures might develop. This has been done to discover possible fracture sites resulting from two sources. First, true stresses are calculated from the deviatoric stresses and the smoothed pressure fields. These produce some regions of tensile stress on certain days, which can be interpreted in a way consistent with fractures which must be involved with the development of the buckle folds described in Chapter 1. Second, the same stresses are reconsidered with the additional effect of pressurized water within the glacier (hydrofracture).

Possible fracture orientations (perpendicular to the direction of tensile stress) are plotted for 21 June (Figure 4.8), 25 June (Figure 4.9), and 29 June (Figure 4.10), while hydrofractures for 21 June are shown in Figure 4.11.

Tensile stresses form where deviatoric tensile stresses become greater in magnitude than the pressure. For this reason, potential cracks do not appear at depth (where overburden stresses increase the pressure), nor do they occur in the front zone where pressures are anomalously high due to the longitudinal compression. Near the surface just downglacier from the leading edge of the surge front, however, pressures are slightly positive (compression being negative) due to the upward traction exerted on the upglacier end of this region by the rapidly rising ice in the surge front. The vertical component of deviatoric stress is positive (tensile), with the consequence that non-deviatoric vertical tensile stresses develop, oriented vertically and consistent with fractures occurring parallel to the surface at near-surface depths. The region where these tensile stresses develop corresponds to the part of the glacier where audible microcracking was observed (as discussed in Chapter 1). If surface-parallel tensile cracks were the source of the microcracking, an unresolved question

would be answered; namely, that the microcracking occurred below the surge front, indicating some state of high stress despite the fact that no substantial longitudinal strain or velocity was being recorded at the time.

The element size used in the finite element grids is not small enough relative to the probable scale length of the vertical variation of stresses to insure an adequate representation of stress variations, so the magnitude and orientations of stresses plotted in Figures 4.8 - 4.11 cannot be taken literally as predictions of exactly where and in what orientations tensile cracks might appear. The significant variations in tensile stress occur between the surface, where the stress must be zero, and the depth at which the overburden pressure exceeds the value of tensile deviatoric stresses. For the 21 June grid, this depth occurs within the second element below the surface, corresponding to a depth on the order of 10 m. On the glacier, however, surface parallel cracks were observed regularly within 10 cm of the surface. Element sizes would have to be much smaller than those used to properly evaluate the location, magnitude, and orientation of tensile stresses. Nevertheless, the calculations are evidence that tensile stresses develop near the surface in this part of the glacier, and that the stress orientations are approximately perpendicular to the surface. It is possible that the microcracking heard on the glacier was produced during the development of surface-parallel tensile cracks, and that these cracks provided the surfaces of separation on which the buckle folds formed during the subsequent compression in the surge front. It is possible, however for surface-parallel fractures such as those observed to develop in the absence of macroscopic tensile stress. Geological field studies and experiments have shown many cases where surface-parallel fractures developed in response to surface-parallel compression. In this connection, however, we note again that strain rate measurements indicated that no such compression existed at the time of the microcracking.

The hydrofractures presented in Figure 4.11 are also speculative, since they involve some assumption about the distribution of water pressure through the glacier. This is a very uncertain proposition since the relationships between conduit size, discharge, and pressure are not well known in any case, and are especially speculative in the case of surge front. Humphrey (1987) has given some theoretical examples of water pressure drops through surge fronts, however. The general shape of his calculated pressure field has been adopted here to diminish a piezometric height from an independently determined value at the top of the front zone to zero at the top of the stagnant zone. The piezometric height at points

above the front zone is determined by maintaining a chosen effective pressure ($P_{\text{overburden}} - P_{\text{water}}$) at the bed, adjusting the piezometric height according to the local ice depth.

The occurrence of hydrofractures for 21 June is shown in Figure 4.11. An effective pressure of 0.3 Mpa (3 bars) was chosen initially, determined by the effective pressure calculated for the water level data of Kamb et al (1985), Fig. 9. A 3 bar effective pressure produced no change in tensile stresses from those already seen, however. Lower values of effective pressure were then tried to determine what value of water pressure is necessary to produce hydrofracture, and where it will occur. Only effective pressures which are approximately zero have any substantial effect. This can be understood in terms of the same factors which control the simple tensile cracks. Below the surge front, water pressure is always zero (atmospheric), so hydrofracture can play no role there, while within and above the surge front, high element pressures - generally above overburden - dominate the water pressure, which is constrained to be at or below the overburden pressure (water pressures locally above overburden are possible, but are not considered here).

When the effective stress is lowered sufficiently, an interesting pattern of hydrofracture develops. An array of fractures appear in Figure 4.11 for 0 bars effective pressure which extends from near the zone of simple tensile cracks down and back to the bed. While the orientation of the cracks does not lie in a direction appropriate for thrust faulting, the path of the array of cracks does. These cracks may define a zone which under the right circumstances will develop into a thrust fault. For a surge front in thinner ice, the overburden pressures would be smaller, and if in fact water pressures are determined by conditions upglacier from the front zone (and are accordingly not constrained by local overburden), the conditions to permit thrust faulting might be achieved. In fact, thrusts were observed in a part of the terminus region outside the study area. These developed in ice substantially thinner than that presented here, they appeared at the downglacier edge of the front zone, and in several instances had pressurized water gushing from the fault.

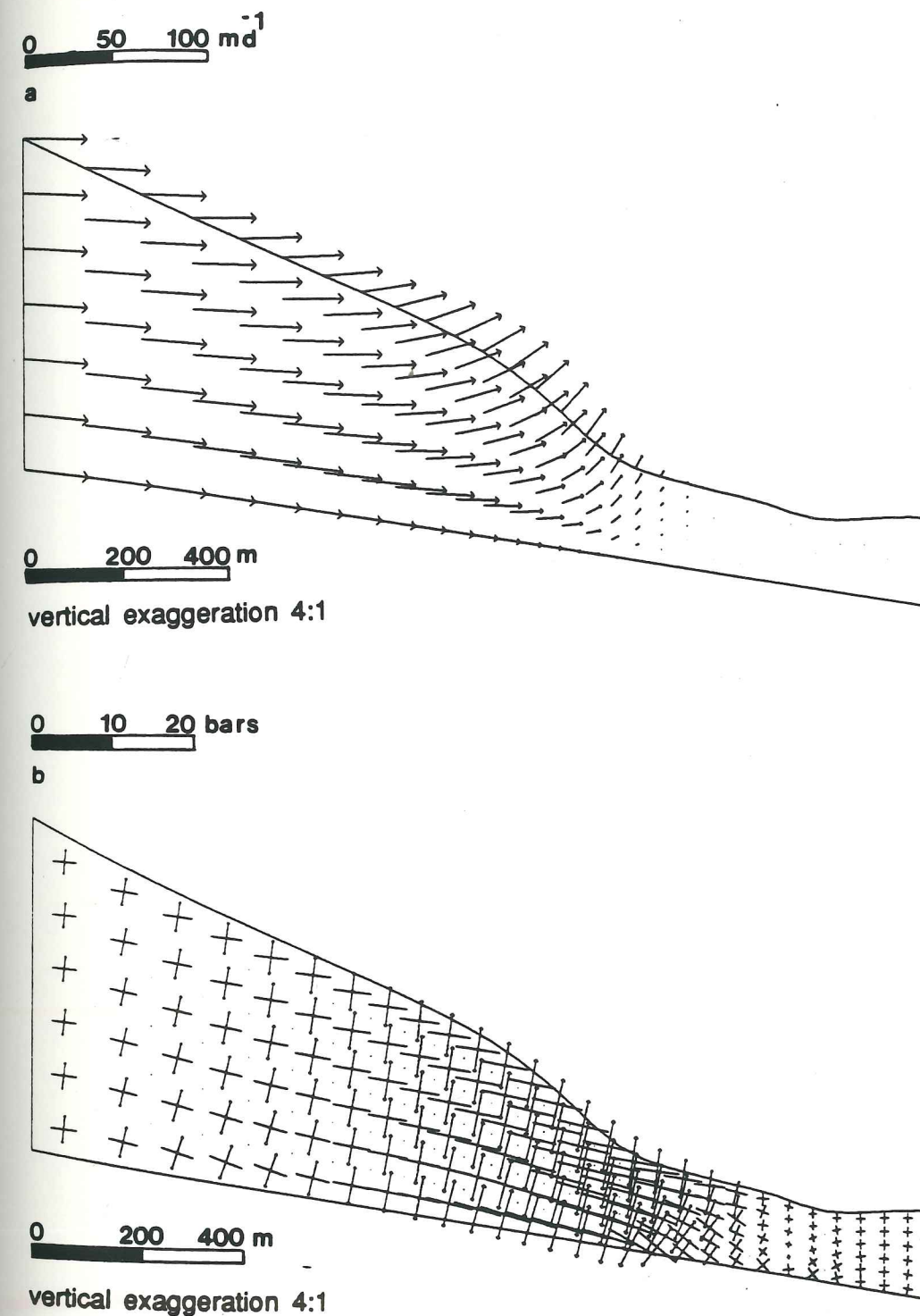


FIGURE 4.1. Finite element velocity and stress solutions for 21 June. a) Velocity vectors b) Principle deviatoric stress vectors. Vectors with arrowheads denote tensile stress; those without denote compressive stress. Vector magnitudes measured from origin of vectors to tip.

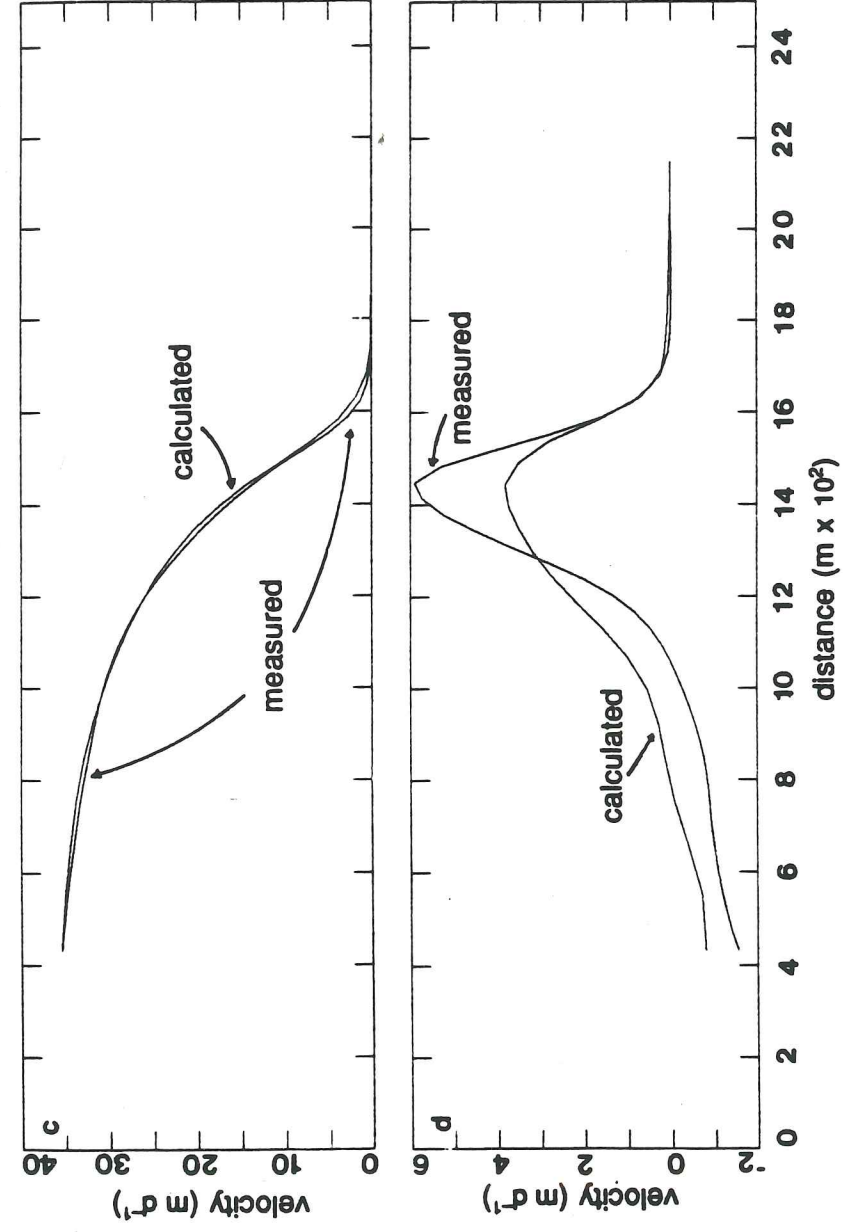


FIGURE 4.1 (continued). c) Horizontal component of velocity at surface; calculated and from measurements. d) Vertical component of velocity at surface; calculated and from measurements.

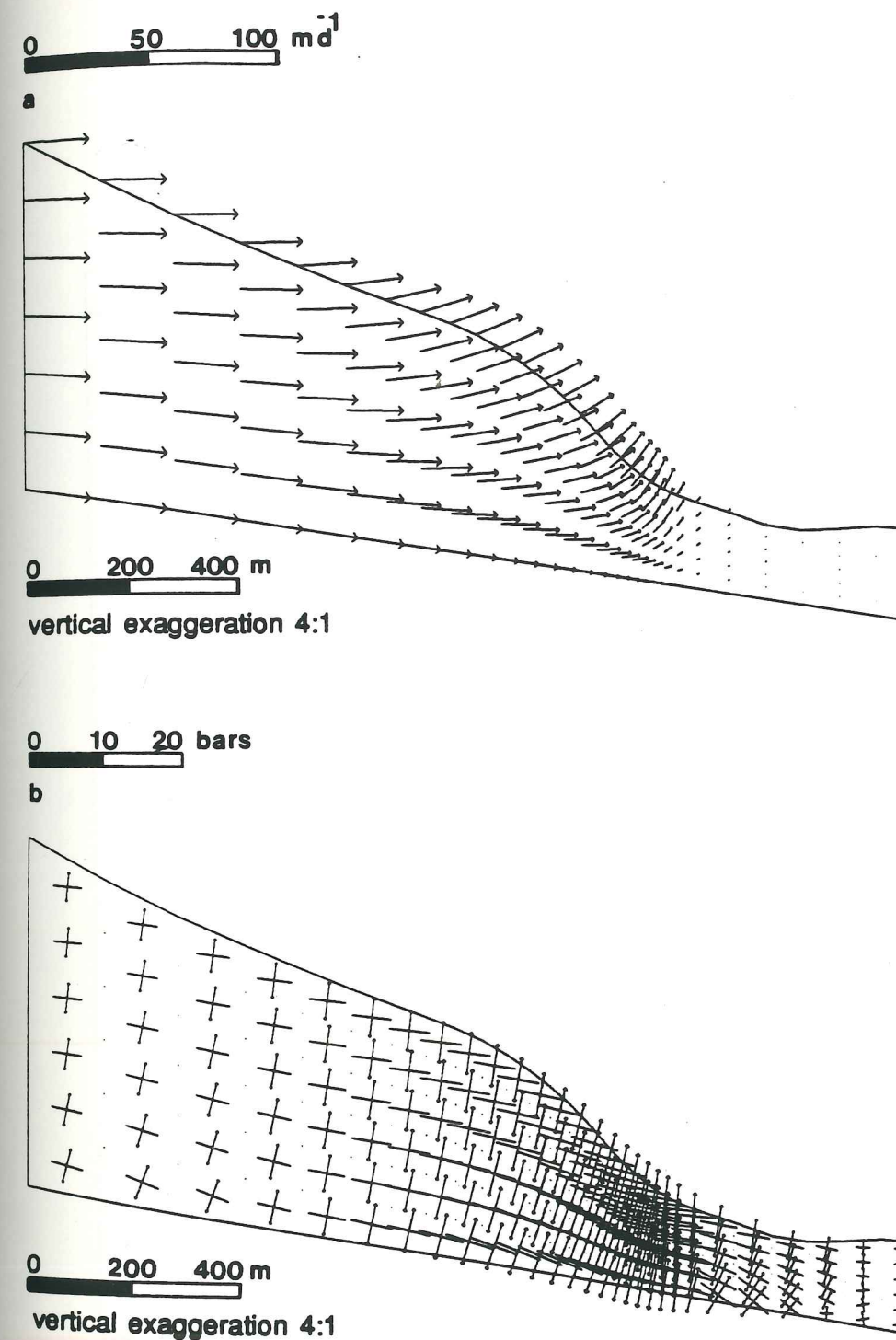


FIGURE 4.2. Finite element velocity and stress solutions for 25 June. a) Velocity vectors b) Principle deviatoric stress vectors. Vectors with arrowheads denote tensile stress; those without denote compressive stress. Vector magnitudes measured from origin of vectors to tip.

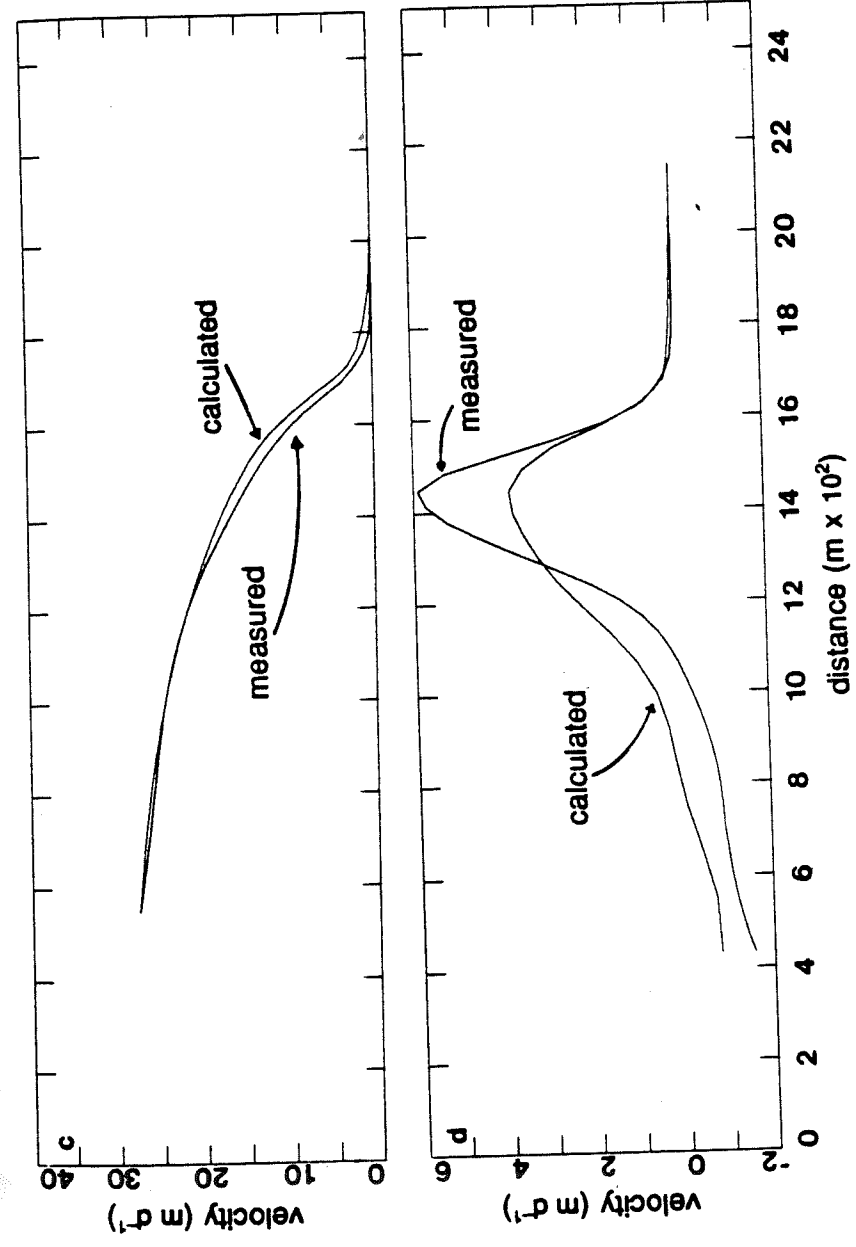


FIGURE 4.2 (continued). c) Horizontal component of velocity at surface; calculated and from measurements. d) Vertical component of velocity at surface; calculated and from measurements.

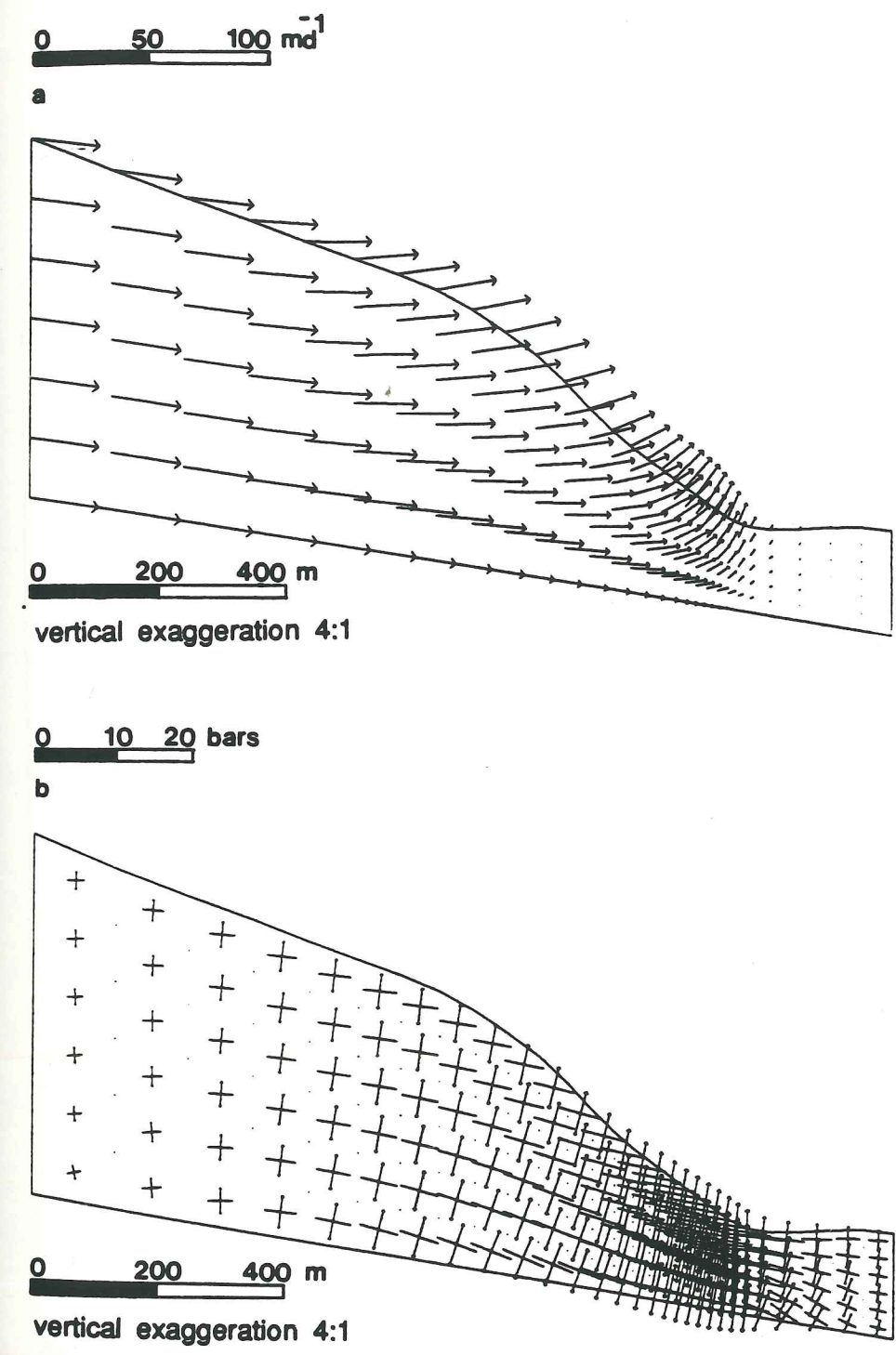


FIGURE 4.3. Finite element velocity and stress solutions for 29 June. a) Velocity vectors b) Principle deviatoric stress vectors. Vectors with arrowheads denote tensile stress; those without denote compressive stress. Vector magnitudes measured from origin of vectors to tip.

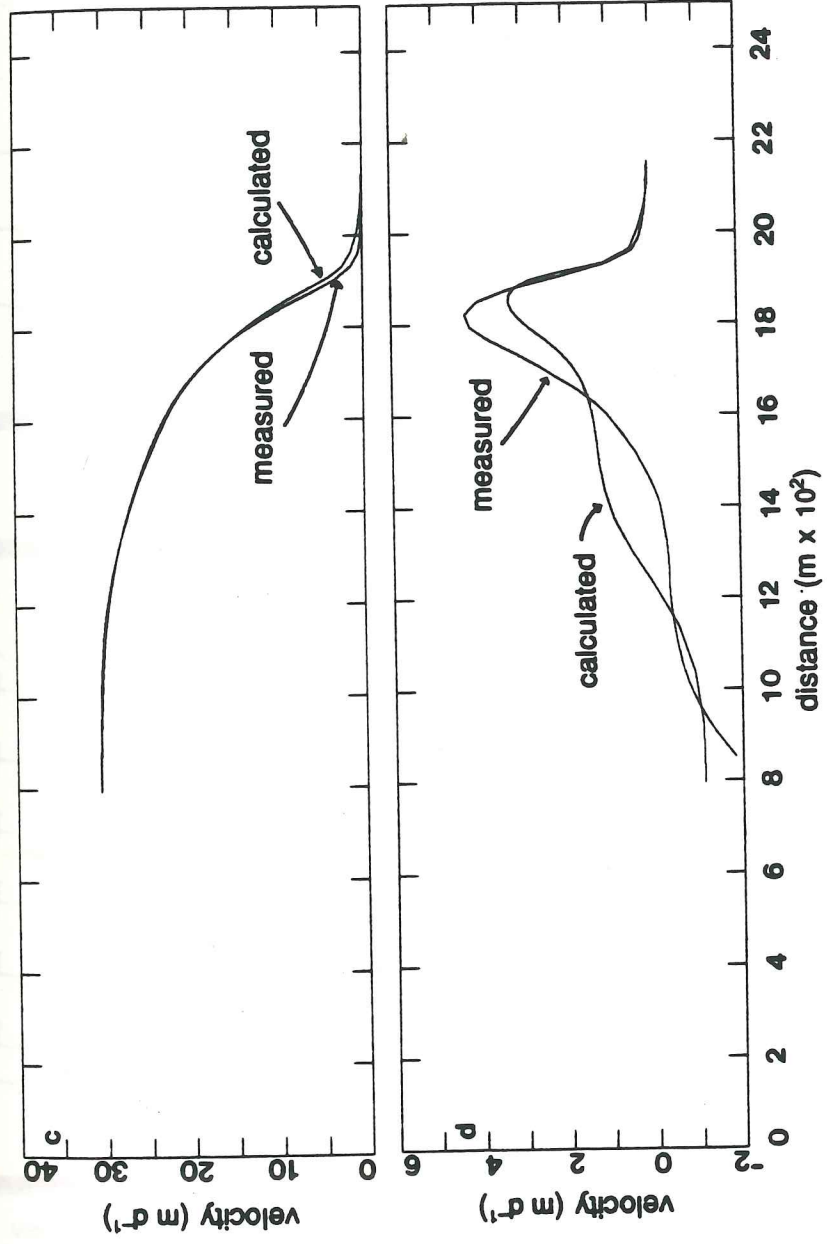


FIGURE 4.3 (continued). c) Horizontal component of velocity at surface; calculated and from measurements. d) Vertical component of velocity at surface; calculated and from measurements.

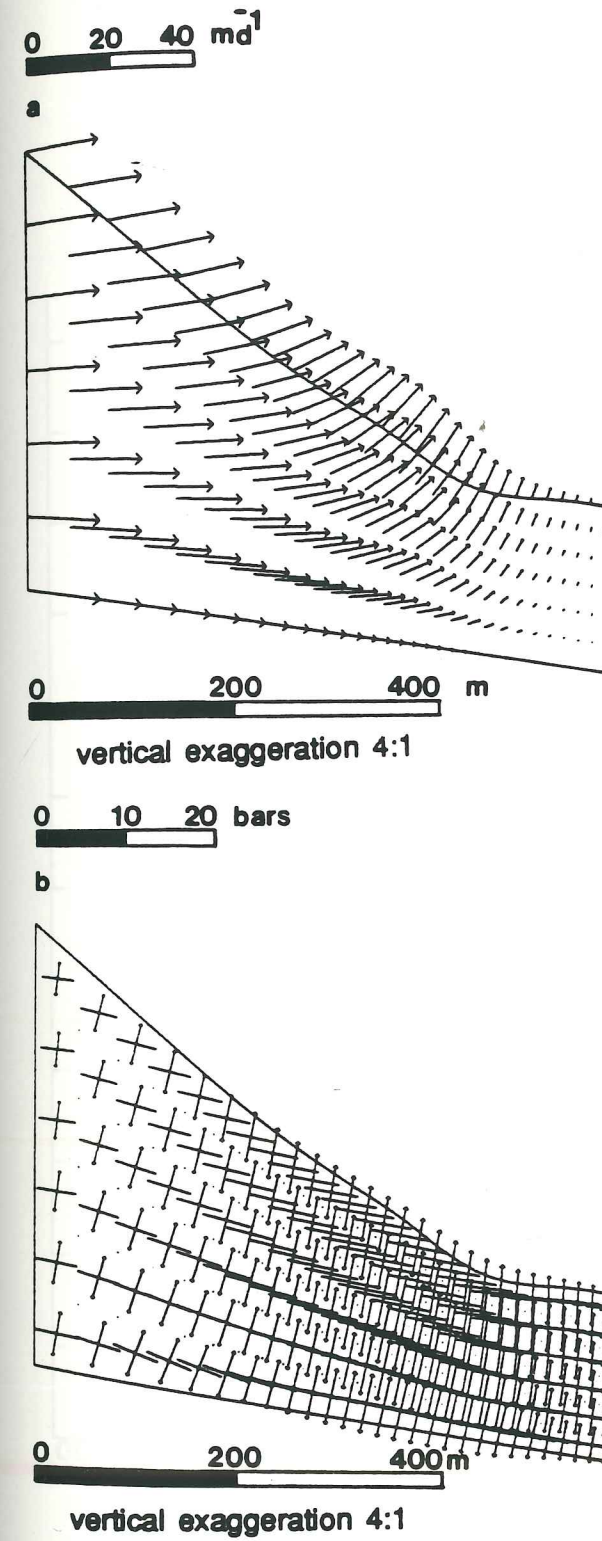


FIGURE 4.4. Finite element velocity and stress solutions for 4 July. a) Velocity vectors b) Principle deviatoric stress vectors. Vectors with arrowheads denote tensile stress; those without denote compressive stress. Vector magnitudes measured from origin of vectors to tip.

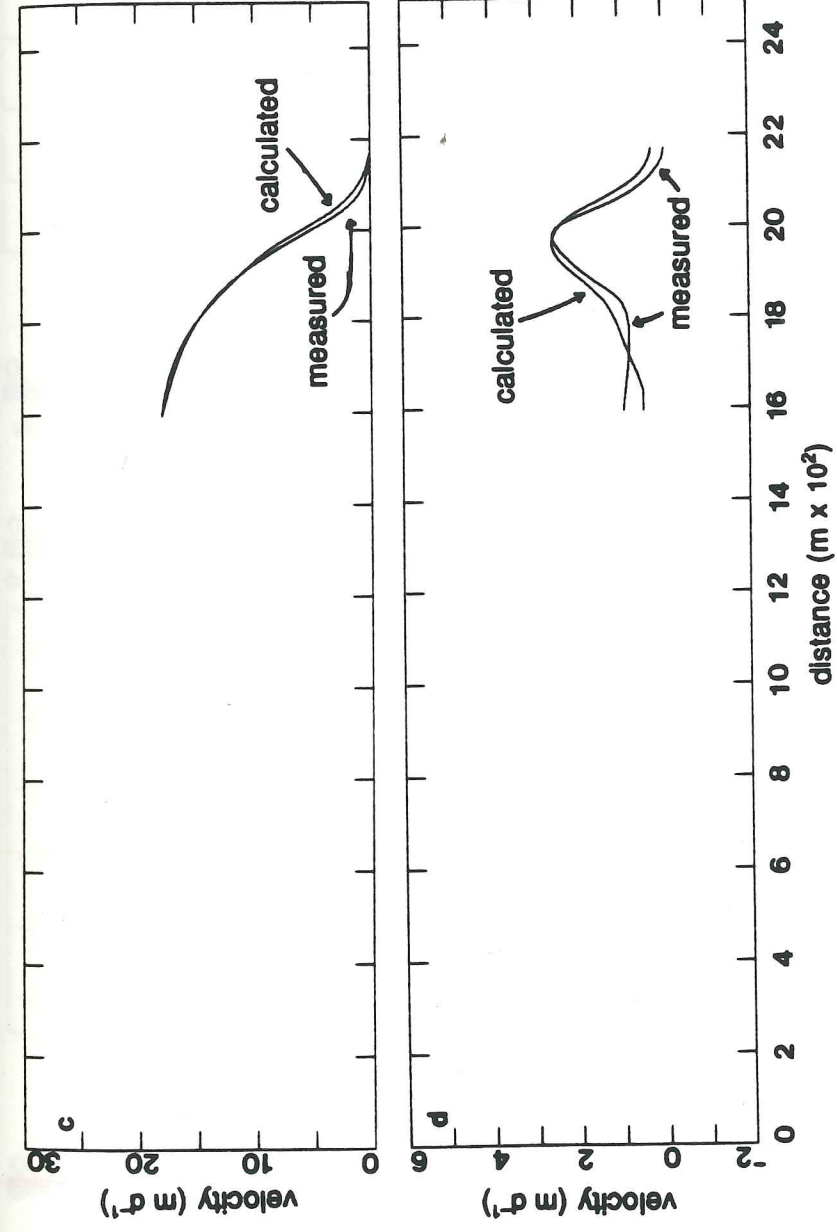


FIGURE 4.4 (continued). c) Horizontal component of velocity at surface; calculated and from measurements. d) Vertical component of velocity at surface; calculated and from measurements.

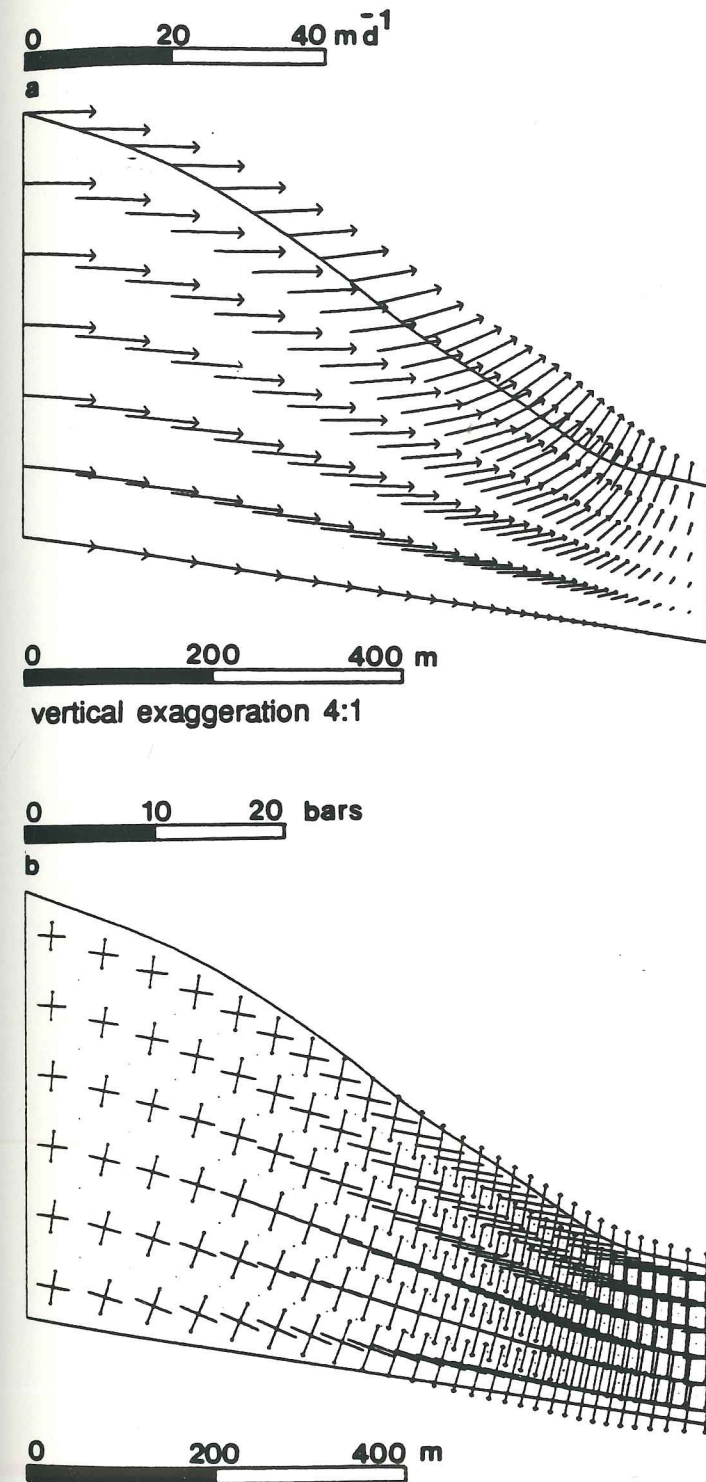


FIGURE 4.5. Finite element velocity and stress solutions for 6 July. a) Velocity vectors b) Principle deviatoric stress vectors. Vectors with arrowheads denote tensile stress; those without denote compressive stress. Vector magnitudes measured from origin of vectors to tip.

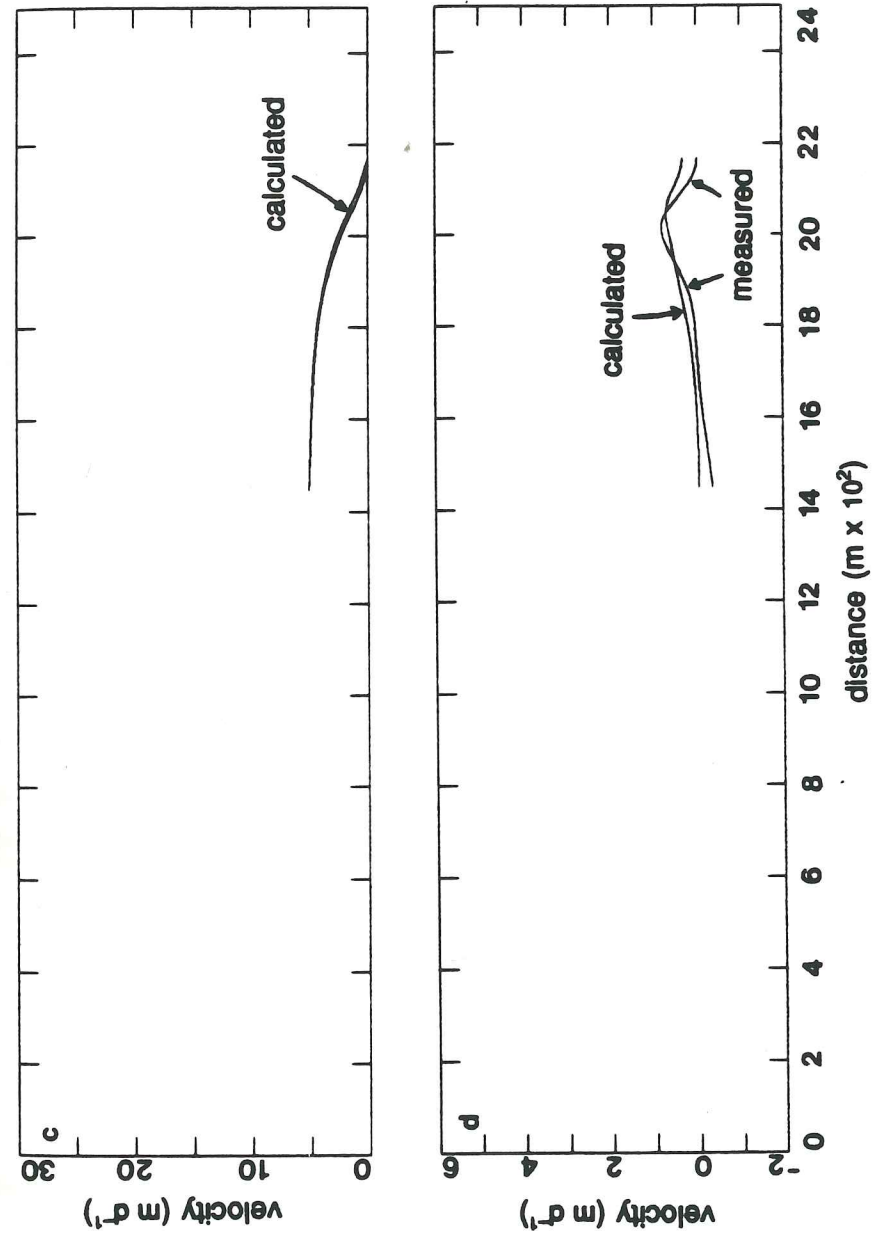


FIGURE 4.5 (continued). c) Horizontal component of velocity at surface; calculated and from measurements. d) Vertical component of velocity at surface; calculated and from measurements.

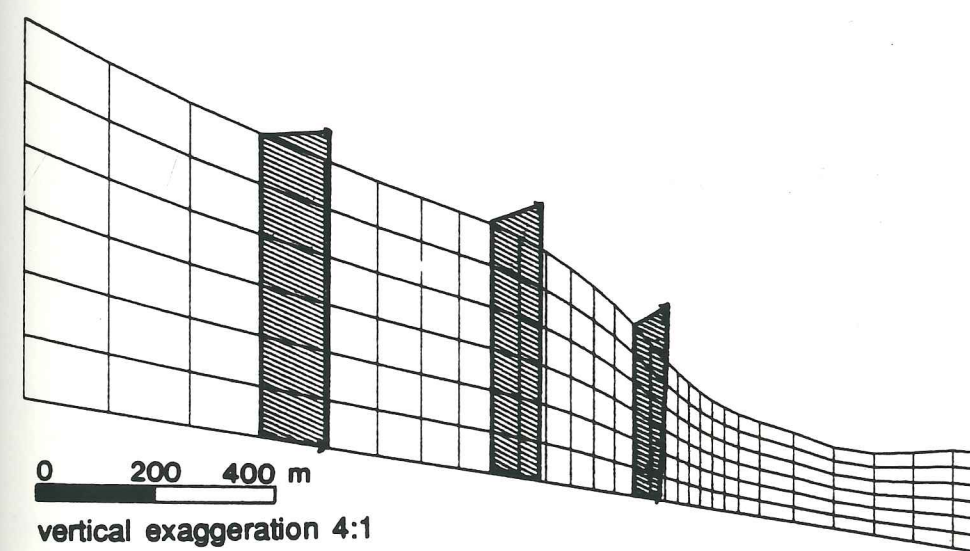


Figure 4.6 Finite element grid for 25 June showing displacement and deformation by 25 June velocity field.

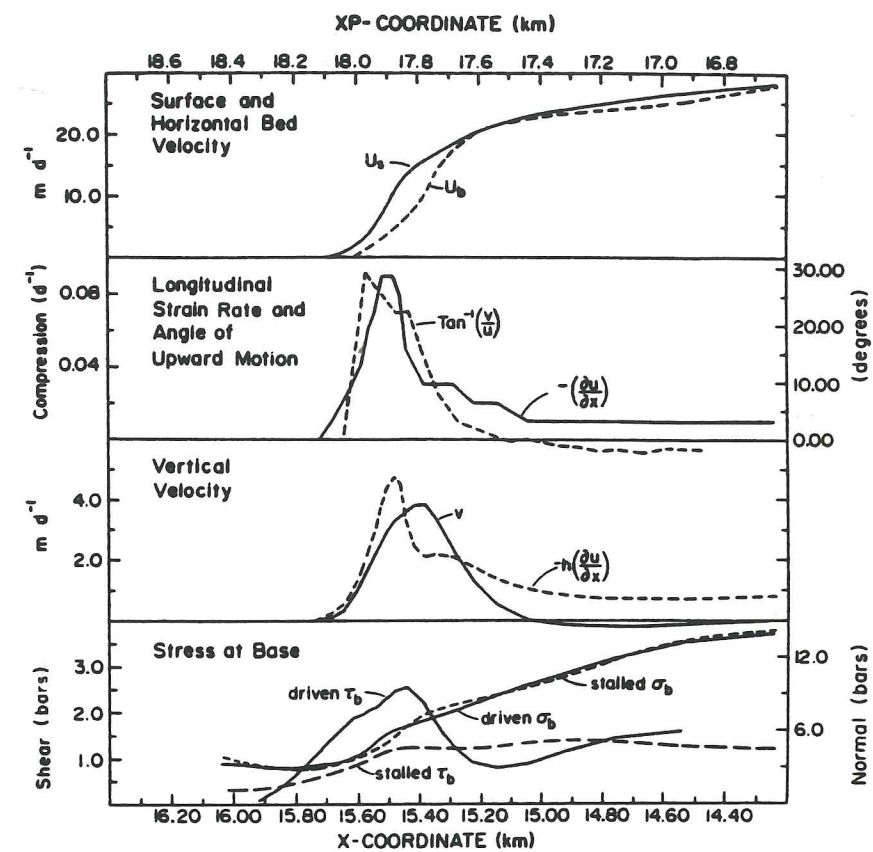


Figure 4.7. Calculated distributions for 22 June of (a) horizontal velocity at surface u_s and bed u_b , (b) longitudinal strain rate $-\partial u / \partial x$ and angle of upward movement γ at surface, (c) thickness times strain rate $h \partial u / \partial x$ and vertical velocity v at surface, and (d) shear stress and normal stress at the bed. In figure 4.7d dashed curves show the stress distribution for the stalled case.

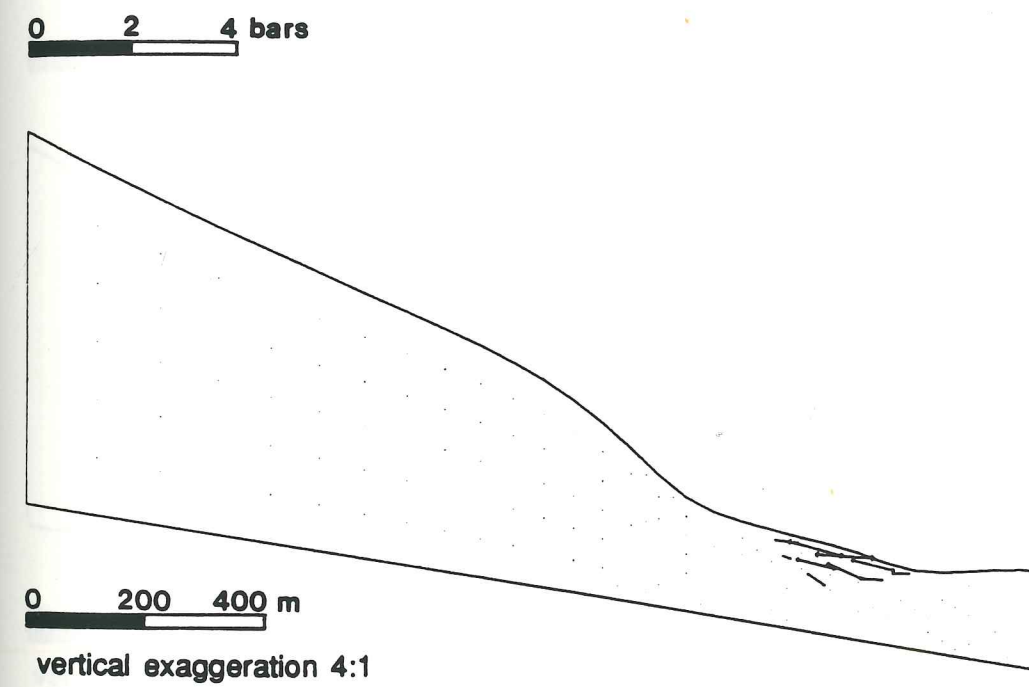


Figure 4.8. Location of tensile stresses on 21 June. Vector orientations represent crack orientations perpendicular to tensile stress. Lengths of vectors proportional to tensile stress magnitude according to scale.

0 5 10 bars

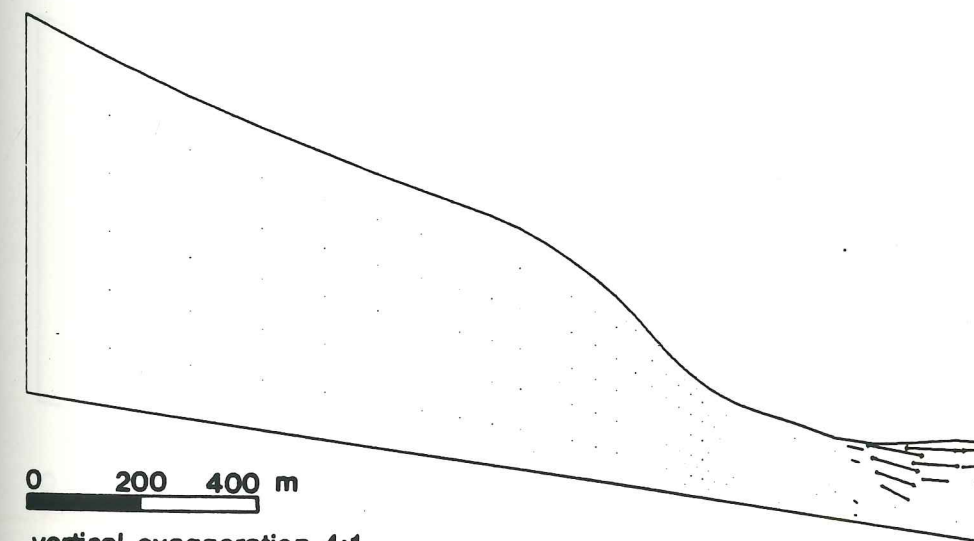


Figure 4.9. Location of tensile stresses on 25 June. Vector orientations represent crack orientations perpendicular to tensile stress. Lengths of vectors proportional to tensile stress magnitude according to scale.

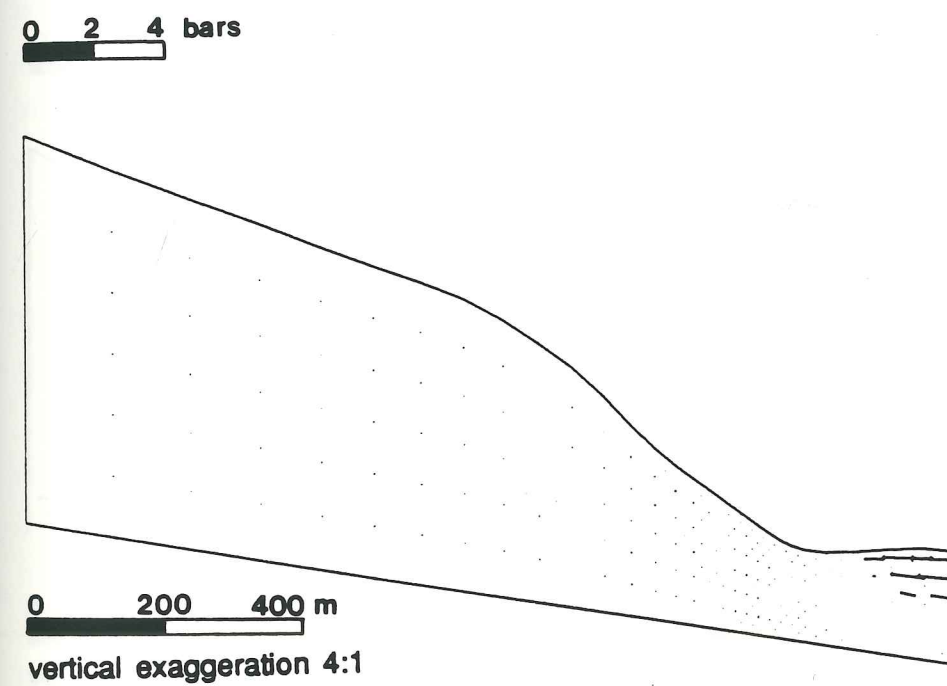
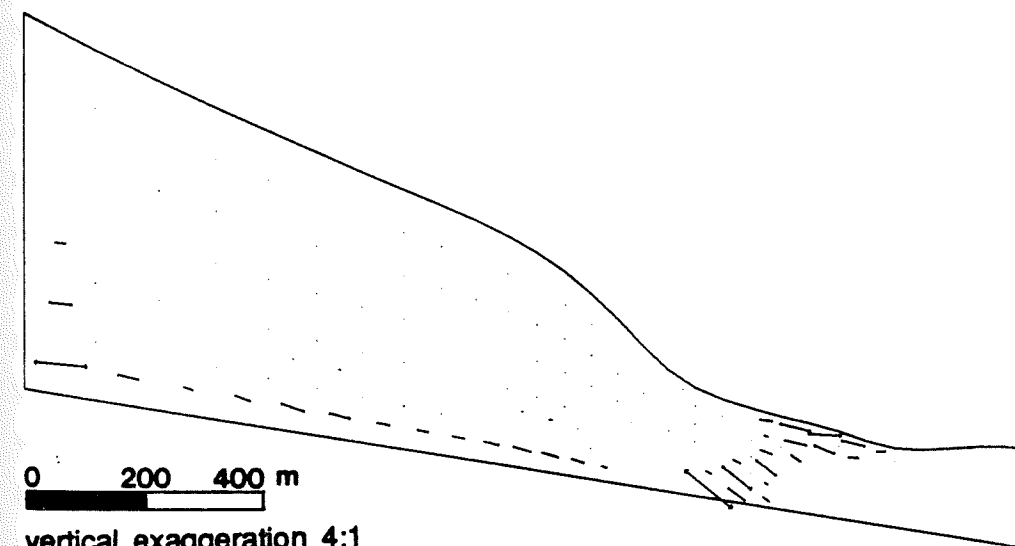


Figure 4.10. Location of tensile stresses on 29 June. Vector orientations represent crack orientations perpendicular to tensile stress. Lengths of vectors proportional to tensile stress magnitude according to scale.

0 5 10 bars



vertical exaggeration 4:1

Figure 4.11. (Hydrofracture) Location of tensile stresses on 21 June with 0 bar effective pressure at bed. Vector orientations represent crack orientations perpendicular to tensile stress. Lengths of vectors proportional to tensile stress magnitude according to scale.

CHAPTER 5

A SIMPLIFIED SURGE FRONT MODEL

5.1 Introduction

In this chapter we will be concerned with characterizing the behavior of the surge front in the most simple terms. In Chapter 2 the observed motion and behavior of the surge front were described, and in Chapter 4 the observations were supplemented by calculations of velocity and stress at depth. These observations and calculations dealt with a fairly complicated geometry which changed substantially with time. In order to identify the basic physical processes which control the advance of the front, we would ultimately like to develop a picture of the surge front motion in which the details of any particular geometry are removed. We would also like to proceed from a model in which the motion is measured to one in which the motion is predicted. As an intermediate step, we will postulate a simple form of propagation for the front, and investigate the requirements to produce the motion in terms of physics or boundary conditions.

The hypothetical model will be presented in two forms. In section 5.2, an analytic model is described in which a simple internal velocity distribution is assumed, thus avoiding the need to deal with the rheology of the ice. This is the simplest model possible which allows the propagating motion of the front to be analyzed. In section 5.3, the same geometrical problem is treated using finite element calculations in place of the assumed internal flow. This model allows us to determine whether the simple model's results adequately reflect the behavior of the true non-linear rheology.

5.2 An Analytic Model of the Front

The analytic model is based on the geometry depicted in Figure 5.1. The glacier in the vicinity of the surge front is composed of two horizontal parallel-sided slabs, one above the surge front ($x \leq x_1$) with thickness h_1 and the other below the front ($x \geq x_2$) with thickness $h_2 \leq h_1$. The topographic ramp of the front joins the two. The geometry of the ramp, $h(x)$, $x_1 \leq x \leq x_2$, is unspecified beyond being continuous in x . The front is assumed to

propagate at speed w without changing its shape ($h = h(x-wt)$). This simple form of propagation is assumed both here and in the finite element model in section 5.2. The purpose of this assumption is both to see if the flow pattern is consistent with observations, and if it is, to allow the velocity which results to stand for any future time. If this is the case, then particle paths, histories of strain rates and total strains can be determined by integrating backwards in time along streamlines in the single velocity field. For the analytic model only, we assume that the horizontal velocity component is independent of depth.

A simple global continuity equation for the region $x_1 \leq x \leq x_2$ in Figure 5.1 provides a relationship between the geometry, ice velocity, and wave velocity:

$$u_1 h_1 = u_2 h_2 + w(h_1 - h_2) \quad (5.1)$$

In this discussion we will consider the special case when $u_2 = 0$, so that the relationship reduces to

$$w = u_1 \frac{h_1}{h_1 - h_2}$$

The objective of the analytic model is to calculate the distribution of velocity $u(x)$, $v(x)$ required to propagate the front forward at speed w with its shape unchanged, given the front geometry $h(x)$. The analysis is simpler in the coordinate system ($x' = x - wt$, y) moving in the horizontal direction at speed w . x and x' are horizontal and positive in the downglacier direction, and y is vertical upward with 0 at the base. The propagating front is stationary in this frame, and particles move in the negative x' direction.

When the horizontal velocity is assumed to be independent of depth, columnwise continuity reduces to the form:

$$u'(x')h(x') = C \quad (5.2)$$

where C is a constant. Here, u' is the horizontal velocity in the moving coordinate system and h is the thickness of the ice. This is the general solution to the differential equation

$$\frac{d}{dx'}(u'h) = 0$$

The thickness and velocity at x'_2 provide the most useful boundary conditions for equation 5.2. For $x' \geq x'_2$, $u = 0$ (this is not required, but is true if the ice below the surge front is stationary), so $u' = -w$. From this we get

$$-wh_2 = C$$

so the horizontal component of velocity in the moving coordinate system is

$$u'(x') = -w \frac{h_2}{h(x')} \quad (5.3)$$

The vertical velocity is related to the horizontal velocity by the incompressibility condition (in the form particular to the assumption of depth-independent horizontal velocity):

$$\begin{aligned} v'(x') &= -h(x') \frac{du'(x')}{dx'} \\ &= -wh_2 \frac{dh(x')/dx'}{h(x')} \end{aligned} \quad (5.4)$$

Equations 5.3 and 5.4 are the components of velocity at the surface which will cause the surge front to propagate forward with its shape unchanged. The horizontal velocity at depth is given by Equation 5.3 for $u'(x')$, and

$$v'(x', y) = -y \frac{du'(x')}{dx'}$$

for the vertical component. Streamlines follow the surface for particles initially on the surface, and follow parallel paths with the vertical coordinate scaled by y/h_2 for particles initially at height y above the bed at $x' = x'_2$.

Particle paths must be determined to calculate velocity and strain histories for individual particles. Only the x coordinate of the position need be calculated, for the vertical coordinate for any point in the future is determined by its initial value and future x coordinate. We shall only be concerned with particle paths on the surface. The velocity

$$u'(x') = dx'/dt$$

can be integrated to give the time as a function of position:

$$t - t_0 = \int_{x_0}^{x'} \frac{dx'}{u'(x')} = \frac{-1}{wh_2} \int_{x_0}^{x'} h(x') dx' \quad (5.5)$$

This function can be tabulated to provide a list of (t, x') pairs. It would be more convenient to be able to write a function $x'(t)$ for a particle, but this is not easy in general because $u'(x')$ is not an explicit function of t .

Strain rate can be written as a function of x' :

$$\frac{\partial u'}{\partial x'} = -wh_2 \frac{\partial}{\partial x'} \frac{1}{h(x')} = +wh_2 \frac{\partial h/\partial x'}{h^2(x')} \quad (5.6)$$

To get strain rate as a function of time, the table of (x', t) pairs from equation 5.4 is inverted to provide tabulated $x'(t)$ at chosen points x' (unequally spaced t). Equation 5.6 is evaluated at the tabulated x' and the resulting $(\partial u'/\partial x', t)$ pairs are tabulated. Finite strain is calculated by summing strain rates over the appropriate time intervals. (As in previous calculations, the strain is coaxial.)

Analytic model results: Sinusoidal front

The analytic model was tested first with a sine-shaped topographic ramp. This was represented by

$$h(x') = \bar{h} - \frac{\Delta h}{2} \sin\left(\frac{\pi}{\Delta x'}(x' - \bar{x}')\right) \quad x'_1 < x' < x'_2$$

where $\bar{h} = (h_1 + h_2)/2$, $\Delta h = (h_1 - h_2)$, $\bar{x}' = (x'_1 + x'_2)/2$, and $\Delta x' = (x'_2 - x'_1)$. The problem is normalized by choosing the scale length $h_2 = 1$ and the scale velocity $w = 1$. The proportions of the topographic ramp in the terminus region varied during the surge, but a typical shape can be defined by choosing $h_1 = 2.5$ and $\Delta x = 5.5$.

Figures 5.2a-5.2d show, respectively, the particle path, horizontal velocity, vertical velocity, and strain rate for a parcel of ice which is on the surface at the downglacier edge of the front at time $t = 0$.

The particle path (Figure 5.2a) shows the elapsed time t in normalized units as a function of the normalized position x' , starting at $x' = 5.5$ (at the base of the surge front) at $t = 0$ and ending at $x' = 0$ (at the top of the surge front) at $t = 9.6$. The travel time is defined to be the time required for a parcel of ice to traverse this path. At a normalized speed of $w = 1$, the front travels 9.6 distance units in 9.6 time units, or 1.75 times the front width $\Delta x = 5.5$. The particle, on the other hand, has traveled the same distance as the front less Δx , since it ends up at the top of the front, and so has traveled only 4.1 units. The average velocity of the particle passing through the front is thus $0.42w$.

To give the normalized units an interpretation appropriate to the size and speed of the front in the terminus region, we set $h_2 = 45$ m, and $w = 40$ m d⁻¹. The elapsed time for the particle to travel to the top of the front is then $9.6h_2/w = 10.8$ d. During this time the front

one or the other will be forced further out of agreement by any change. This problem is evidently related to the chosen shape of the front $h(x)$, and will be treated in the next model.

Composite data front

We now move away from the assumed sinusoidal topography of the front and adopt instead a smoothed and normalized composite of all the measured front profiles between 21 June and 5 July (Figure 5.3). The base elevation has been subtracted from the profiles, so the composite is a thickness profile on a horizontal bed at $y = 0$.

The model calculations proceed exactly as in the previous case, except that $h(x)$ is tabulated rather than supplied by a formula. The interpretation of the results is complicated by the fact that the surface is sloped everywhere, so the downglacier and upglacier limits of the front zone (corresponding to h_2 and h_1) are not precisely defined. The front zone is approximately the steepest region of the profile, and is thus defined to be the region between $x' = 3.9$ and $x' = -3.5$ (normalized units in which $h_2 = 1$) in Figure 5.3a, so $\Delta x = 7.4$.

Figure 5.4a shows the particle path through the complete section. The total travel time is 62.6, while the travel time through the front zone is 13.7. The appropriate glacier units are $h_2 = 40$ m and $w = 40$ md⁻¹, so the time unit is 1 day. During the passage of the particle through the front zone, the front has moved $13.7w = 548$ m, while the particle has moved $548 - \Delta x = 252$ m at an average speed of 18.4 md⁻¹, or $0.46w$. Compared to the sine-front model, the travel time is longer (by 27%), owing largely to a larger Δx (by 20%). The longer Δx in the composite model is the result of including the early days of the period (21 June and immediately thereafter), when the front had a more elongated profile than the 3x5.5 ratio chosen for the sine model. The average speed and ratio of average velocity to wave speed are comparable, however.

The horizontal velocity (Figure 5.4b) shows the same pattern seen in the previous model, except that here, the velocity profile extends over the entire topographic profile, rather than being restricted to the front zone. In the glacier units defined above, the maximum horizontal velocity (0.71) is 28.4 mday⁻¹, or $0.71w$. The vertical velocity (Figure 5.4c) also follows the expected pattern, rising to a maximum of $0.07 = 4.28$ md⁻¹ in the front zone. A small inflection appears in the vertical velocity peak at $t = 3.75$. This is the

result of flow over a small inflection in the topography near $x' = 6.0$.

The strain rate (Figure 5.4d) shows the same pattern as seen in Figure 5.2d, except for the addition of a secondary peak arising from the same source as the inflection in the vertical velocity. The maximum compressive value attained is -0.71 d^{-1} , and the total strain through the surge front is -0.61 . The total strain through the entire section is -1.24 .

The composite model has produced patterns of velocity and strain rate similar to the observed pattern and to the pattern calculated for the sine-front model, and the magnitudes of strain rate and finite strain are now within the limits of observations. The travel time still exceeds observed time, but as was discussed earlier, this quantity is directly related to Δx , and Δx is large in the composite model owing to the contribution of the early days data. The overall shape of the strain rate pattern results from the presence of a topographic ramp joining the downglacier and upglacier reaches of the glacier profile. The shape of the strain rate in its small features results from the specific shape of the front. More importantly, the magnitude of the maximum strain rate is sensitive to the details of the shape. Total strain is completely determined by the total thickness change (given the simple flow assumption), and travel time is controlled primarily by Δx .

On the basis of the two models presented here, it appears that the surge front propagation in the terminus region (as depicted by its behavior at the surface) proceeded in a way compatible with the two following assumptions: 1) The motion preserved the shape of the front zone in a steady state, displacing it downglacier at a constant rate w . 2) The horizontal (or bed-parallel) component of the flow did not vary with depth. The preservation of the front shape is applied in these models as a constraint, but may have been only coincidental in the terminus region of the glacier, and was in any case only approximately satisfied. What the real constraints are on the front shape is a more complex matter, involving subtle interactions between front geometry, internal deformation at the base, basal hydrology, and basal sliding. Without going into such details we can do no better at present than to observe that the assumption of a steady state gives fairly satisfactory results, and simplifies considerably the task of calculating strain rates and finite strains.

The assumption of depth-independent horizontal velocity is also a convenient assumption for the present models, and has been justified by the finite element analyses of Chapter 4. This assumption may be further justified, however, by returning to a finite element

model, in which the non-linear rheology of ice is re-introduced.

5.3 A Finite Element Model of the Steady State Front

For the steady state problem, a finite element grid (Figure 5.5a) is formed based on the geometry of the composite front presented in the last section. The calculations proceed exactly as described in Chapter 4, and the results are presented in the same form.

The velocity solutions in Chapter 4 were obtained by adjusting the basal velocities to produce surface velocities which match the observations. In the present case, the basal velocities have been adjusted to produce a match at the surface with the steady state velocity profile prescribed by equation 5.3. As in previous calculations, a match is attempted only in the horizontal component, since there are not enough degrees of freedom in the boundary conditions to satisfy both the horizontal and vertical components. The velocity solution is shown in Figure 5.5b. In general pattern, the velocity solution resembles the solutions of Chapter 4, bearing in mind that the model region corresponds only to the area above the stagnant zone (stationary ice) in the Chapter 4 solutions. The resemblance is also close between the model and the velocity field on 6 July, after the termination of the surge. Despite the fact that the 6 July velocities were much lower (5 m d^{-1} maximum) than surging velocities, the velocity was still high by normal standards, and the flow was still dominated by basal sliding.

Deviatoric stresses (Figure 5.5c) again show the typical pattern, with principle stresses greatest in the front zone, oriented nearly parallel and perpendicular to the bed at the leading edge of the front and rotating to positions indicative of higher basal shear in the central part of the front zone. As with the other finite element solutions, the stresses have slightly anomalous orientations near the bed at the upglacier end in response to small errors in the end boundary conditions. Adjusting the boundary velocity at the upglacier end to allow a very small amount of shear deformation in the elements near the base would improve the stress orientations here, but would not affect the stresses in the front zone or have any substantial effect on the velocity field.

Figure 5.6a shows the match between the bed-parallel component of the calculated and hypothetical velocities. Over most of the profile the calculated and hypothetical velocities match or are within a few per cent of each other. The maximum mismatch is about

15% near the midpoint of the front zone; the shape is essentially identical, however, and the mismatch is insignificant in terms of its effects on the pattern of strain which will be derived from the velocity distribution. The match was achieved by the procedure described in Chapter 4. Also included is the velocity applied at the base. The bed-normal component (Figure 5.6b) shows generally good agreement. Deviations at the ends are another consequence of end boundary conditions. At the maximum ($\approx 3 \text{ md}^{-1}$), a discrepancy exists, with the calculated velocity being 0.78 md^{-1} less than the hypothetical velocity. This difference can be explained by noting that at the same place, the calculated bed-parallel velocity is slightly higher than the velocity required for a steady state. Continuity forces a reduction in the bed-normal component, which, having a smaller magnitude, shows a larger proportional change.

While local differences between the hypothetical and calculated bed-normal velocity can be explained in terms of corresponding differences in the bed-parallel component, it will be noted that the pattern of velocity discrepancy over the length of the model region is similar to that found in Chapter 4, from which it was inferred that volume was not conserved in the glacier. Such a conclusion makes no sense in the present case, since both the hypothetical and finite element models conserve volume by definition. The discrepancy here is to be interpreted in a different way, because different assumptions were made in constructing these models. In the present case, both sources of velocity profiles (hypothetical and finite element models) conserve volume, but only one is precisely steady state (the hypothetical model). In Chapter 4, both sources (measurements and finite element model) were assumed to be steady state, but only one (the finite element model) was known to conserve volume. A final thickness difference between two volume conserving models, one steady state and one not, simply indicates that the non-steady state model produces a different final thickness. Two steady state models, however, each with the same upstream thickness, must maintain that thickness, and a net difference in vertical velocity (integrated over the model length) is interpreted as a failure to conserve volume on the part of the model not constrained to do so.

It is plain from the agreement in the bed-parallel component, which carries the bulk of the flux, that the hypothetical flow regime for a steady state front, based on the depth independent bed-parallel velocity and a steady state profile, is an adequate approximation to the results of the finite element calculation with a realistic non-linear rheology and a

reasonable basal velocity distribution.

5.4 Summary

The objectives of this chapter have been to investigate the propagating motion of the surge front without becoming involved in the details of a particular geometry, and to create a simple picture of the flow in the surge front in which the essential details of the deformation are present. We have looked at the motion of the front in two geometrically simple forms, a sinusoidal front and a smoothed composite of the observed fronts, and found that the basic features of the observed flow are still present. Evidently the propagation of the surge was not strongly influenced by obscure geometric effects peculiar to the actual shape of the glacier terminus. As for the simple picture of deformation, we have found here, as we did in Chapter 4, that when viewed on the large scale, the bed-parallel flow is indeed essentially independent of depth, and the propagation of the front and the straining of the ice which passes through it can be understood in terms of that simple flow and the continuity equation. We say that this is true "on the large scale", for there is certainly a very complicated kind of deformation occurring in a narrow zone at the bed in the surge front. We have avoided dealing with this zone by simply invoking a distribution of basal velocity which meets our needs. It also has not influenced the structures observed at the surface.

This unaddressed deformation at the bed is related to the second major assumption made in these models: that the front propagates with its shape unchanged. We have seen that this is an adequate assumption, for a velocity distribution which preserves the front shape also produces sequences of velocity and strain in time which agree in general points of shape and magnitude with observations. We see that the shape of the surge front did change slightly with time, but we can also see that the front was entering stagnant ice whose geometry was not perfectly uniform. Our conclusion is that the front changed shape as it moved only to the extent that it was entering variable initial topography. Since the front propagated at a more or less constant shape and speed, we conclude that the zone of sliding moved downglacier at a comparably steady rate, and that its location was controlled primarily by the local front geometry.

The hypothetical model shows that the front can be propagated forward by a realistic

velocity field which satisfies the continuity condition (equation 5.2). Finite element calculations show that the observed deformation, which necessarily includes a zone of complex deformation at the base, is compatible with the simple large-scale picture of flow adopted in the hypothetical model. Because of the simple flow pattern, finite strains can be evaluated without complex numerical calculations. In the absence of variations in quantities which are boundary conditions for equation 5.2, the advance of the leading edge of the sliding is controlled by deformation in the front zone. Evidently it is possible, at least when viewed on a kinematic level, for the advance to occur in a steady-state, self-perpetuating fashion.

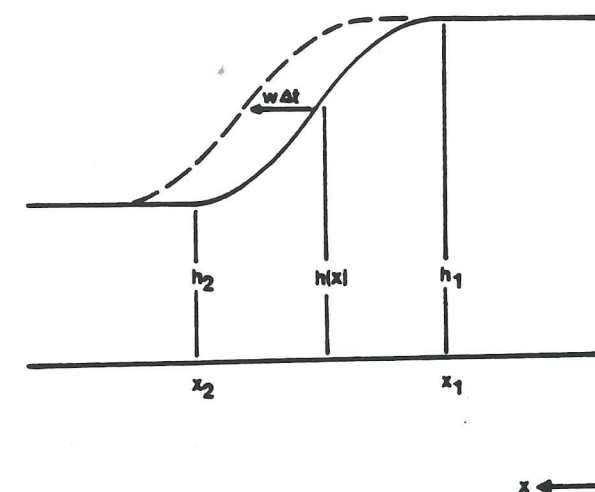


Figure 5.1 Schematic of idealized surge front geometry.

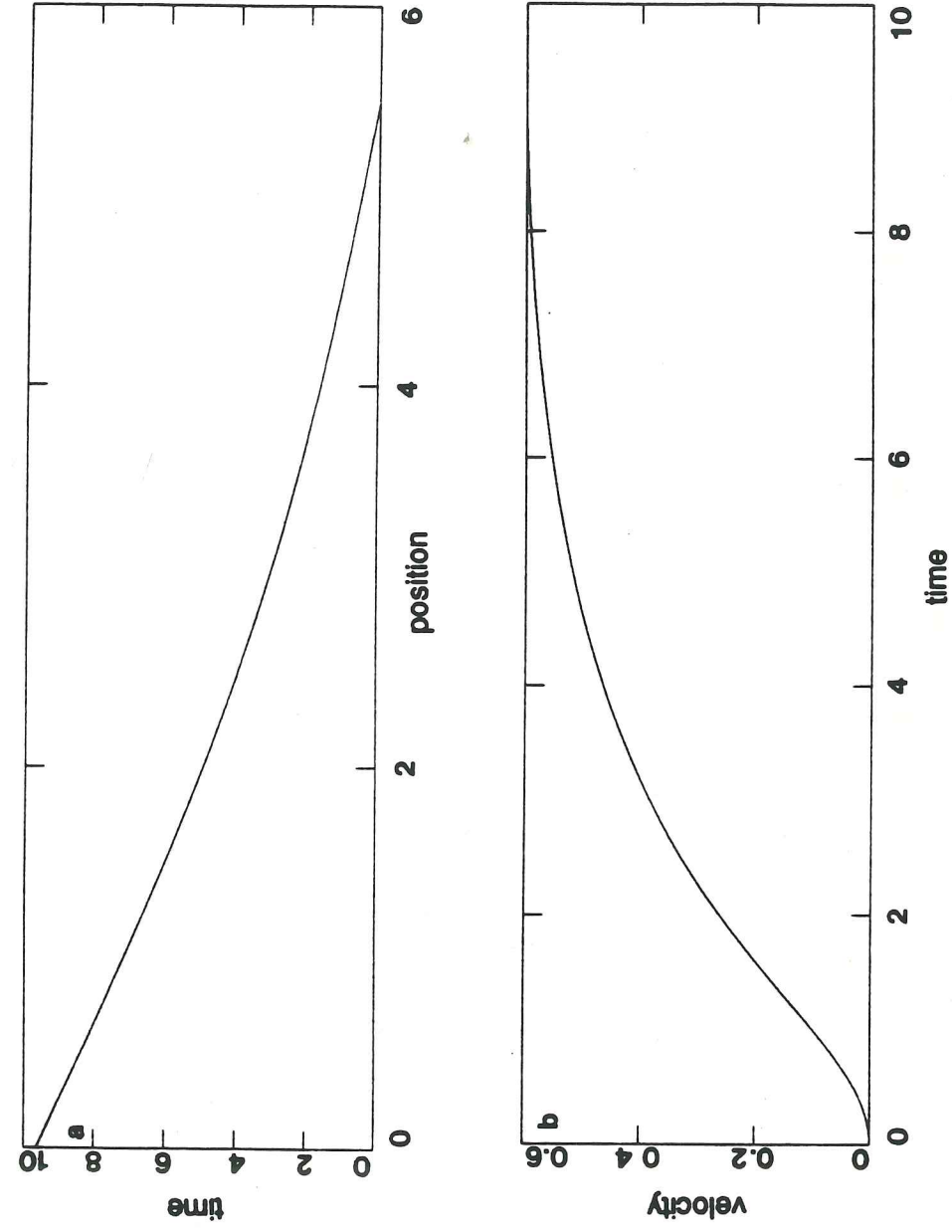


Figure 5.2. a) Particle path for sinusoidal front. b) Horizontal component of velocity for sinusoidal front. Position, time and velocity are dimensionless.

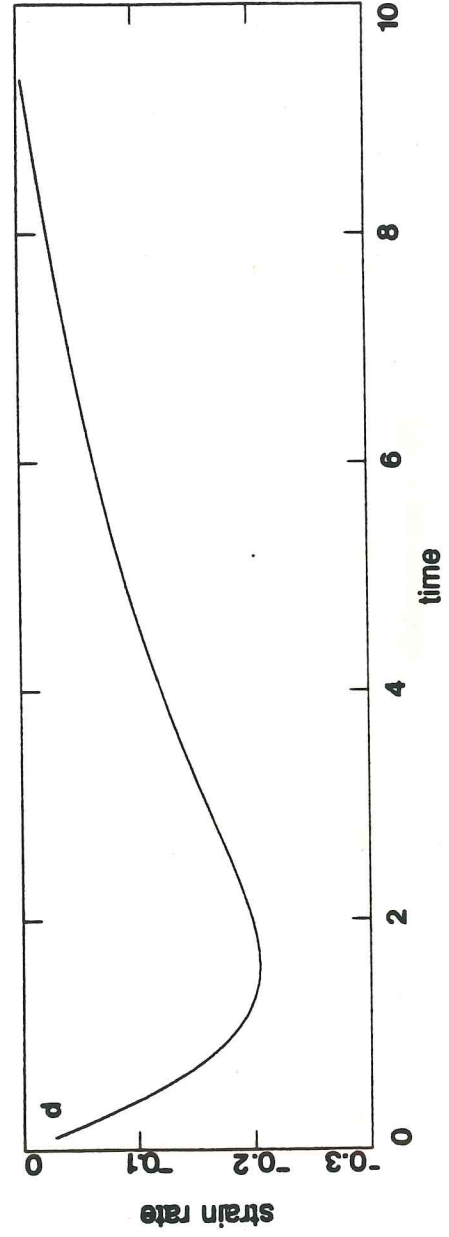
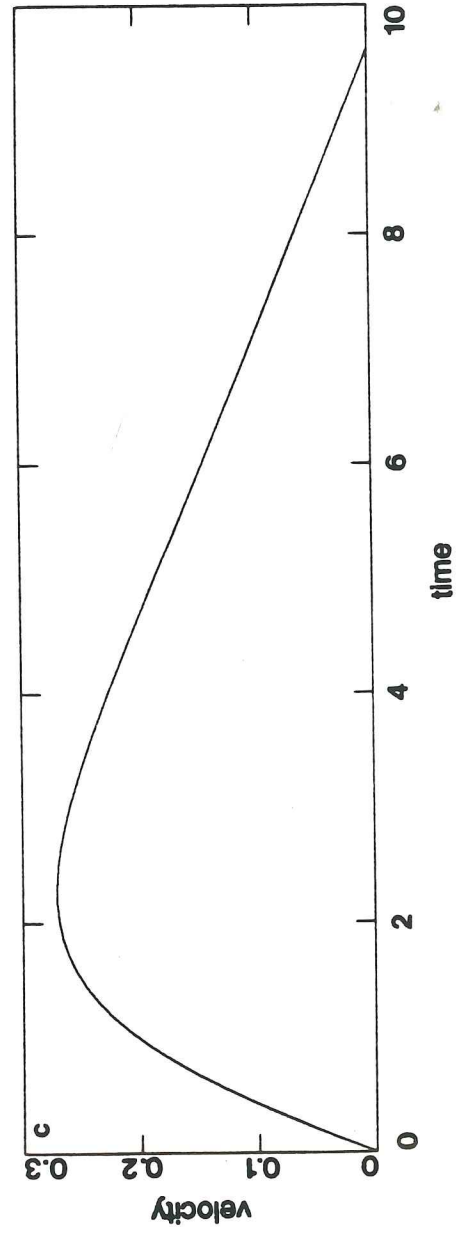


Figure 5.2 (continued). c) Vertical component of velocity for sinusoidal front. d) Strain rate for sinusoidal front. Position, velocity and strain rate are dimensionless.

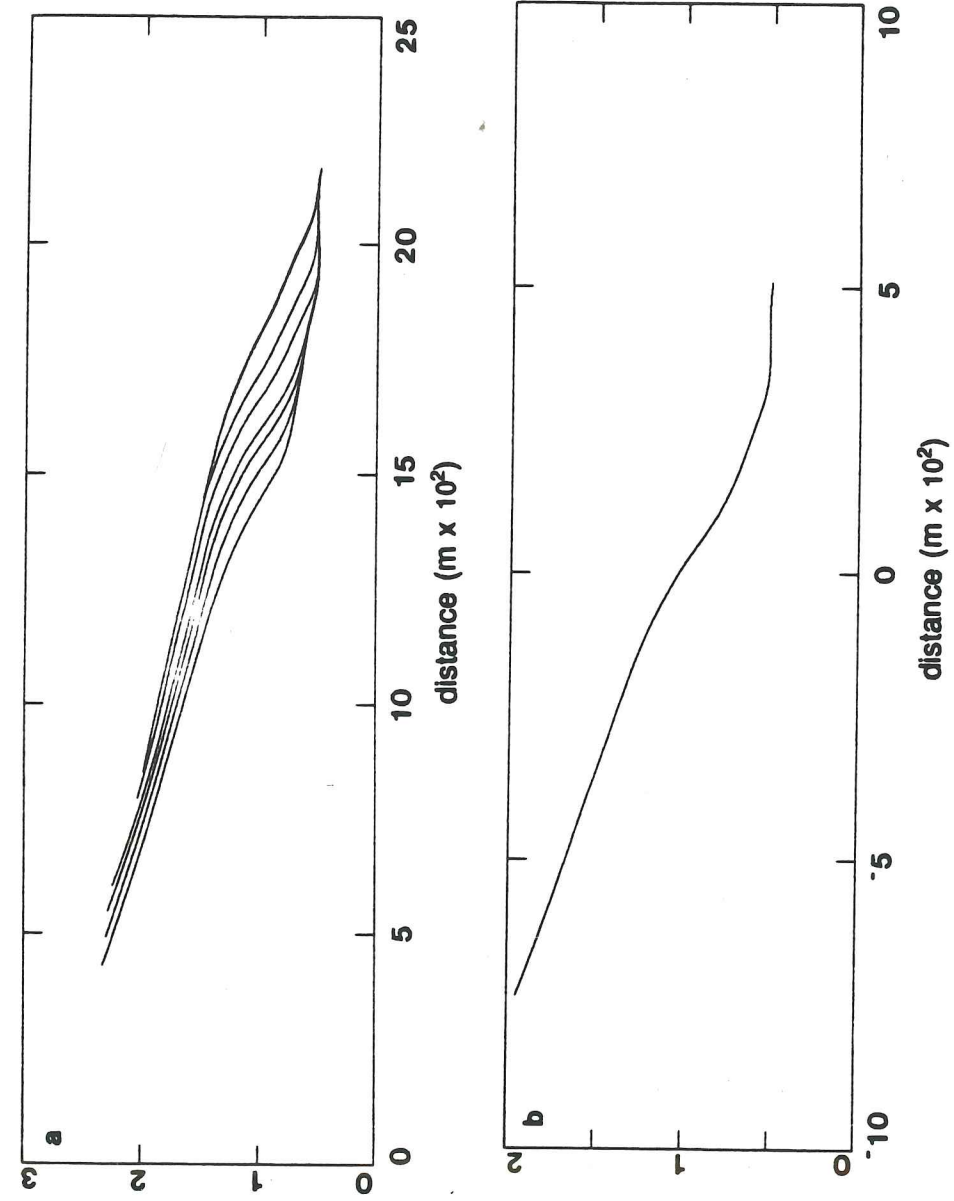


Figure 5.3. Construction of composite front. a) Individual profiles. b) Average profile. Curves are shifted to superimpose point of maximum slope for each day, and elevations averaged.

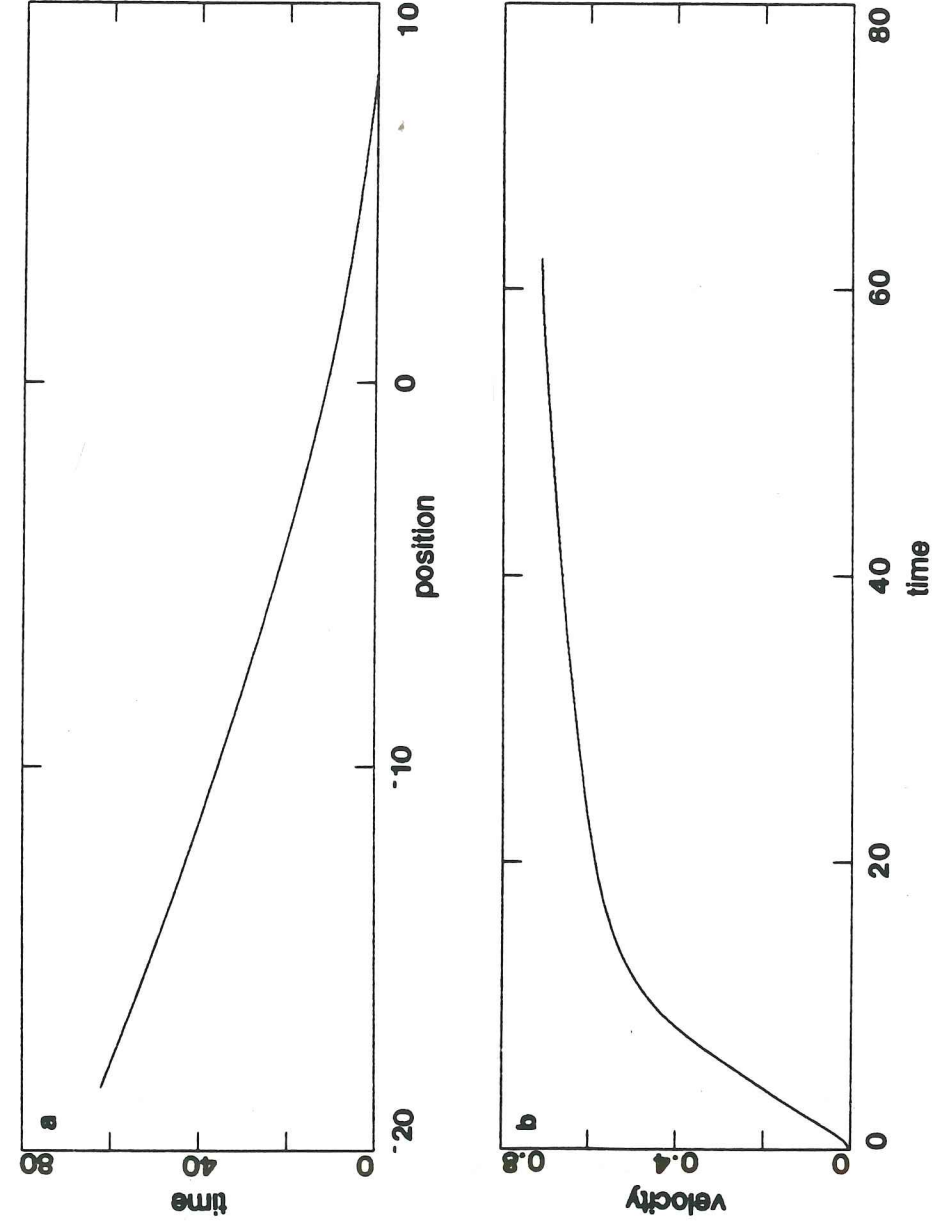


Figure 5.4. a) Particle path for composite front. b) Horizontal component of velocity for composite front. Position, time and velocity are dimensionless.

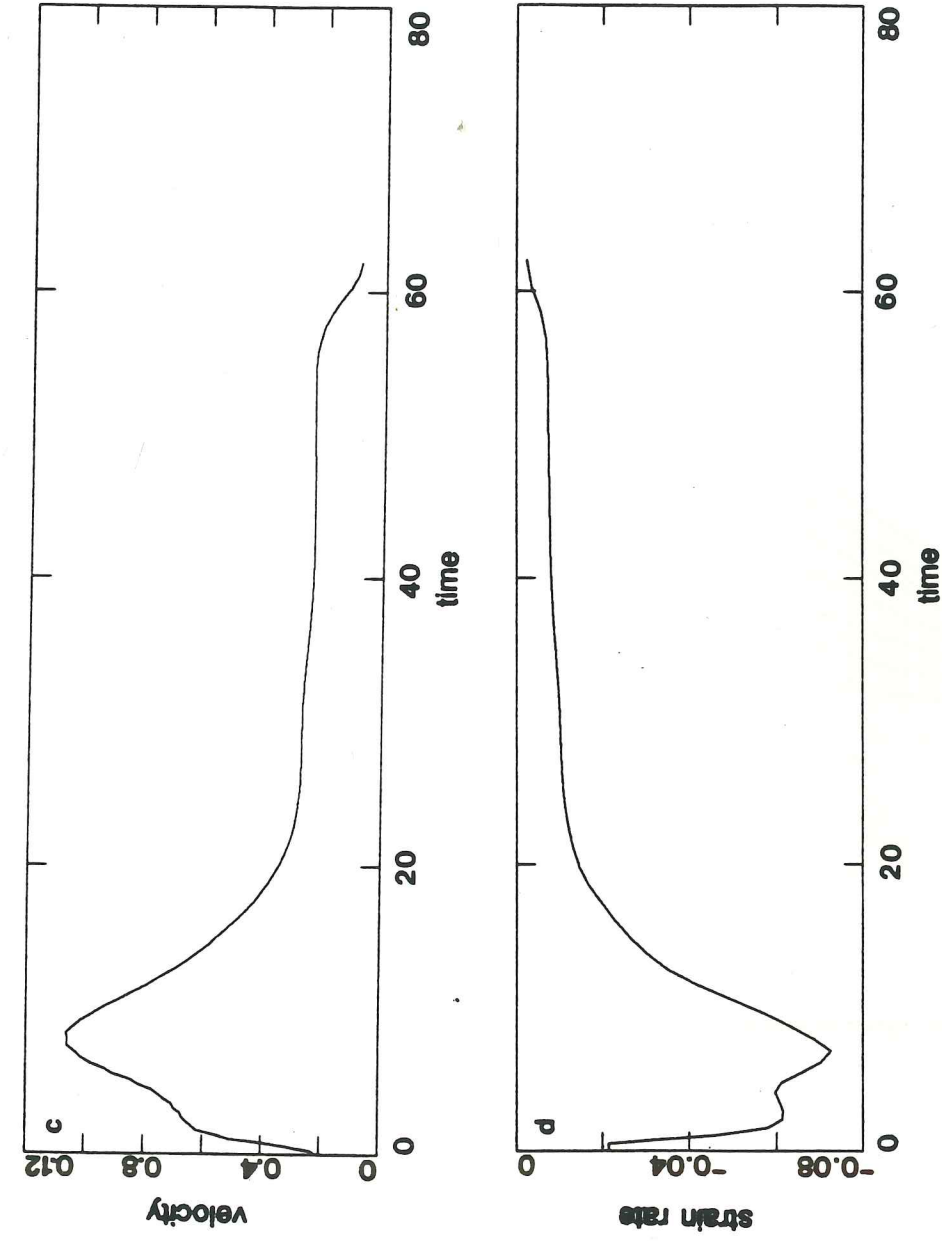


Figure 5.4 (continued). c) Vertical component of velocity for composite front. d) Strain rate for composite front. Position, velocity and strain rate are dimensionless.

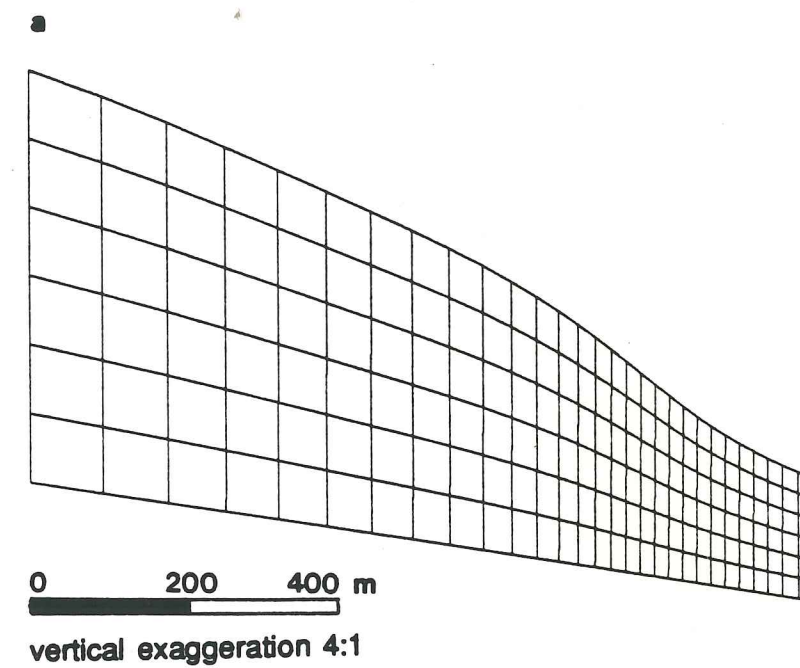


Figure 5.5. a) Finite element grid for composite surge front.

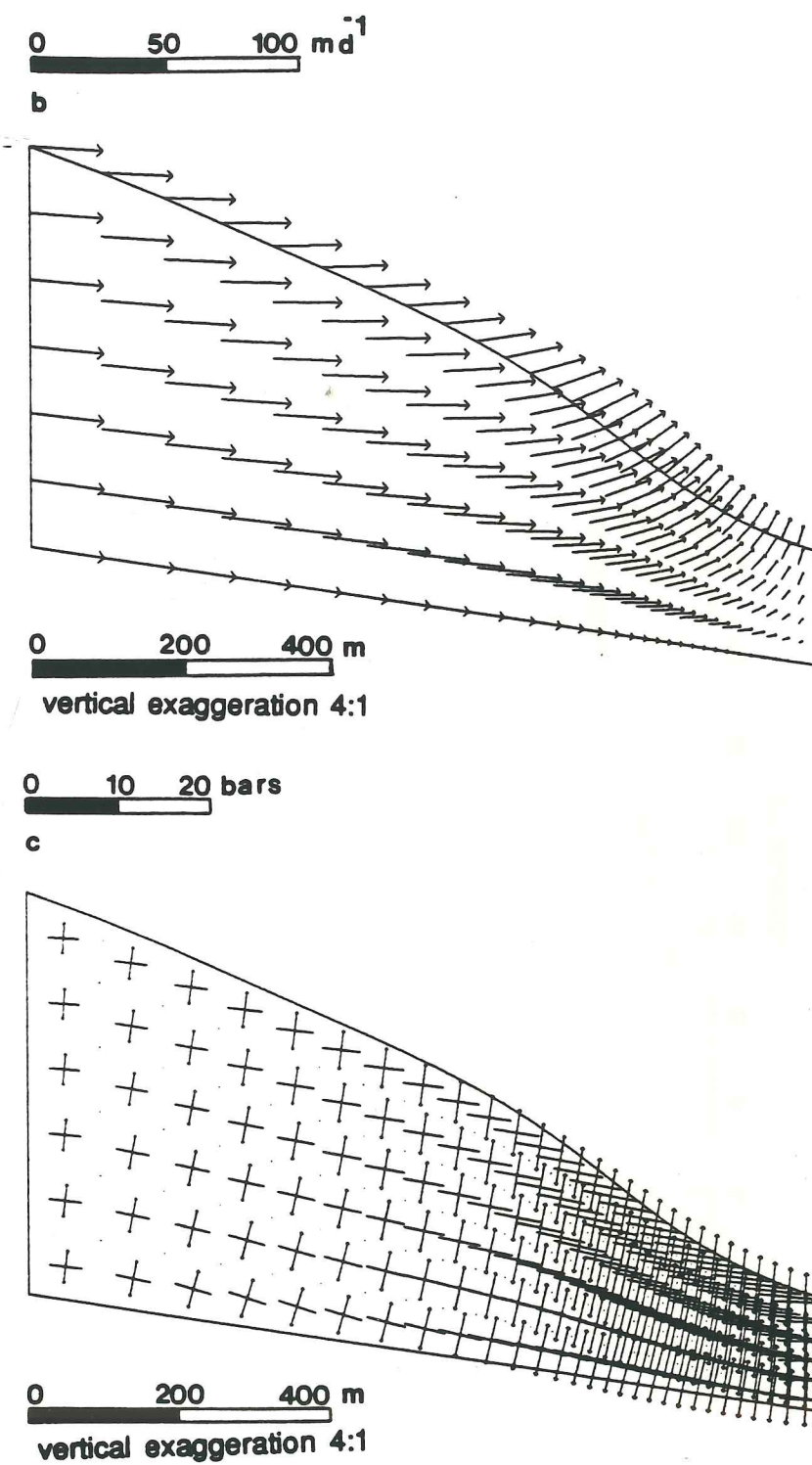


Figure 5.5 (continued). b) Velocity vectors. c) Principle deviatoric stress vectors. Vectors with arrowheads denote tensile stress; those without denote compressive stress. Vector magnitudes measured from origin of vectors to tip.

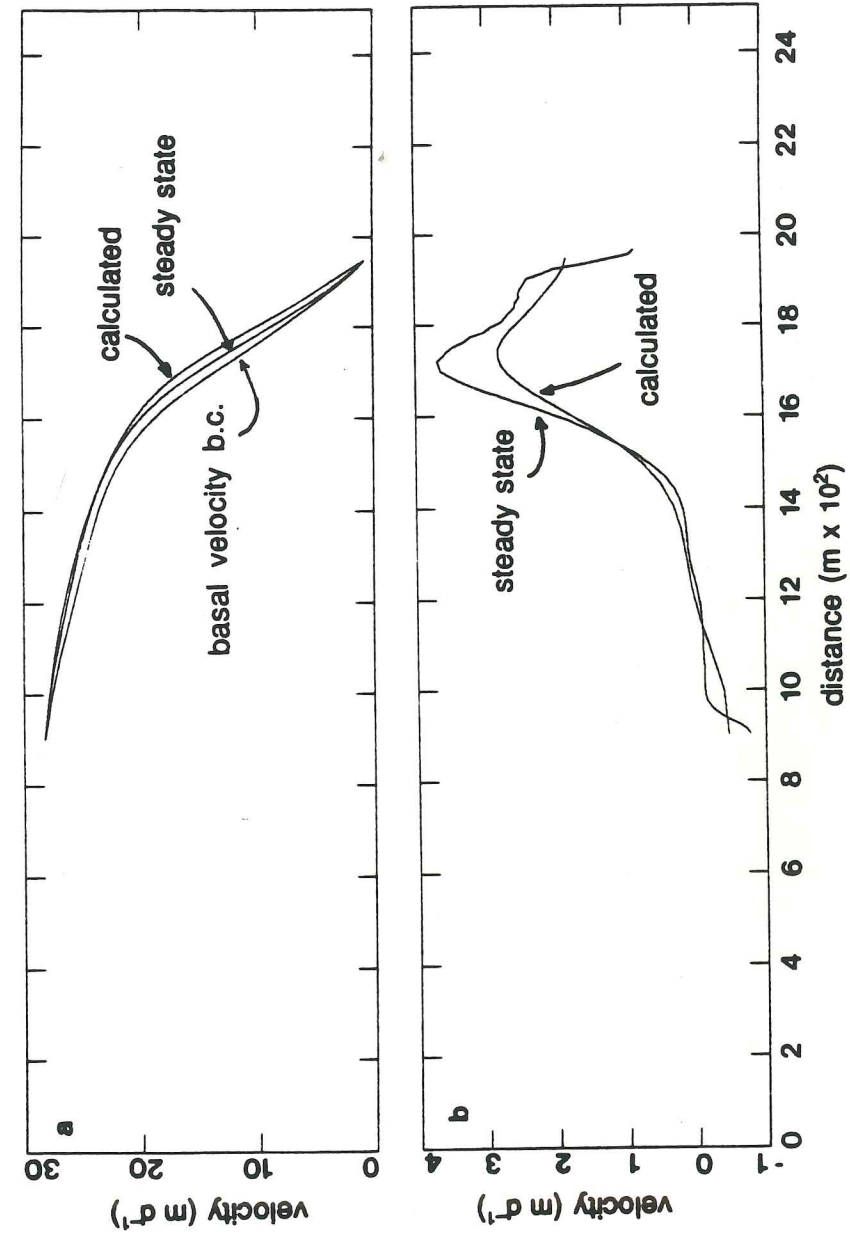


Figure 5.6. Velocity solution at surface. a) Horizontal component. b) Vertical component.

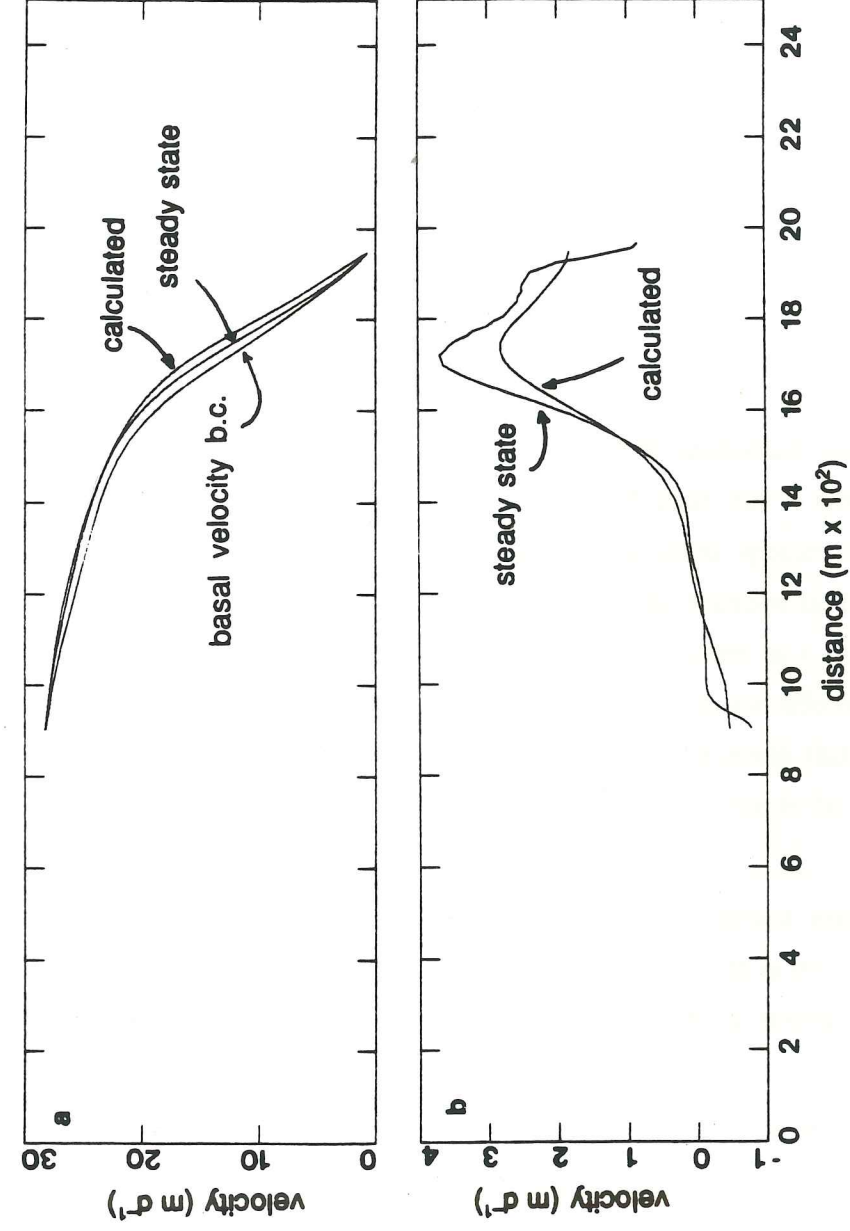


Figure 5.6. Velocity solution at surface. a) Horizontal component. b) Vertical component.

CHAPTER 6

SUMMARY AND SYNTHESIS

6.1 Introduction

In the preceding chapters we have presented a detailed analysis and interpretation of observations made at Variegated Glacier during and after its surge, which pertain to the kinematics of deformation in the terminus region and the structures which were developed there as a result of the deformation. Here we give a summary interpretation of the observations and their interpretations (6.2), followed by a recapitulation of the major conclusions of this work.

6.2 Descriptive Summary

Initially, the ice in the terminus region is composed of interlocked coarse grains; bubble content is moderate, with small (≈ 10 cm) regions of clear ice. A moderate to strong subhorizontal foliation (S_b) formed of bubble density variations appears in thin ice lying beyond the limit of the 1982/83 surge. Appearing with the foliation is a weak multiple-maximum crystallographic c-axis fabric with the maxima oriented in a cluster around the vertical direction. Neither this foliation nor this fabric appear in ice affected by the surge. In ice throughout the terminus region, primary depositional layering (S_0) is present in a subhorizontal orientation with very little shear deformation. The ice is 50-100 m in thickness, and is essentially stationary prior to the surge.

A kinematic wave of rapidly increasing horizontal and vertical velocity, called the surge front zone, approaches the stationary ice at approximately 40 m d^{-1} . A column of ice standing in advance of the front zone is subjected to the following events during its arrival and passage:

Once within a 200-300 m width of the leading edge of the front zone, the column develops vertical tensile stresses in near-surface layers due to the longitudinal gradient in vertical velocity. The stresses create surface-parallel fractures.

The leading edge of the surge front arrives, defined by a rapid ($< 1 \text{ d}$) onset of high ($> 1 \text{ m d}^{-1}$) horizontal velocity. The column is now in a region of high longitudinal compression ($\approx -0.1 \text{ d}^{-1}$) and rapidly increasing horizontal and vertical velocity. The

horizontal velocity is essentially constant over the depth of the column, with 95% or more of the velocity at the surface being the result of basal sliding. The horizontal velocity rises monotonically to 20-30 m d⁻¹ at the upglacier end of the front zone, and maintains the high velocity in the surging ice behind. The vertical velocity rises to a maximum (≈ 5 m d⁻¹) in the middle of the front zone, then diminishes (1-2 m d⁻¹) near the upglacier end of the front zone. The vertical velocity at its maximum is greater than can be explained by continuity of ice and the longitudinal strain rate. The development of some kind of void space within the glacier is evidently responsible for the excess velocity.

Longitudinal strain rate drops from its maximum initial level to reduced but still high (≈ -0.05 d⁻¹) levels in the middle of the front zone. This is punctuated by sudden (< 15 minutes) drops of strain rate to low or even extensile rates, followed by a slower (12-24 h) return to moderate levels.

Basal shear stress varies along the front zone in a way which balances the gradient of longitudinal stress indicated by strain rate: at the leading edge of the front the basal shear stress rises rapidly to a high level (≈ 1.5 bars), and drops in the middle of the front zone to very low levels (≈ 0.5 bars). In the surging zone, stress levels return to normal (higher) levels as determined by $\tau_b = \rho g h \sin \alpha$.

Shortly after entering the front, the ice column develops a foliation (S_1) oriented in vertical planes approximately transverse to the flow direction. This occurs in a region of high compressive stress (5-8 bars), but before substantial compressive strain has developed (< -0.1 , all strains given as logarithmic). Higher in the front zone, the longitudinal stress diminishes, and the transverse deviatoric stress passes through an extensile maximum. The transverse extension causes a longitudinally oriented vertical crack set (S_2) to develop. The cracks and accompanying bubble trains are not necessarily oriented perpendicular to the transverse foliation, because principle stress directions may reorient during the interval between the longitudinal and transverse stress maxima.

Finite strains during the surge accumulate in pure shear with the principle compression oriented parallel to the flow direction and the principle extension oriented vertically. The total strain is determined by the total thickness change and initial thickness. Since the total thickness change diminishes with increasing initial thickness, the total strain increases in thinner ice lying nearer to the terminus. Strain in the terminus region attains a maximum

value of -0.75 at a point ≈ 500 m behind the final position of the surge front. The strain diminishes smoothly to zero beyond this point since ice within the final position of the front zone has passed through only a fraction of the compressive regime of the front.

Crystallographic c-axis fabrics develop in the ice affected by the surge which are compatible with other fabrics seen in ice subjected to pure shear deformation. The strength of the fabric is fairly constant over the length of the terminus region, indicating that the strength of the present fabrics are not directly related to the finite strain. There may have been a closer correspondence immediately after the surge, which has been subsequently altered by annealing.

6.3 New Developments

The observations and analyses we have presented include some phenomena which have not been reported before, and some which are known but are not firmly established. Our conclusions include some new notions regarding deformation in the surge front, and some questions for which we can offer no complete answer, but which stand as challenging puzzles for future work. Here we recapitulate the most significant of the new observations and ideas.

S₀: Primary layering

Primary depositional layering (*S₀*) was observed throughout the terminus region in a state deformed by moderate, small-scale (≈ 10 cm) folding, but nonetheless distinctly recognizable. On non-surging glaciers, primary layering is ordinarily obliterated or transformed to other structures by the time it re-emerges at the terminus. Its presence here is a unique consequence of the "rafting" motion of ice during the surge phase, in which shear deformation is confined to narrow zones at the bed and margins, causing the bulk of the ice in the glacier channel to be moved downglacier with very little deformation. This unusual pattern of flow was also found in finite element calculations, which showed that the observed surface velocities during the surge were compatible with calculated internal velocities in which the horizontal component is essentially constant over the depth of the glacier. A predominant primary layering in the terminus region will be characteristic of other surging glaciers where this kind of plug flow dominates the overall pattern of deformation during a surge cycle.

S₁: Transverse foliation

The transverse foliation at the surge front was developed in a state of plane strain deformation, and is not simply the result of the passive deformation of pre-existing inhomogeneities. The foliation appears in the surge front at a point before substantial longitudinal compressive strain has developed; its appearance does coincide with the zone of highest compressive stress (3-5 bars). The strength of *S₁* upglacier from the front is essentially constant. No correspondence is seen between foliation intensity and the longitudinal variation in calculated finite strain. Evidently some mechanism of bubble transport or production within the ice has acted to create the conditions for a redistribution of bubbles within a very short time (a few days) and in the absence of compressive strains large enough to produce the observed foliation anisotropy from initially uniform clusters of bubbles. The mechanism is unknown, and its discovery will depend on a closer analysis of the nature of the bubble density change across the zone over which *S₁* appears, as well as experimental work.

S₂: Longitudinal fracture foliation

Again, a foliation is developed in a short period of time by a mechanism unrelated to finite strain. In this case the formation of the foliation was observed and is known to be the result of transverse extension. The orientation of the foliation is unusual, striking approximately parallel to the direction of principle compression. This kind of penetrative structure has not been described or recognized in ice, nor is it recognized in rocks by structural geologists, although it is somewhat akin to sheeting and jointing structures.

Crystallographic fabrics

C-axis fabrics were measured which show broad single maxima or weakly developed double maxima oriented approximately adjacent to or coaxially with the direction of principle compression. The fabric appears simultaneously with the appearance of *S₁* near the top of the final position of the surge front. This fabric is compatible with fabrics created experimentally and observed in glaciers under comparable stress conditions. An unusual aspect of the fabric is that, like *S₁*, there is no correspondence between the minor variations in fabric intensity and the calculated finite strain along the terminus profile. The fabric is essentially fully developed as soon as it appears near the upglacier limit of the surge front.

Below the final position of the surge front, fabrics with weakly defined multiple maxima are present, with the maxima centered on the poles to a subhorizontal foliation. These fabrics are not strong, but resemble classic 4-pole, or "diamond" fabrics. The unusual aspect of this fabric is that it is present in ice which has been mostly at 0°C and has undergone no substantial deformation in 22 years since 1965. Annealing to a random pattern, as observed by Rigsby (1960) to have occurred in the space of one month, has evidently not occurred here. Annealing may have been inhibited by the comparatively large grain size of the ice.

Fractures and faulting

Fractures and faults, whose role in internal deformation in glaciers is not well understood, have appeared in two roles in the propagation of the surge front. First, there is abundant evidence of small reverse fault motions along old crevasse planes during the surge, both in displacements of cross-fault markers and in strain rate signals which indicate sudden releases of stress. The faults, however, did not significantly affect the large scale pattern of deformation. The other appearance is as the fractures which formed the planes of separation along which transverse surface buckle folds formed in compression at the surge front. Finite element modelling indicates that the velocity field at the leading edge of the front may have provided a source for near-surface tensile stresses which could have formed these fractures.

Excess vertical velocity

Measured vertical velocities at the surge front were greater than those indicated by simple considerations of continuity, or by more complete finite element calculations. The excess velocity accumulated as an excess thickness of about 12% at the end of the surge. Conservation of volume is a fundamental assumption in the analysis of ice flow, and it has not been satisfied here. This may be a phenomenon restricted to glacier surges, although it may also be characteristic of other flow regimes with the same principle features - sliding, significant longitudinal stress gradients, and high water pressure - acting at lower levels. The creation of some kind of englacial void space is the most plausible source of the excess thickness, and one which is compatible with the observed settlement of the glacier surface following the surge. The creation of such a substantial quantity of void space is an important consideration in efforts to understand the englacial hydraulic system.

Distributions of basal stress and velocity

Longitudinal gradients of velocity result in gradients of stress which alter the patterns of basal shear and normal stress from distributions predicted on the basis of depth and surface slope. Anomalous high shear stresses occur at the base of the front zone, and anomalously low shear stresses appear near the top. Basal normal stresses also vary through the front, but with a much smaller magnitude of dynamically induced variation than seen in the shear stress. Calculated basal sliding velocities are high in the region of low shear stress in the front, and low in the region of high shear stress, indicating a transition from "easy" (rapid) sliding in a "lubricated" (low shear stress) region, to "hard" (slow) sliding in a region of high shear stress. The relation between sliding velocity and basal shear stress is consistent with the theory that basal water pressure controls rapid sliding. This was demonstrated clearly on the upper glacier, and is evidently the case at the surge front as well. Also of note is the fact that the basal shear stress does not vary monotonically within the front, but passes through a local minimum. Evidently, local conditions - the local geometry in particular - play an important role in determining the stress.

Hypothetical surge front

A simple continuity-based model of the surge front indicates that if boundary conditions are constant - in particular, if the ice encountered by the front is of constant thickness and if the upstream velocity is constant - then the front can propagate at a prescribed rate with its shape unchanged. This behavior is largely confirmed by events, for the changes which were observed in the shape of the actual surge front can be understood in terms of changes in initial thickness and glacier-wide changes in velocity. The implication of the model is that in the absence of external changes, the advance of rapid motion is controlled by conditions within the front zone, and that this advance can proceed in a steady, self-perpetuating way.

REFERENCES

- Allen, C.R., Kamb, W.B., Meier, M.F., Sharp, R.P., 1960. Structure of the lower Blue Glacier, Washington. *Journal of Geology*. Vol. 68, No. 6, pp. 601-625.
- Balise, M., Unpublished. The relation between surface and basal velocity variations in glaciers, with application to the mini-surges of Variegated Glacier. [Ph.D. Thesis, University of Washington, 1987.]
- Bindschadler, R.A., Harrison, W.D., Raymond, C.F., and Crosson, R., 1977. Geometry and dynamics of a surge-type glacier. *Journal of Glaciology*. Vol. 18, No. 79, pp. 181-194.
- Glen, J.W., 1955. The creep of polycrystalline ice. *Proceedings of the Royal Society of London, Ser A*. 228, pp. 519-538.
- Hambrey, M.J., Milnes, A.G., Siegenthaler, H., 1980. Dynamics and structure of Greisgletscher, Switzerland. *Journal of Glaciology*. Vol. 25, No. 92, pp. 215-228.
- Hooke, R. LeB., and Hudleston, P.J., 1978. Origin of foliation in glaciers. *Journal of Glaciology*. Vol. 20, No 88, pp. 285-299.
- Hooke, R. LeB., and Hudleston, P.J., 1980. Ice fabrics in a vertical flow plane, Barnes Ice Cap, Canada. *Journal of Glaciology*. Vol. 25, No. 92, pp. 195-214.
- Hudleston, P.J., 1977. Progressive deformation and development of fabric across zones of shear in glacier ice. (in Saxena, S., and Bhattacharji, S., ed. *Energetics of geological processes*. New York, Springer-Verlag, pp. 121-150.)
- Hudleston, P.J., and Hooke, R. LeB., 1980. Cumulative deformation in the Barnes Ice Cap and implications for the development of foliation. *Tectonophysics*. Vol 66, pp. 127-146.
- Humphrey, N.F., Unpublished. Basal hydrology of a surge-type glacier: observations and theory

relating to Variegated Glacier. [Ph.D. thesis, University of Washington, 1987.]

Kamb, W.B., Raymond, C.F., Harrison, W.D., Engelhardt, H., Echelmeyer, K.A., Humphrey, N., Brugman, M.M., and Pfeffer, T., 1985. Glacier surge mechanism: new insights from the 1982-3 surge of Variegated Glacier, Alaska. *Science*. Vol. 227, No. 4686, pp. 469-479.

Kamb, W.B., 1972. Experimental recrystallization of ice under stress. (in Heard, H.C., and others, ed. *Flow and Fracture of Rocks*, edited by H.C. Heard, I.Y. Borgh, N.L. Carter, and C.B. Raleigh. Washington. D.C., American Geophysical Union, pp.211-241. Geophysical Monograph 16.)

Kamb, W.B., 1959. Ice petrofabric observations from Blue Glacier, Washington, in relation to theory and experiment. *Journal of Geophysical Research*. Vol. 64, No. 11, pp. 1891-1909.

Langway, C.C., 1958. Ice fabrics and the universal stage. *SIPRE Technical Report*. No. 62.

Raymond, C.F., 1978. Numerical calculation of glacier flow by finite element methods. *Final Technical Report for NSF Grant No. DPP74-19075*. 213 pp.

Raymond, C.F., Johannesson, T., Pfeffer, T., and Sharp, M., 1987. Propagation of a glacier surge into stagnant ice. *Journal of Geophysical Research*, Vol. 92, No. B9, pp 9037-9049.

Raymond, C.F. and Harrison, W.D., (submitted to *Journal of Glaciology*, 1987.) Evolution of Variegated Glacier, Alaska, U.S.A., prior to its surge.

Rigsby, G.P., 1960. Crystal orientation in a glacier and in experimentally deformed ice. *Journal of Glaciology*. Vol. 3, No. 27., pp. 589-606.

Sani, R.L., Gresho, P.M., Lee, R.L., and Griffiths, D.F., 1981. The cause and cure (!) of the spurious pressures generated by certain FEM solutions of the incompressible Navier-Stokes equations: Part 1. *International Journal for Numerical Methods in Fluids*. Vol. 1, No. 1, pp. 17-43.

BIOGRAPHICAL NOTE

William Tad Pfeffer

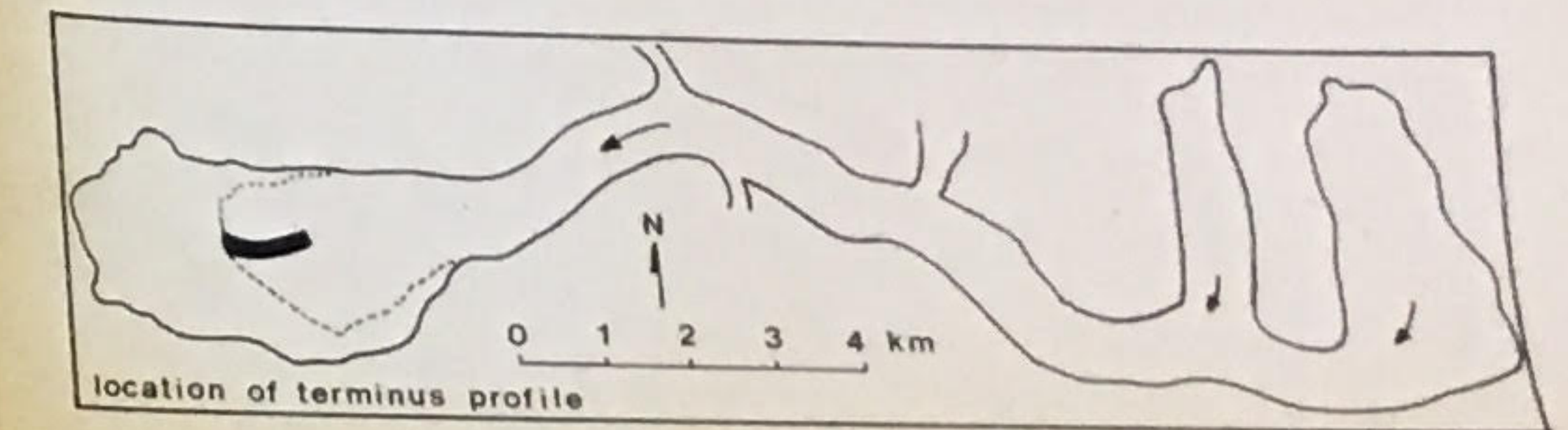
Born: 4 June, 1952, Boston Massachusetts

B.A.: University of Vermont, 1976 (Geology)

M.A.: University of Maine, 1981 (Geology)

Ph.D.: University of Washington, 1988 (Geophysics)

VARIEGATED GLACIER, ALASKA FOLIATION IN THE TERMINUS REGION FOLLOWING THE 82/83 SURGE



field measurements made 1985 & 1986

100 50 20 10 0 m

N

S₁ Foliation

S₂ Foliation

Symbols

- 80 Strike and dip of foliation
- Cracks and bubble traces
- Crevasses
- Crevasses coalesced into depressions
- Location checked for foliation; none found
- C-axis fabric site
- Strain meter site

debris cover boundary

debris cover boundary

67

72

70

59

86

72

82

83

85

79

80

76

74

71

87

73

74

81

81

85

75

73

73

75

80

85

85

85

85

85

85

85

85

85

85

85

85

85

85

85

85

85

85

85